PHYSICS AREA, THEORY AND NUMERICAL SIMULATION OF CONDENSED MATTER

Emergent phenomena in twisted Van der Waals materials

PhD Thesis

Candidate: **Mattia Angeli**
Supervisor: Michele Fabrizio

Trieste, September 2020

Publications

The present thesis is based on the following manuscripts, published or under review in international peer-reviewed journals:

— Emergent D_6 symmetry in fully relaxed magic-angle twisted bilayer graphene
M. Angeli, D. Mandelli, A. Valli, A. Amaricci, M. Capone, E. Tosatti and M. Fabrizio
Physical Review B, **98** 235237, Dec. 2018

— Valley Jahn-Teller Effect in twisted bilayer graphene
M. Angeli, E. Tosatti and M. Fabrizio
Physical Review X, **9** 041010, Oct. 2019

— Jahn–Teller coupling to moiré phonons in the continuum model formalism for small-angle twisted bilayer graphene
M. Angeli and M. Fabrizio
EPJ *Plus,* **135** 630, Jul. 2020

— Γ-valley Transition metal dichalchogenide moiré bands
M. Angeli and A.H. MacDonald
*arXiv:*2008.01735, Aug. 2020

Contents

1 Introduction

Reducing the dimensionality of a system is often associated with enhanced quantum effects, which lead to exotic electronic, optical, and magnetic properties [1]. Van der Waals layered materials are formed by stacks of atomically thin layers held together by weak van der Waals forces. Each layer has an independent chemical structure without unsatisfied valencies, which makes each individual layer stable. With isolation of a single graphite atomic sheet known as graphene, and the discovery of its intriguing physical properties, the research field of 2D materials thrived [2]. The electronic band structure of graphene can be described by introducing quasi-relativistic particles near the corners of the hexagonal Brillouin zone of the system $\mathbf{K}$ and $\mathbf{K}'$. Around these points, the valence and conduction bands meet in conical valleys where energy disperse linearly as a function of momentum. This common feature with massless Dirac fermions, leads to the emergence of various electronic properties such as the so-called Klein tunneling across a potential barrier, unconventional quantum Hall effect [3] and nontrivial Berry phase [4].

Since graphene has been stabilized, the family of 2D crystals has grown exponentially to include metals such as $NbSe_2$, semiconductors like phosphorene or most transition metal dichalchogenides (TMDs), insulators (e.g. hexagonal Boron Nitride) and magnetic materials (e.g. CrI_3). Among transition metal dichalchogenides, the most widely studied are those formed by a group-VI transition metal atom (Mo, W) sandwiched between two chalchogen layers (Se, S, Te). The monolayer bandstructure exhibit a direct band gap in the visible range located at the Brillouin zone corners. The relatively heavy metal atoms and the lack of inversion symmetry induces a strong spin orbit coupling which splits the TMDs valence bands into two spin-polarized ones in which electron spin can be controlled by circularly polarized light. Of particular interest are excitons, which, due to the lack of bulk dielectric screening, acquire large binding energies [5]. Hexagonal boron nitride is a wide-gap ($\approx$ 6 eV) insulator. Its strong, in-plane, ionic bonding of the planar hexagonal lattice structure makes it relatively inert. This and its dielectric properties make it an ideal substrate for 2D materials. In particular, encapsulating graphene in hBN protects it from the local environment and dramatically enhances electronic transport [6].

The broadening of the 2D materials family opened up the possibility to stack different 2D crystals on top of each other thus building new types of heterostructures. This allowed researchers to explore novel collective phenomena at the interfaces between different layers [7]. Recently, a new kind of heterostructure has emerged in the field. Adjusting the angle between two layers or

simply stacking layers with different lattice constants can result in structures known as *moiré superlattices*. In these systems, the local registry between the two layers periodically varies in real space with a wavelength that depends on the twist angle, and can greatly exceed the linear size of each layer's unit cell. The moiré pattern acts as a long-wavelength modulating potential, dramatically affecting electronic, optical, vibrational and structural properties. The resulting emergent states differ qualitatively from those of the underlying monolayers. The possibility to use the twist angle as a new degree of freedom opened up a new research field known as *twistronics*, which will be the main focus of this thesis.

1.1 Experimental features of magic angle twisted bilayer graphene

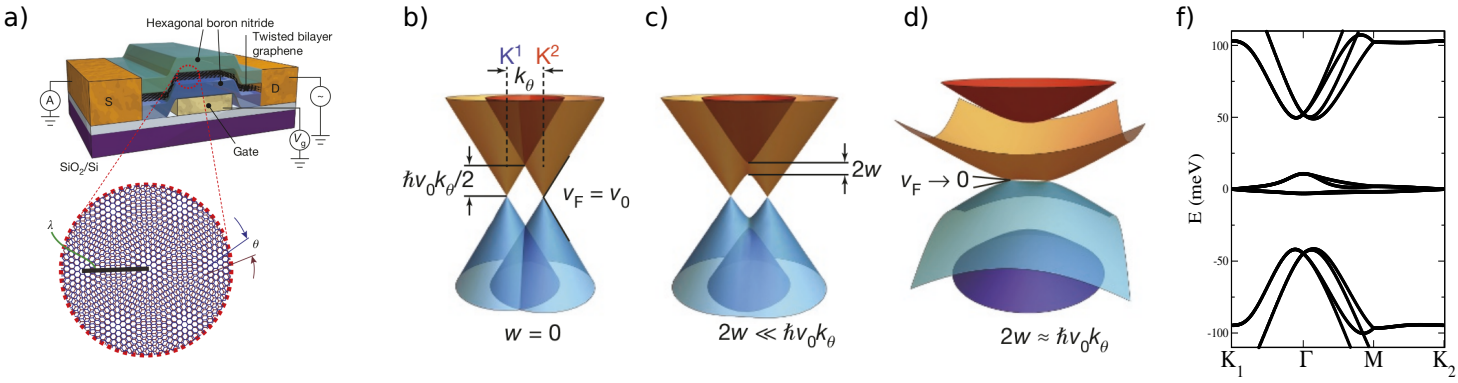

Figure 1.1: a) Schematic of the tBLG device used in Refs. [8, 9]. The twisted bilayer is encapsulated in hexagonal boron nitride flakes and fabricated on SiO_2/Si substrates. The conductance is measured while varying the local bottom gate voltage. 'S' and 'D' are the source and drain contacts, respectively. Below, a zoom within the moiré pattern with wavelength $\lambda \approx 13$ nm which form in $\theta \approx 1.1°$ tBLG. b) c) d) Effect of an increasing interlayer hybridization. When $2w$ is comparable to $\hbar v_0 k_\theta$ a set of narrow bands around neutrality form. e) $\theta = 1.08°$ tBLG bandstructure computed with tight-binding as in Ref. [10]. A set of four isolated and narrow bands form around charge neutrality set at $E = 0$. The first four panels are reproduced from Ref. [8].

Perhaps the most dramatic moiré phenomena are those observed by stacking two graphene layers slightly twisted with respect to each other (tBLG). If the two layers are decoupled, the low-energy band structure of twisted bilayer graphene can be seen as two sets of monolayer graphene Dirac cones rotated by the twist angle θ as in Fig. 1.1(b). The interlayer coupling depends on the local registry of the two layers, so that it varies smoothly along the long-wavelength moiré pattern. As a consequence, Dirac cones near either **K** or **K**' valleys mix through the interlayer hybridization. Bistritzer and MacDonald predicted in Ref. [11] that the consequences of such hybridization are the energy gaps that open near the intersection of the Dirac cones and a strong renormalization of the Fermi velocity v_F at the **K** points. In particular, at some twist angles called *magic angles*, the Fermi velocity was predicted to vanish and the resulting 'moiré ' bands confined to few tens of meV. The flattening of these bands can be understood qualitatively from the competition between the intra- and interlayer hybridization energy strengths (Fig. 1.1(b-d)). When the interlayer hybridization energy $2w$ is comparable to the energy mismatch between the Dirac cones at the intersection point, equal to $\hbar v_0 k_\theta$ where v_0 is the monolayer Fermi velocity, the layer hybridized states are pushed toward zero energy [11, 9].

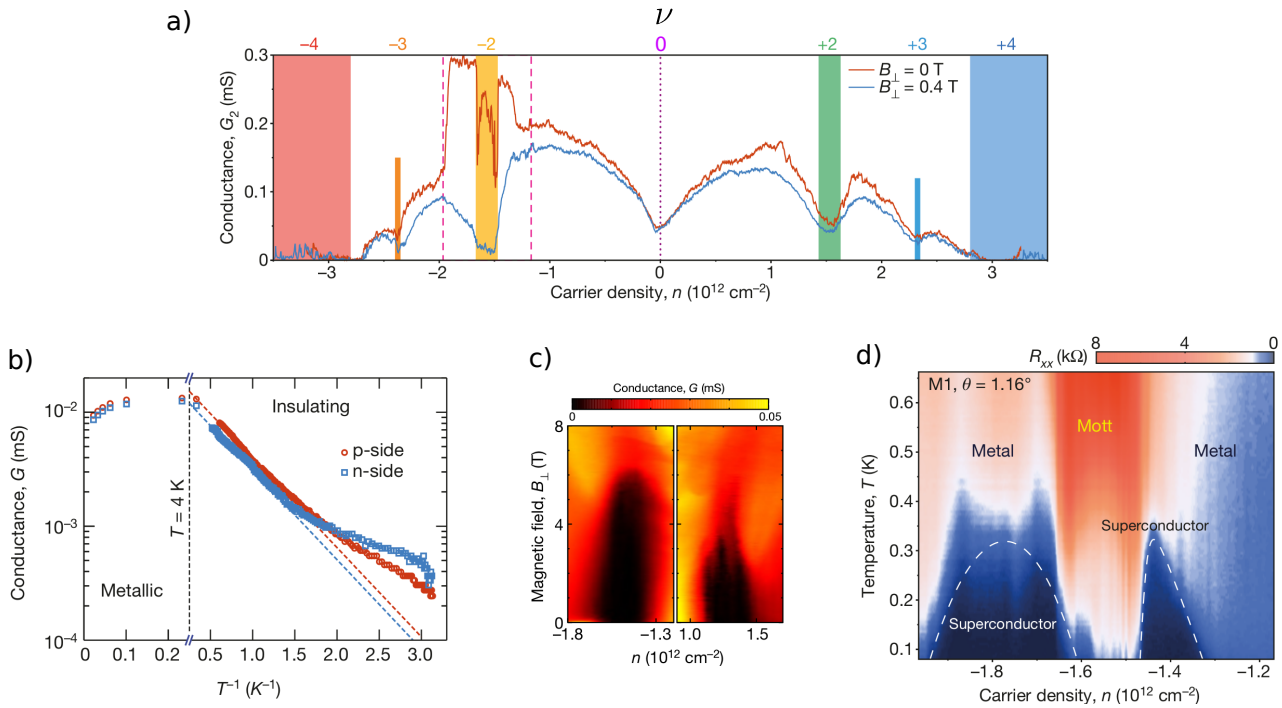

Figure 1.2: This figure is reproduced from Refs.[8, 9]. a) Two-probe conductance G of $\theta = 1.16°$ tBLG as a function of charge carrier density n measured in zero magnetic field (red) and at a perpendicular field of 0.4 Tesla (blue). On top, filling is expressed as the number of electrons ν per moiré unit cell injected into the system by gating. The curves exhibit insulating states at the superlattice band gaps, which correspond to filling of $\nu = \pm 4$ electrons in each moiré unit cell (blue and red bars). They also exhibit reduced conductance at intermediate integer fillings of $\nu = \pm 2$. Near a filling of -2 electrons per unit cell, there is considerable conductance enhancement at zero field that is suppressed in $B = 0.4$ Tesla. This enhancement signals the onset of superconductivity. b) Minimum conductance values in the quarter filling insulating states. The dashed lines are Arrhenius fits of $\exp[-\Delta/(2k_BT)]$ to the data, with $\Delta = 0.31$ meV as the thermal activation gap. c) Dependence of the conductance on the perpendicular magnetic field B of the quarter filling states at $\nu = \pm 2$. The measurement is taken at 0.3 K. d) Four-probe resistance R_{xx}, measured at densities corresponding to the region bounded by pink dashed lines in a), versus temperature. Two superconducting domes are observed next to the quarter filling insulating state, which is labeled 'Mott'. The remaining regions in the diagram are denoted as 'metal' owing to the metallic temperature dependence. The highest critical temperature observed in this device is $T_C = 0.5K$

In Fig. 1.1(f) we shown the bandstructure at the first magic angle $\theta \approx 1.1°$ along some high-symmetry lines in the Brilluoin zone of tBLG. As can be seen, a set of four extremely narrow bands lie isolated in energy around the charge neutrality point (CNP). It was by doping these bands that Cao et.al. [8, 9] opened two years ago a Pandora's box touching simultaneously 2D materials, moiré superlattices, insulating and superconducting states in narrow band materials, emergent symmetries, topological phenomena, and more.

The tBLG devices were fabricated using the 'tear and stack' technique [12], which allows controlling the twist angle with an accuracy of about $0.1° - 0.2°$ degrees. The sample was encapsulated in hexagonal boron nitride flakes with thicknesses of about $10 - 30$ nm and fabricated on SiO_2/Si substrates (see Fig. 1.1(a)). A bottom Pd/Au gate enabled the control of the charge carrier density n upon electrochemical doping.

In Fig. 1.2(a) conductance is shown as a function of charge carrier density with and without perpendicular magnetic field applied to the sample. On top, the doping density is expressed as the number of electrons ν per moiré unit cell injected into the system. As the chemical potential

is moved away from the charge neutrality point, the system is metallic until the quarter integer fillings of ±2 electrons per unit cell is reached. Here, conductance suddenly drops and the system turns into an insulator. Fig. 1.2(b) shows conductance as a function of temperature for $\nu = -2$ (p-doped) and $\nu = 2$ (n-doped) devices. Below ≈ 4 K the conductance gets exponentially suppressed. The dashed lines are Arrhenius fits of $\exp[-\Delta/(2k_BT)]$ to the data, where $\Delta \approx 0.3$ meV is the thermal activation gap. Moreover, as shown in Fig. 1.2(c), these insulators turn into metals as a perpendicular magnetic field is applied to the sample. The Zeeman energy required to suppress these quarter filling insulating states is approximately 0.5 meV, the same order of magnitude as that of the thermal excitation energy. Due to the insulating behavior being in stark contrast with the metallic one predicted by single-particle bandstructure calculations, these insulating states have been identified as correlation driven or Mott insulators. By further doping away from neutrality, the system turns into a band insulator at $\nu = \pm 4$ electrons per unit cell, which corresponds to full filling/depletion of the four flat bands (see Fig. 1.1(f)).
Perhaps, the most interesting phenomena is that observed upon slightly doping away from the insulating states at quarter filling. There, conductance abruptly rises as resistance drops to zero, which is the fingerprint of a superconducting behavior. The critical temperature is few Kelvins and 0.4 Tesla are enough to suppress this state. In Fig. 1.2(d) the phase diagram of the system around quarter filling is shown. Two superconducting domes surround the insulating state and turn into normal metal upon heating. The apparent resemblance of such a phase diagram with that of Cuprates [13] fueled an intense theoretical and experimental effort to understand the origin of these phenomena.
By improving the quality of the samples and experimental setups, the phase diagram of Refs. [8, 9] has been further enriched. First of all, insulating states have been observed at most integer fillings of the four flat bands, including at charge neutrality [14, 15, 16, 17, 18, 19, 20]. In particular, by aligining one of the two graphene layers to the hBN substrate, the insulators at $\nu = \pm 3$ filling showed an intriguing magnetic behavior [21]. The longitudinal resistance R_{xy} approaches the quantized value of $\hbar/e^2$, concomitant with a deep minimum in R_{xx} reminiscent of an integer quantum Hall state. Furthermore, the Hall resistivity is hysteretic, with a coercive field of several tens of millitesla, indicative of the Quantum anomalous Hall effect. This state requires spontaneous time reversal symmetry breaking, suggesting a non-trivial topological origin for such phenomena.
The phase diagram of magic angle tBLG has also been investigated with scanning tunneling microscopy (STM) [16, 17, 18, 20, 22]. These experiments show how the local and total density of states associated with the flat bands evolves by changing the filling. Interestingly, bandwidth and in particular the separation between the two van Hove singularities, increases when the chemical potential is within the flat bands, reaching a maximum value at the CNP. Some of these works [16, 20, 17] also report a three-fold rotational symmetry breaking when the system is doped around quarter filling.
Another interesting feature of tBLG is the large linear-in-temperature resistivity that survives over a broad range of angles and up to temperatures of several tens of Kelvin [23, 24]. A dominant role of electron-phonon scattering [23, 25] or of quantum fluctuations [24] might be behind such behavior.
Finally, superconductivity has been observed over a broader range of densities [15, 26, 14, 27], even when the insulating states were suppressed by screening of a nearby metallic layer [27] or by slightly moving the twist angle away from the magic angle condition [26]. The observation of superconductivity in the absence of correlated insulating states constitutes powerful evidence that such phenomenon arises independently, and might well be simply explained through the standard electron–phonon coupling BCS mechanism [28, 29, 30].

1.2 Moirè van der Waals materials as quantum simulation platforms

The physics of magic angle tBLG is not bound to occur only in a bilayer or in carbon allotropes, but is general to any moiré material. Twisted trilayer [31] and double bilayer [32] graphene exhibit similar insulating and superconducting behaviors. Evidences of gate tunable insulating states in ABC stacked trilayer graphene forming a moiré pattern with the underlying hBN substrate has been reported in Ref. [33].
Of particular interest are the moiré patterns formed in transition metal dichalchogenides (TMDs), which allow realizing the so-called moiré excitons [34, 35, 36, 37] that can feature topological bands supporting excitonic edge states [38]. Their bandstructure, in particular around the top of the valence band, comprises a set of extremely narrow bands. The topology of these bands depends on how the moiré heterostructure is formed. Stacking on top of each other different TMD layers (heterobilayers) lead to the formation of a moiré pattern even without a twist if the chalchogen atoms are different. In these cases, the charge density is strongly confined in a triangular superlattice. If a twist is present, it can be used to continuously tune the localization of the charge density and the lattice constant of the moiré superlattice. By quenching the kinetic energy with a twist, these bands flatten enhancing correlation effects realizing an effective Hubbard model on the triangular lattice [39].
Homobilayers can display very different physics depending on chemical composition. In WSe_2 and $MoTe_2$ the band edge of the bilayer is located around the Brilluoin zone corners. In this case, the physics is similar to that of heterobilayers. Indeed, insulating states and evidences of superconducting ones have been found upon doping the top of the valence band in twisted WSe_2, over a broad range of twist angles [40].
If the band edge is instead located around the Brilluoin zone center as in WS_2, MoS_2 and $MoSe_2$, the physics can be completely different [41, 42]. As a consequence of an emergent D_6 symmetry (see Chapter. 5) electrons are confined in an honeycomb lattice. In energetic order the first three bands realize a single-orbital (s-like) model and a two-orbital ($p_x \pm ip_y$-like) model on an honeycomb lattice [42]. The third set of bands is more intriguing, as it realizes a single-orbital model on a Kagome lattice, which is induced by an orbital hybridization that moves the charge away from the honeycomb sites. Again, since bandwidth and correlation strength can be tuned at will by changing the twist angle, these systems open the exciting possibility to study strongly correlated physics in multiorbital honeycomb and Kagome lattices.
Twisted insulators such as hBN can host triangular lattice physics similar to that of TMDs [43]. The triangular Bravais lattices emerging in the materials considered so far are due to the three fold (120°) rotational symmetry of the corresponding monolayers. This situation can be enriched by twisting 2D materials with a rectangular unit cell such as Germanium Selenide [44] or phosphorene [45]. Here,at small angles the emergent moiré lattice structure has negligible dispersion along one of the two principal axes, which forces electrons to disperse in only one direction, thus realizing an effective one dimensional model.
The systems described above are only few examples of the artificial moiré lattices which form in 2D heterostructures. The possibility to quench their kinetic energy by simply changing twist angle renders them into a versatile quantum simulation platform.

1.3 Plan of the thesis

In the first part of this Thesis we focus mostly on twisted bilayer graphene. In Chapter. 2 we review the most common theoretical tools to deal with the electronic and structural prop-

erties of twisted bilayer graphene. After describing in details the structural features of the moiré pattern formed by the relative twist between the layers, we introduce lattice relaxation (Section. 2.2).Then, the bandstructure of the system is computed by means of tight-binding (Section. 2.3.1) and Continuum model Hamiltonians (Section. 2.3.2).
In Chapter. 3 we deal with the difficult but important task to reduce the complexity of the problem by deriving a minimal (number of orbitals) model that faithfully describes the flat bands physics. We start by showing the set of emergent symmetries developed by the system in Section. 3.1. As a consequence of these symmetries we prove that a description of the flat bands in terms of only four Wannier orbitals is not possible (Section. 3.2). In the last part of this Chapter (Section. 3.3) we propose a 16 Wannier orbitals model which is able to reproduce the flat bands complexity.
In Chapter. 4 we describe a lattice driven mechanism which might be responsible of the experimental features observed in Refs. [8, 9]. In Section. 4.1 we compute the phonon spectrum of the twisted bilayers, showing that the system develops a set of almost dispersionless modes that resemble global vibrations of the moiré supercell dubbed as *moiré phonons*. Such phonons are strongly coupled to the emergent electronic degrees of freedom, and are able to open gaps at most integer filling of the four flat bands (Section. ‘4.1.3 and Section. 4.1.5). Such mechanism is extremely efficient, as a lattice deformation of less than few mÅ can open gaps of tens of meV. As explained in Section. 4.1.4, this electron-phonon coupling mechanism and its efficiency realizes by an $E \otimes e$ Jahn-Teller Hamiltonian. In Section. 4.2 we describe the superconducting state that might be mediated by the Jahn-Teller phonons. Finally, in Section. 4.3 we work out how the Jahn-Teller mechanism can be included within the continuum model formalism.
In Chapter. 5 we focus on twisted transition metal dichalchogenides. We derive a continuum model Hamiltonian for those homobilayers (identified in Section. 5.1) in which the valence band edge is around the Brilluoin zone center Γ. As a consequence of the emergent symmetries described in Section. 5.2.1 the system simulates honeycomb lattice physics. In Section. 5.2.2 the continuum model for twisted WS_2, MoS_2 and $MoSe_2$ is derived by fitting DFT calculations that include lattice relaxation. In Section. 5.2.3 we demonstrate the efficacy of the continuum model to predict the bandstructure of twisted TMDs at small angles, where fully microscopic calculations are prohibitive. A symmetry analysis of the Bloch states with the three set of bands higher in energy reveal their origin, which can be described in terms of a simple harmonic oscillator picture (Section. 5.2.4).
The last Chaper. 6 is devoted to concluding remarks.

2

Lattice and electronic structure of twisted bilayer graphene

In this chapter we introduce the most common theoretical tools used to obtain the structural and electronic properties of twisted bilayer graphene (tBLG). After defining those angles at which the lattice is periodic in Section. 2.1, we employ molecular dynamics techniques to determine the relaxed structures (Section. 2.2). In the second part of this chapter, we focus on their bandstructure, which is computed by means of tight-binding in Section. 2.3.1 and continuum model calculations in Section. 2.3.2.

2.1 Commensurate angles

When two layers are slightly misaligned with respect to each other a moiré pattern form. The resulting lattice is in general not periodic, except at a specific set of discrete angles known as 'commensurate angles' [46]. In order to determine this set of angles, we consider two identical and aligned honeycomb lattices with lattice constant a and lattice vectors:

$$\begin{aligned} \mathbf{a}_0 &= (1/2, -\sqrt{3}/2)\, a, \\ \mathbf{b}_0 &= (1/2,\ \sqrt{3}/2)\, a \end{aligned} \tag{2.1}$$

the two sites in the unit cell are assumed to be located at

$$\begin{aligned} \mathbf{r}_A &= \frac{2}{3}\,\mathbf{a}_0 + \frac{1}{3}\,\mathbf{b}_0\,, \\ \mathbf{r}_B &= \frac{1}{3}\,\mathbf{a}_0 + \frac{2}{3}\,\mathbf{b}_0 \end{aligned} \tag{2.2}$$

where the origin is the center of the hexagon.
The reciprocal lattice vectors are defined as

$$\begin{aligned} \mathbf{G}_a &= \frac{4\pi}{\sqrt{3}a}\,(\sqrt{3}/2, -1/2)\,, \\ \mathbf{G}_b &= \frac{4\pi}{\sqrt{3}a}\,(\sqrt{3}/2, 1/2) \end{aligned} \tag{2.3}$$

We consider a generic lattice vector

$$\mathbf{R}_{-n,m} = -n\,\mathbf{a}_0 + m\,\mathbf{b}_0 = \Big((m-n)/2\,,\ \sqrt{3}(m+n)/2\Big) \equiv R_{nm}\Big(\sin\phi_{nm}\,,\ \cos\phi_{nm}\Big)\,, \tag{2.4}$$

where

$$R_{nm} = a\,\sqrt{n^2+m^2+n\,m}\ ,\ \tan\phi_{nm} = \frac{1}{\sqrt{3}}\,\frac{m-n}{m+m}\ . \tag{2.5}$$

Since the honeycomb lattice is symmetric under reflection with respect to the y-axis [30], for a given $\mathbf{R}_{nm} = (R_x, R_y)$ there always exists a $\mathbf{R}_{mn} = (-R_x, R_y)$. Therefore, if we rotate one layer by ϕ_{nm} and the other by $-\phi_{nm}$, we have that they have in common the superlattice vector $\mathbf{R}_{m,n} \to R_{nm}\,(0,1)$. The full spectrum of commensurate angles can be obtained through Eq. (2.5) for several choices of n and m. Noting that $m-n$ and $m+n$ have the same parity, the equivalence class (p,q) of rational numbers $p/q = (m-n)/(n+m)$, with $p-q$ even, defines the same

$$\tan\phi = \frac{1}{\sqrt{3}}\,\frac{p}{q}\ , \tag{2.6}$$

but generally different

$$R_{nm} = a\,\sqrt{n^2+m^2+n\,m}\ \to R(p,q) = a\,\sqrt{\frac{3}{4}\,q^2 + \frac{1}{4}\,p^2}\ = \frac{p}{2\sin\phi}\ , \tag{2.7}$$

which are multiple of each other. Therefore, the fundamental R within each equivalence class is defined by the minimum p, and identifies the lattice vector of the moiré superlattice $\mathbf{R} = R\,(0,1)$. By fixing $p=1$ and q as an odd integer equal to $q = 2k+1$, we have that

$$R = \frac{a}{2\sin\phi} \qquad \tan\phi_k = \frac{1}{\sqrt{3}}\,\frac{1}{2k+1} \tag{2.8}$$

where $k \in \mathbb{Z}^{\geq}$. For instance, if $k = 30$ we have that the twisting angle is $\theta = 2\phi \simeq 1.08°$, the number of atoms in the unit cell is $N = 4R^2 = 11164$ and the moiré lattice constant is several thousand times larger than that of the layers forming it.
Given Eq. 2.8, the moiré lattice vectors can be chosen as

$$\mathbf{R}_1 = R\,(\,\sqrt{3}/2\,,\,-1/2) \qquad ,\mathbf{R}_2 = R\,(\,\sqrt{3}/2\,,\,1/2)\,, \tag{2.9}$$

The moiré reciprocal lattice vectors are consequently

$$\begin{aligned}\mathbf{G_1} &= \frac{4\pi}{\sqrt{3}R}\,(1/2\,,\,-\sqrt{3}/2) = \frac{4\pi\sin\phi}{\sqrt{3}}\,(1\,,\,-\sqrt{3})\,,\\ \mathbf{G_2} &= \frac{4\pi}{\sqrt{3}R}\,(1/2\,,\,\sqrt{3}/2) = \frac{4\pi\sin\phi}{\sqrt{3}}\,(1\,,\,\sqrt{3})\,,\end{aligned} \tag{2.10}$$

so that the two monolayer Brillouin zones are folded several times in the mini-Brillouin zone (MBZ) of the system, which is still hexagonal (see 2.1). In the untwisted bilayer the Dirac points are

$$\begin{aligned}\mathbf{K}' &= -\frac{1}{3}\,\mathbf{G}_a + \frac{2}{3}\,\mathbf{G}_b = \frac{4\pi}{3}\,(1/2\,,\,\sqrt{3}/2)\,,\\ \mathbf{K} &= -\frac{2}{3}\,\mathbf{G}_a + \frac{1}{3}\,\mathbf{G}_b = \frac{4\pi}{3}\,(-1/2\,,\,\sqrt{3}/2)\,,\end{aligned} \tag{2.11}$$

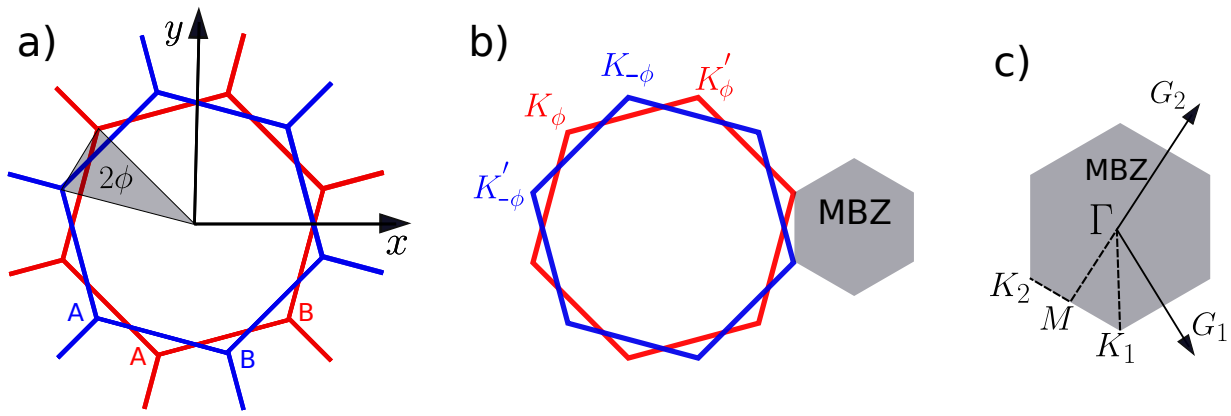

Figure 2.1: a) Two overimposed honeycomb lattices twisted by an angle $\theta = 2\phi$. b)The two monolayer Brillouin zones (in red and blue) are folded several times in the mini-Brillouin zone (MBZ) of the twisted lattice. Inequivalent $\mathbf{K}/\mathbf{K}'$ points in different layers are folded into the same $\mathbf{K_1}/\mathbf{K_2}$ points in the MBZ. c) The MBZ formed by the reciprocal lattice vectors G_1 and G_2. One of the high-symmetry paths often used in this thesis is also denoted by a black dashed line.

and the three equivalent points obtained by a 120° rotation. We consider two of these points, specifically

$$\begin{aligned}\mathbf{K}'_k &= k\,(\mathbf{G}_2 - \mathbf{G}_1) + \mathbf{K}' = \frac{2\pi}{\sqrt{3}/2}\left(\frac{1}{2\sqrt{3}}\,,\, k + \frac{1}{2}\right) = \left|\mathbf{K}_k\right|(\sin\phi_k\,,\,\cos\phi_k)\,,\\ \mathbf{K}_k &= k\,(\mathbf{G}_2 - \mathbf{G}_1) + \mathbf{K} = \frac{2\pi}{\sqrt{3}/2}\left(-\frac{1}{2\sqrt{3}}\,,\, k + \frac{1}{2}\right) = \left|\mathbf{K}_k\right|(-\sin\phi_k\,,\,\cos\phi_k)\,.\end{aligned} \tag{2.12}$$

If we assume that $\mathbf{K}'_k$ belongs to the top layer while $\mathbf{K}_k$ to the bottom one , it follows that after the twist the two fall to the same point along the y-axis if

$$\tan\phi_k = \frac{1}{\sqrt{3}}\,\frac{1}{2k+1}\,, \tag{2.13}$$

which is exactly the condition (2.8). The above result thus implies that $\mathbf{K}(\mathbf{K}')$ of one layer and $\mathbf{K}'(\mathbf{K})$ of the other layer fold on the same point in the MBZ.

2.2 Moirè pattern and lattice relaxation in twisted bilayer graphene

In Fig. 2.2 we show two graphene layers rotated with respect to each other by a small angle. Due to the small misalignment between the graphene layers, a moiré pattern forms where regions characterized by local realizations of different stacking modes appear periodically within the bilayer. Bernal-stacked regions (AB or BA) form an honeycomb lattice (green and orange triangles in Fig. 2.2), while AA-stacked regions in the hexagon centers form a triangular lattice. This picture is however not realistic, as it turns out that there is a substantial lattice energy mismatch between zones differently stacked within the moiré pattern. This can be seen in Table 2.1, where the total energy of aligned graphene bilayers is shown for different stackings. This energy difference which varies smoothly along the moiré, generating a non-uniform force field which tends to dramatically alter the lattice [47, 48, 49, 50, 51, 52, 10, 30, 53, 54]. Indeed,

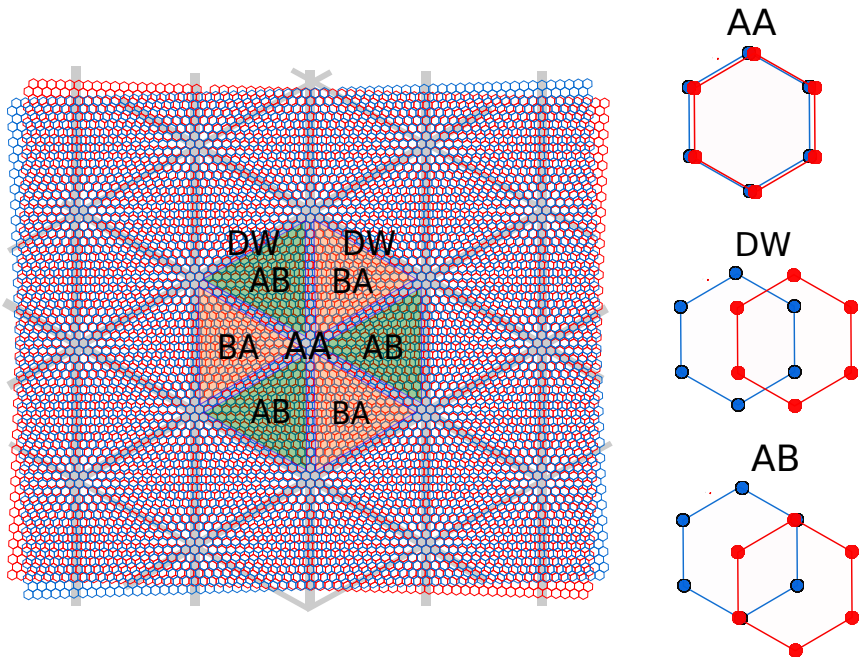

Figure 2.2: Moiré superlattice formed by two unrelaxed graphene layers (in blue and red) twisted by a small angle θ. We indicate the different stacking regions: AA and the two different Bernal regions AB and BA. The domain walls (DWs) separate AB from BA regions,connect different AA regions and are denoted by grey lines. On the right, a zoom within the high-symmetry stacking regions is shown.

there is strong experimental evidence of a substantial lattice relaxation, especially at small twist angles [55, 48], which needs to be accounted for to get physically reliable results.
We thus performed lattice relaxations via classical molecular dynamics simulations using state-of-the-art force-fields. The carbon-carbon intralayer interactions are modeled via the second generation REBO potential [56]. The interlayer interactions are instead modeled via the Kolmogorov-Crespi (KC) potential,[57] using the parametrization of Ref. [58]. The starting intralayer carbon-carbon distance is set equal to $a_0 = 1.3978$ Å, corresponding to the equilibrium bond length of the adopted REBO potential, giving a lattice parameter of $a \approx 2.42$ Å. Geometric optimizations are performed using the FIRE algorithm.[59] The atomic positions are relaxed toward equilibrium until total force acting on each atom, $F_i = |-\nabla_{\mathbf{r}_i}(V^{\mathrm{KC}}_{\mathrm{inter}} + V^{\mathrm{REBO}}_{\mathrm{intra}})|$, become less than 10^{-6} eV/atom. It is important to stress that during the relaxation the system is not constrained to preserve any particular symmetry. Fig. 2.3(a) shows the supercell of tBLG at $\theta \approx 1.08°$, before relaxation, corresponding to a triangular superlattice of period ≈ 13 nm. Examining different directions, areas of energetically least favorable AA stacking, see Table 2.1, gradually turn into energetically more favorable saddle point (SP) regions or most favorable AB and BA stacking regions. This is achieved via small in-plane deformations characterized by a displacement field that rotates around the center of the AA domains (see Fig. 2.3(c)), respectively counterclockwise and clockwise in the upper and lower layer. As a consequence of this the AA regions shrink while the area of the Bernal-stacked regions expand (see Fig. 2.3(b)). The interface regions between AB and BA sharpen, forming the so called domain walls (DWs). We note that such distortions lead to negligible local lattice compressions/expansions, corresponding to variations $< 0.03\%$ of the stiff carbon-carbon bond length relative to the equilibrium value. On the other hand, the large difference between the equilibrium interlayer distances of the AA and AB stacking (see Table 2.1) leads to significant out-of-plane buckling deformations, genuine "corrugations" of the graphene layers, that form protruding bubbles in correspondence of the AA regions. This is clearly shown in Fig. 2.3(d), where the color map of the local interlayer

	interlayer dist. (Å)	$\Delta\varepsilon$ (meV/atom)
AB	3.39	0
SP	3.42	0.74
AA	3.61	4.70

Table 2.1: The equilibrium interlayer distance and the corresponding total energy of aligned ($\theta = 0°$) graphene bilayers at various stacking modes, specified in the first column. Energies are measured relative to that of the optimal AB stacking. Results obtained by initially shifting the relative (x,y) centers-of mass of the two layers, and then relaxing. For the case of AB stacking, a full relaxation of the bilayer was performed. For the case of AA or SP stacking, only the z coordinate of all atoms was relaxed, while the in plane (x,y) coordinates were held fixed. This prevented the bilayer from falling into the AB global minimum, thus preserving the initial stacking.

distance, shows an overall increase of ~ 0.2 Å from Bernal AB (blue circle) to the AA region (green circle). We end by pointing out that the stacking-dependence of the force fields acting on each atom, which varies smoothly along the moiré, will also affect phonons. As shown in the next chapter 4.1.2, the normal modes of the system are modulated and strongly affected by the moiré pattern.

2.3 Bandstructure of twisted bilayer graphene

2.3.1 Tight-binding

The tight-binding method is an useful tool to compute the electronic properties of a system. In particular, the fact that the Hamiltonian depends directly on the atomic positions, makes this method suitable to treat systems with a deformed or relaxed lattice. Denoting the position within the unit cell of atom i as $\mathbf{r}_i$ we can write the tight-binding Hamiltonian as:

$$\hat{\mathscr{H}} = \sum_{i,j} \Big(t(\mathbf{r}_i - \mathbf{r}_j) \, |i\rangle \langle j| + \text{ H.c.} \Big), \tag{2.14}$$

where $t(\mathbf{r}_i - \mathbf{r}_j)$ is the hopping amplitude which is computed using the Slater-Koster formalism: [60]

$$t(\mathbf{d}) = V_{pp\sigma}(d) \Big[\frac{\mathbf{d} \cdot \mathbf{e}_z}{d} \Big]^2 + V_{pp\pi}(d) \Big[1 - \Big(\frac{\mathbf{d} \cdot \mathbf{e}_z}{d} \Big)^2 \Big], \tag{2.15}$$

where $\mathbf{d} = \mathbf{r}_i - \mathbf{r}_j$, $d = |\mathbf{d}|$, and $\mathbf{e}_z$ is the unit vector in the direction perpendicular to the graphene planes. The out-of-plane (σ) and in-plane (π) transfer integrals are:

$$V_{pp\sigma}(x) = V^0_{pp\sigma} \mathrm{e}^{-\frac{x-d_0}{r_0}} \qquad V_{pp\pi}(x) = V^0_{pp\pi} \mathrm{e}^{-\frac{x-a_0}{r_0}} \tag{2.16}$$

where $V^0_{pp\sigma} = 0.48\ eV$ and $V^0_{pp\pi} = -2.7\ eV$ are values chosen to reproduce ab-initio dispersion curves in AA and AB stacked bilayer graphene, $d_0 = 3.344$Å is the starting inter-layer distance, $a = 1.3978$Å is the intralayer carbon-carbon distance, and $r_0 = 0.184\ a$ is the decay length, in units of the lattice parameter.[61, 50] Although the hopping amplitude decreases exponentially with distance, we found that upon setting even a fairly large cutoff r_c, important features of

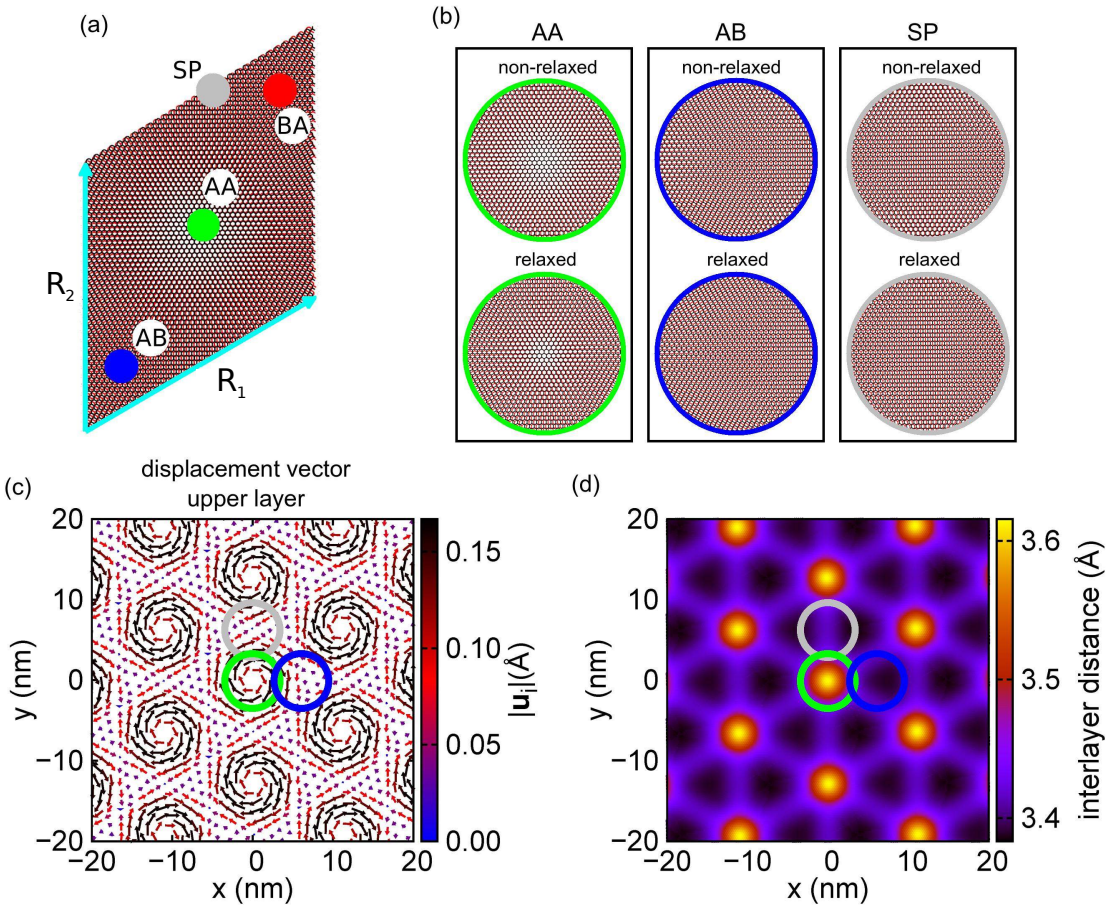

Figure 2.3: (a) The supercell of a tBLG at $\theta \approx 1.08°$ used in simulations. Arrows show the primitive lattice vectors, of length R, of the triangular moiré superstructure. Green, grey, red and blue circles mark the regions of AA, SP, AB and BA stacking, respectively. (b) Local structure before and after relaxation around the center of the AA, SP and AB regions. (c) Displacement field showing the in-plane deformations of the upper layer. The displacement vectors $\{\mathbf{u}_i\}$ go from the equilibrium position of the carbon atoms in the non-relaxed configuration to the corresponding position in the fully relaxed structure. Only few vectors are shown for clarity, magnified by a factor of ten. (d) Colored map showing the local interlayer distance. The colored circles reported in panels (c) and (d) correspond to the samples of panel (b).

the band structure are spoiled. An example is the degeneracy at the $K_{1(2)}$ points, which we find to be fourfold, up to our numerical accuracy, keeping all hopping amplitudes that are nonzero within machine precision, while it is fully lifted using a cutoff as large as $r_c \approx 4a_0$. In Fig. 2.4 we show the bandstructure of twisted bilayer graphene before relaxation. The bandwidth of the four bands close to neutrality, which are highlited in yellow, decreases with twist angle while being compressed around neutrality. Then, at an angle $\theta_c \approx 1.3°$,the bandwidth reaches a minimum and by further decreasing the angle the bandwidth increases again. They become extremely flat again at $\theta_c = 0.5°$ and at a series of other magic angles. However, although a set of extremely flat bands is predicted, the bandstructure of the unrelaxed structure differ quantitatively from the experimental data. There, the angle in which superconductivity is observed is smaller, around $1.05° \sim 1.1°$ [9, 15]. More importantly, the flat bands are reproducibly found in experiments [14, 8, 9, 15, 16, 17, 23, 62, 63] to be separated from the other bands by a sizeable gap of around $\sim 30 - 50$ meV, a feature not observed in the bands in Fig. 2.4. A better agreement with experiments is obtained if lattice relaxation is taken into account. We therefore computed the bandstructure of the system updating the atomic positions in the unit cell with

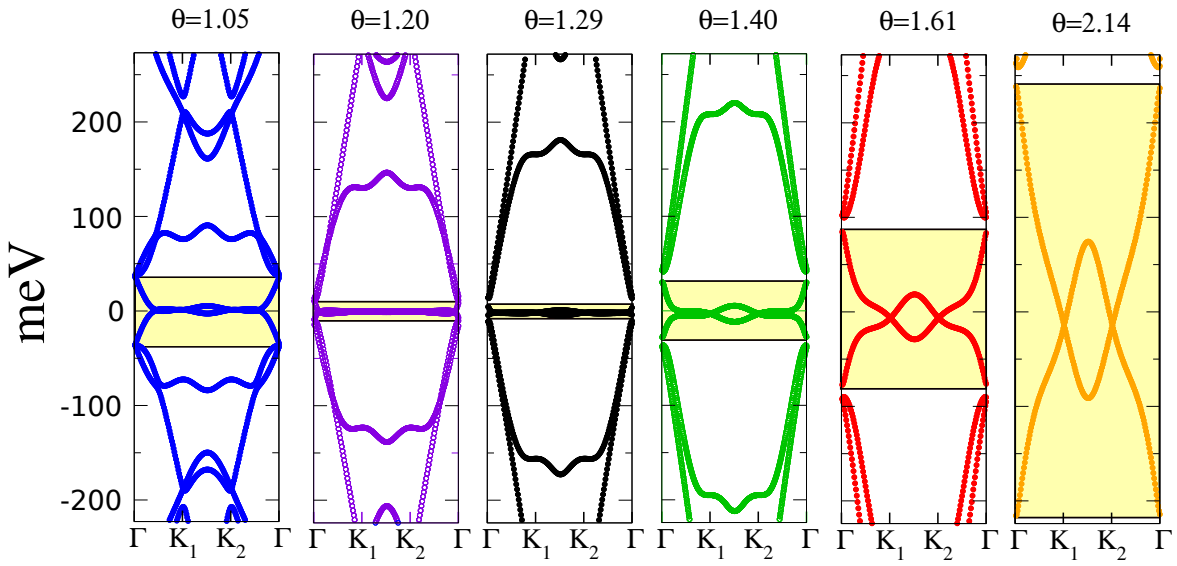

Figure 2.4: Bandstructure of *unrelaxed* twisted bilayer graphene at different angles. The background of the set of four bands around charge neutrality is colored in yellow. Their bandwidth monotonously decreases until $\theta \approx 1.3°$, then it increases again.

those of the relaxed structure. We assumed the carbon π-orbitals to be oriented along $\mathbf{e}_z$, while in reality they are oriented along the direction locally perpendicular to the relaxed graphene sheet, no longer flat. However, since the out of plane distortions varies smoothly along the moiré pattern, we checked that the misorientation of the orbitals with respect to the z axis are lower than $\sim 0.1 - 0.01°$, and have no noticeable effect on the band structure. While the above discussion focused on a specific supercell at $\theta \approx 1.08°$, qualitatively similar results were obtained for other angles, too. We emphasize that out-of-plane deformations, significant at small magic angles, have important effects on the electronic structure of the system. Indeed, as can be seen from Fig. 2.5(a), where the tight-binding band structure is calculated for the fully relaxed structure, the flat bands are now well separated from the rest by an $\approx 35 - 40$ meV gap, consistent with experiments [8, 15, 9] and DFT calculations [53, 54], and larger than the gap obtained allowing only in-plane displacements.[50] Furthermore, the flat bands Fig. 2.5(b) are considerably flatter than in the unrelaxed structure at a similar angle, so that lattice relaxation lowers the magic angle to a value consistent with experiments [64]. Finally, the particle-hole asymmetry is also a feature present only if lattice relaxation is included in the calculation and routinely observed in experiments [18, 16].

2.3.2 Continuum Model Hamiltonian

The large number of atoms contained in the $\theta \approx 1.08°$ unit cell of twisted bilayer graphene (more than 11000), make any calculation, more involved than a simple thigh-binding one, rather tough, if not computationally impossible. Such a problem can be solved introducing the less computationally demanding continuum model of Ref. [11]. This approach avoids the real space complexity of the problem by solving it in reciprocal space. This method can serve as a suitable starting point for BCS [28, 29], Hartree-Fock [65, 66, 67, 68] and many other calculations, which may involve both phonons and correlations. In order to derive the Bistritzer-MacDonald continuum model for twisted bilayer graphene [11], we recall that the single layer

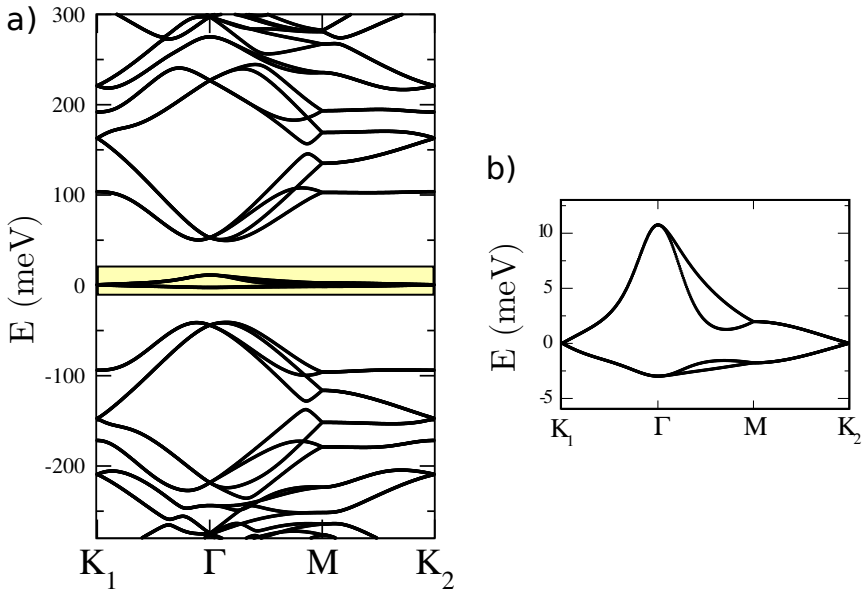

Figure 2.5: a) Bandstructure of *relaxed* twisted bilayer graphene at the magic angle $\theta \approx 1.08°$ obtained with tight-binding. b) zoom within the flat bands region. These bands are isolated in energy due to the lattice relaxation.

Dirac Hamiltonian is, around the $\mathbf{K}$ and $\mathbf{K}' = -\mathbf{K}$ valleys, respectively,

$$\begin{aligned} \hat{H}_{\mathbf{k}\sim\mathbf{K}} \equiv \hat{H}^{+1}_{\mathbf{k}} &= -v\left(\mathbf{k}-\mathbf{K}\right)\cdot\left(\sigma_x,\sigma_y\right), \\ \hat{H}_{\mathbf{k}\sim-\mathbf{K}} \equiv \hat{H}^{-1}_{\mathbf{k}} &= -v\left(\mathbf{k}+\mathbf{K}\right)\cdot\left(-\sigma_x,\sigma_y\right), \end{aligned} \tag{2.17}$$

namely

$$\hat{H}^{\zeta}_{\mathbf{k}} = -v\left(\mathbf{k}-\zeta\mathbf{K}\right)\cdot\left(\zeta\,\sigma_x,\sigma_y\right), \tag{2.18}$$

with $\zeta = \pm 1$ the valley index, and where the Pauli matrices σ_a act on the two component wavefunctions, each component referring to one of the two sites per unit cell that form the honeycomb lattice.
We recall that the reciprocal lattice vectors in the MBZ are:

$$\begin{aligned} \mathbf{G}_1 &= \mathbf{G}^{(2)}_b - \mathbf{G}^{(1)}_b, \\ \mathbf{G}_2 &= \mathbf{G}^{(1)}_a - \mathbf{G}^{(2)}_a. \end{aligned} \tag{2.19}$$

where $\boldsymbol{G}^{(1)}_{a/b} = \mathscr{R}_{+\phi}(\boldsymbol{G}_{a/b})$ and $\boldsymbol{G}^{(2)}_{a/b} = \mathscr{R}_{-\phi}(\boldsymbol{G}_{a/b})$ are the reciprocal lattice vectors of each layer after the twist (the layer index is denoted by the apex $(1/2)$), with $\mathscr{R}_\phi$ the rotation operator by an angle ϕ.
The Dirac nodes of each monolayer are, correspondingly, $\mathscr{R}_{\pm\phi}(\mathbf{K}) \equiv \mathbf{K}_{\pm\phi}$ for the valley we shall denote as $\zeta = +1$, and $\mathscr{R}_{\pm\phi}(\mathbf{K}') \equiv \mathbf{K}'_{\pm\phi}$ for the other valley, $\zeta = -1$. With our choices, $\mathbf{K}_{+\phi}$ and $\mathbf{K}'_{-\phi}$ fold into the same point $\mathbf{K}_1$ of the MBZ, as well as $\mathbf{K}_{-\phi}$ and $\mathbf{K}'_{+\phi}$ into the point $\mathbf{K}_2$, see Fig. 2.1b).
We introduce the (real) Wannier functions derived by the p_z orbital of each carbon atom:

$$\begin{aligned} \phi_{1\,\alpha\mathbf{R}^{(1)}}(\mathbf{r}) &\equiv \phi\Big(\mathbf{r}-\mathbf{R}^{(1)}-\mathbf{r}^{(1)}_\alpha-\frac{\boldsymbol{d}_\perp}{2}\Big), \\ \phi_{2\,\alpha\mathbf{R}^{(2)}}(\mathbf{r}) &\equiv \phi\Big(\mathbf{r}-\mathbf{R}^{(2)}-\mathbf{r}^{(2)}_\alpha+\frac{\boldsymbol{d}_\perp}{2}\Big), \end{aligned} \tag{2.20}$$

where $\boldsymbol{d}_\perp = (0,0,d)$, with d the interlayer distance, $\mathbf{R}^{(i)}$ label the positions of the unit cells in layer $i = 1,2$, while $\mathbf{r}_\alpha^{(i)}$ the coordinates with respect to $\mathbf{R}^{(i)}$ of the two sites within each unit cell, $\alpha = A, B$ denoting the two sublattices. From the Wannier functions we build the Bloch functions

$$\begin{aligned}\psi_{1\,\alpha\mathbf{k}}(\mathbf{r}) &= \frac{1}{\sqrt{N}} \sum_{\mathbf{R}^{(1)}} \mathrm{e}^{-i\mathbf{k}\cdot\left(\mathbf{R}^{(1)}+\mathbf{r}_\alpha^{(1)}\right)}\, \phi_{1\,\alpha\mathbf{R}^{(1)}}(\mathbf{r})\,,\\ \psi_{2\,\alpha\mathbf{k}}(\mathbf{r}) &= \frac{1}{\sqrt{N}} \sum_{\mathbf{R}^{(2)}} \mathrm{e}^{-i\mathbf{k}\cdot\left(\mathbf{R}^{(2)}+\mathbf{r}_\alpha^{(2)}\right)}\, \phi_{2\,\alpha\mathbf{R}^{(2)}}(\mathbf{r})\,.\end{aligned} \tag{2.21}$$

Conventionally, one assumes the two-center approximation [11], so that, if $V_\perp(\mathbf{r})$ is the interlayer potential, then the interlayer hopping

$$\iint d\mathbf{r}\, \phi_{1\,\alpha\mathbf{R}^{(2)}}(\mathbf{r})\; V_\perp(\mathbf{r})\; \phi_{2\beta\mathbf{R}^{(1)}}(\mathbf{r}) \simeq T_\perp\!\left(\mathbf{R}^{(2)} + \mathbf{r}_\alpha^{(2)} - \mathbf{R}^{(1)} - \mathbf{r}_\beta^{(1)}\right), \tag{2.22}$$

depends only on the distance between the centers of the two Wannier orbitals. We define $T_\perp(\mathbf{q})$, the Fourier transform of $T_\perp(\mathbf{r})$:

$$T_\perp(\mathbf{r}) = \frac{1}{N} \sum_{\mathbf{q}} \mathrm{e}^{i\mathbf{q}\cdot\mathbf{r}}\; T_\perp(\mathbf{q})\,, \tag{2.23}$$

where $\mathbf{r}$ and $\mathbf{q}$ are vectors in the x-y plane. Hereafter, all momenta are assumed also to lie in the x-y plane.
The interlayer hopping between an electron in layer 1 with momentum $\mathbf{p}$ and one in layer 2 with momentum $\mathbf{k}$ is in general a matrix $\hat{T}_{\mathbf{kp}}$, with elements $T_{\mathbf{kp}}^{\alpha\beta}$, $\alpha,\beta = A, B$, which, through equations (2.21), (2.22) and (2.23), reads explicitly

$$\begin{aligned} T_{\mathbf{kp}}^{\alpha\beta} &= \frac{1}{N} \sum_{\mathbf{R}^{(2)}\mathbf{R}^{(1)}} \mathrm{e}^{-i\mathbf{k}\cdot\left(\mathbf{R}^{(2)}+\mathbf{r}_\alpha^{(2)}\right)}\, \mathrm{e}^{i\mathbf{p}\cdot\left(\mathbf{R}^{(1)}+\mathbf{r}_\beta^{(1)}\right)}\; T_\perp\!\left(\mathbf{R}^{(2)} + \mathbf{r}_\alpha^{(2)} - \mathbf{R}^{(1)} - \mathbf{r}_\beta^{(1)}\right)\\ &= \sum_{\mathbf{q}} T_\perp(-\mathbf{q})\; \frac{1}{N^2} \sum_{\mathbf{R}^{(2)}\mathbf{R}^{(1)}} \mathrm{e}^{-i\left(\mathbf{k}+\mathbf{q}\right)\cdot\left(\mathbf{R}^{(2)}+\mathbf{r}_\alpha^{(2)}\right)}\, \mathrm{e}^{i\left(\mathbf{p}+\mathbf{q}\right)\cdot\left(\mathbf{R}^{(1)}+\mathbf{r}_\beta^{(1)}\right)}\\ &= \sum_{\mathbf{q}} T_\perp(-\mathbf{q}) \sum_{\mathbf{G}^{(2)}\mathbf{G}^{(1)}} \delta_{\mathbf{k}+\mathbf{q},\,-\mathbf{G}^{(2)}}\, \delta_{\mathbf{p}+\mathbf{q},\,-\mathbf{G}^{(1)}}\, \mathrm{e}^{i\mathbf{G}^{(2)}\cdot\mathbf{r}_\alpha^{(2)}}\, \mathrm{e}^{-i\mathbf{G}^{(1)}\cdot\mathbf{r}_\beta^{(1)}}\\ &= \sum_{\mathbf{G}^{(2)}\mathbf{G}^{(1)}} T_\perp\!\left(\mathbf{k}+\mathbf{G}^{(2)}\right) \delta_{\mathbf{k}+\mathbf{G}^{(2)},\,\mathbf{p}+\mathbf{G}^{(1)}}\, \mathrm{e}^{i\mathbf{G}^{(2)}\cdot\mathbf{r}_\alpha^{(2)}}\, \mathrm{e}^{-i\mathbf{G}^{(1)}\cdot\mathbf{r}_\beta^{(1)}}\,. \end{aligned} \tag{2.24}$$

Since we are interested in the low energy physics, $\mathbf{k}$ and $\mathbf{p}$ must be close to the corresponding Dirac points, namely $\mathbf{K}_\phi$ and $\mathbf{K}'_\phi$ for $\mathbf{p}$ in layer 1, while $\mathbf{K}_{-\phi}$ and $\mathbf{K}'_{-\phi}$ for $\mathbf{k}$ in layer 2. Therefore, $\hat{T}_{\mathbf{kp}}$ can in principle couple to each other states of different layers within the same valley, or between opposite valleys. Since $T_\perp(\mathbf{q})$ decays exponentially with $q = |\mathbf{q}|$ [11], the leading terms are those with the least possible $\left|\mathbf{k} + \mathbf{G}^{(2)}\right|$ compatible with momentum conservation $\mathbf{k} + \mathbf{G}^{(2)} = \mathbf{p} + \mathbf{G}^{(1)}$. At small twist angle ϕ, only the intra-valley matrix elements, $\mathbf{p} \sim \mathbf{k}$, are sizeable, while the inter-valley ones are negligibly small, despite opposite valleys of different layers fold into the same point of the MBZ. For instance, if $\mathbf{p} \simeq \mathbf{K}_{+\phi}$ and $\mathbf{k} \simeq \mathbf{K}'_{-\phi}$, momentum conservation requires very large $\mathbf{G}^{(1)} = (2k+1)\,(\mathbf{G}_a^{(1)} - \mathbf{G}_b^{(1)})$ and $\mathbf{G}^{(2)} = (2k+1)\,(\mathbf{G}_b^{(2)} - \mathbf{G}_a^{(2)})$, thus an exponentially small $T_\perp(\mathbf{k} + \mathbf{G}^{(2)})$. The effective decoupling between the two valleys implies that the number of electrons within each valley is to high accuracy a conserved quantity, thus an emergent valley $U_v(1)$ symmetry [11, 69] that causes accidental band degeneracies along

high-symmetry lines in the MBZ [69, 30].

We can therefore just consider the intra-valley inter-layer scattering processes. We start with valley $\zeta = +1$, and thus require that $\mathbf{k}$ is close to $\mathbf{K}_{-\phi} = \mathbf{K}_2$ and $\mathbf{p}$ close to $\mathbf{K}_{+\phi} = \mathbf{K}_1$, see Fig. 2.1. Since the modulus of $\mathbf{k} \sim \mathbf{K}_2$ is invariant under C_{3z} rotations, where $C_{3z}(\mathbf{K}_2) = \mathbf{K}_2 - \mathbf{G}_1^{(2)}$ and $C_{3z}^2(\mathbf{K}_2) = \mathbf{K}_2 - \mathbf{G}_2^{(2)}$, maximisation of $T_\perp(\mathbf{k} + \mathbf{G}^{(2)})$ compatibly with momentum conservation leads to the following conditions, see Eq. (2.19),

$$\begin{aligned} &\mathbf{p} = \mathbf{k}\,, \\ &\mathbf{p} = \mathbf{k} - \mathbf{G}_a^{(2)} + \mathbf{G}_a^{(1)} = \mathbf{k} + \mathbf{G}_2\,, \\ &\mathbf{p} = \mathbf{k} - \mathbf{G}_b^{(2)} + \mathbf{G}_b^{(1)} = \mathbf{k} - \mathbf{G}_1\,. \end{aligned} \tag{2.25}$$

Upon defining $T(\mathbf{k}) \equiv t_\perp$, and using Eq. (2.25) to evaluate the phase factors in (2.24), we finally obtain

$$\hat{T}_{\mathbf{kp}}^{\zeta=+1} = \delta_{\mathbf{p},\mathbf{k}}\, \hat{T}_1 + \delta_{\mathbf{p},\mathbf{k}+\mathbf{G}_2}\, \hat{T}_2 + \delta_{\mathbf{p},\mathbf{k}-\mathbf{G}_1}\, \hat{T}_3\,, \tag{2.26}$$

where we explicitly indicate the valley index ζ, and

$$\hat{T}_1 = t_\perp \begin{pmatrix} 1 & 1 \\ 1 & 1 \end{pmatrix}, \hat{T}_2 = t_\perp \begin{pmatrix} 1 & \omega^* \\ \omega & 1 \end{pmatrix}, \hat{T}_3 = t_\perp \begin{pmatrix} 1 & \omega \\ \omega^* & 1 \end{pmatrix}, \tag{2.27}$$

with $\omega = \mathrm{e}^{2\pi i/3}$.

We now focus on the other valley, $\zeta = -1$, and take $\mathbf{k}$ close to $\mathbf{K}'_{-\phi} = -\mathbf{K}_1$, and $\mathbf{p}$ to $\mathbf{K}'_{\phi} = -\mathbf{K}_2$, see Fig. 2.1(d). In this case Eq. (2.25) is replaced by

$$\begin{aligned} &\mathbf{p} = \mathbf{k}\,, \\ &\mathbf{p} = \mathbf{k} - \mathbf{G}_2\,, \\ &\mathbf{p} = \mathbf{k} + \mathbf{G}_1\,, \end{aligned} \tag{2.28}$$

and

$$\hat{T}_{\mathbf{kp}}^{\zeta=-1} = \delta_{\mathbf{p},\mathbf{k}}\, \hat{T}_1^* + \delta_{\mathbf{p},\mathbf{k}-\mathbf{G}_2}\, \hat{T}_2^* + \delta_{\mathbf{p},\mathbf{k}+\mathbf{G}_1}\, \hat{T}_3^*\,. \tag{2.29}$$

Let us briefly discuss how one can take into account lattice relaxation, which as pointed out in the previous section tends to shrink the energetically unfavourable AA regions enlarging the Bernal stacked triangular domains in the moiré pattern. As a consequence, the inter- and intra-sublattice hopping processes acquire different amplitudes, which is taken into account by modifying the operators $\hat{T}_i$ in Eq. (2.27) according to

$$\begin{aligned} \hat{T}_1 \to T_1(u,u') &= \begin{pmatrix} u & u' \\ u' & u \end{pmatrix} = u\,\sigma_0 + u'\,\sigma_x\,, \\ \hat{T}_2 \to \hat{T}_2(u,u') &= \begin{pmatrix} u & u'\,\omega^* \\ u'\,\omega & u \end{pmatrix} = u\,\sigma_0 + u'\Big(\cos\frac{2\pi}{3}\,\sigma_x + \sin\frac{2\pi}{3}\,\sigma_y\Big), \\ \hat{T}_3 \to \hat{T}_3(u,u') &= \begin{pmatrix} u & u'\,\omega \\ u'\,\omega^* & u \end{pmatrix} = u\,\sigma_0 + u'\Big(\cos\frac{2\pi}{3}\,\sigma_x - \sin\frac{2\pi}{3}\,\sigma_y\Big), \end{aligned} \tag{2.30}$$

with u generally smaller than u'. In Fig. 2.6 we show the bandstructure of $\theta = 1.08^\circ$ twisted bilayer graphene obtained using the u, u' parameters of Ref. [53]. The bandstructure is in general similar to the one obtained with tight-binding, although the bands are particle-hole symmetric.

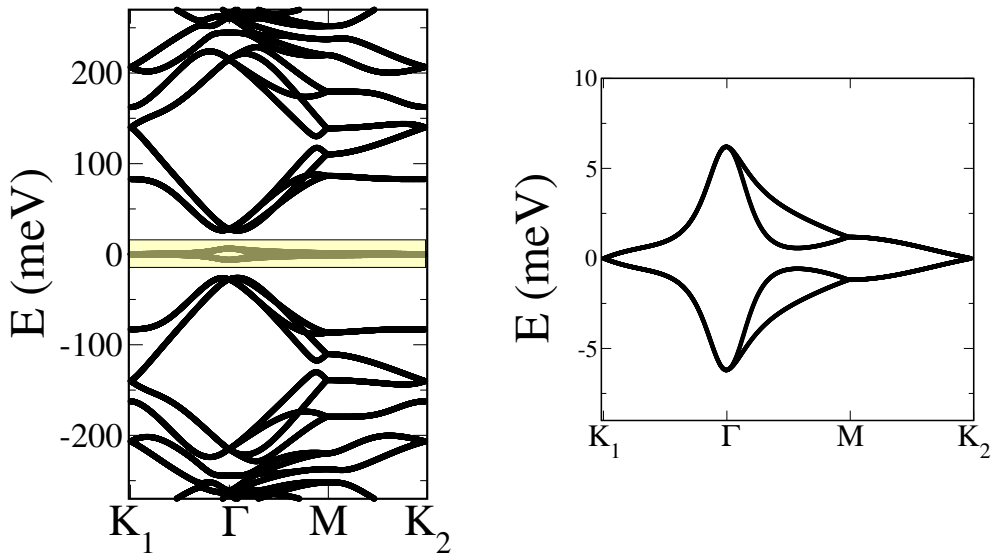

Figure 2.6: Bandstructure of *relaxed* twisted bilayer graphene at the magic angle $\theta \approx 1.08°$ obtained with the continuum model and using the parameters of Ref.[53]. On the left a zoom within the flat bands region.

The continuum model Hamiltonian can be made more accurate by introducing other terms in the Hamiltonian [70] which tend to break this additional particle-hole symmetry.
We conclude by showing how this formalism allows recovering the untwisted case, where $\mathbf{G}^{(1)}_{1/2} = \mathbf{G}^{(2)}_{1/2}$, so that, through Eq. (2.19), $\mathbf{G}_1 = \mathbf{G}_2 = \mathbf{0}$, and therefore

$$\hat{T}_{\mathbf{kp}} \xrightarrow[\phi \to 0]{} \delta_{\mathbf{p},\mathbf{k}} \left(\hat{T}_1 + \hat{T}_2 + \hat{T}_3 \right) = 3 t_\perp \, \delta_{\mathbf{p},\mathbf{k}} \begin{pmatrix} 1 & 0 \\ 0 & 1 \end{pmatrix}, \tag{2.31}$$

which is what one would expect from an AA stacked bilayer.

3

Emergent symmetries and Wannier orbitals in twisted bilayer graphene

Because of the very non-dispersive character of the flat bands (FBs), it is tempting to invoke an important role of strong electronic correlations in the physics of magic angle tBLG [8]. Despite mean field calculations such as Hartree-Fock have been performed with the continuum model, the common approach dealing with strong correlations is adding electron-electron repulsion on top of a tight-binding lattice model. However, the large number of atoms contained in the unit cell makes it challenging, if not impossible, to carry out a straight many-body calculation even in the already simplified lattice model. A further approximation may consist in focusing just on the four flat bands, an approach which requires to first identify their corresponding Wannier functions. Surprisingly, even such a preliminary step turns out to be rather difficult and, to some extent, controversial [71, 72, 73, 74, 75, 76]. The scope of this chapter is to shed light on this debated issue. In Section. 3.1 we work out what are the symmetries of tBLG. Then, in Section. 3.2 we show that due to the peculiarities of the Bloch states at the high-symmetry points it is not possible to build a minimal model of the flat bands which employs less than 8 Wannier orbitals. In Section. 3.3 we propose a 8 orbitals (per valley) model , able to faithfully describe the flat bands physics and topology.

3.1 Emergent symmetries in twisted bilayer graphene

As shown in Fig. 3.1, the point group of twisted bilayer graphene depends on the twisting center. If the twisted bilayer is obtained from AA stacking upon rotation around the center of two overlapping basic graphene hexagons, the point-group symmetry of the superlattice is D_6, which reduces to D_3 when the rotation center is around a vertical C-C bond [77, 71]. If instead the twisting center is the midpoint between two carbon atoms in the same layer, the group is D_2. Finally, whenever the layers are rotated around non-high symmetry points (the situation more likely to occur in experiments), the point group of the lattice contains only a reflection with respect to the rotation axis. This is puzzling since some of the most interesting features of a bandstructure are those protected by symmetry. As an example, if the group was D_3, the Dirac nodes at the **K** points would loose symmetry protection and would be gapped by perturbations

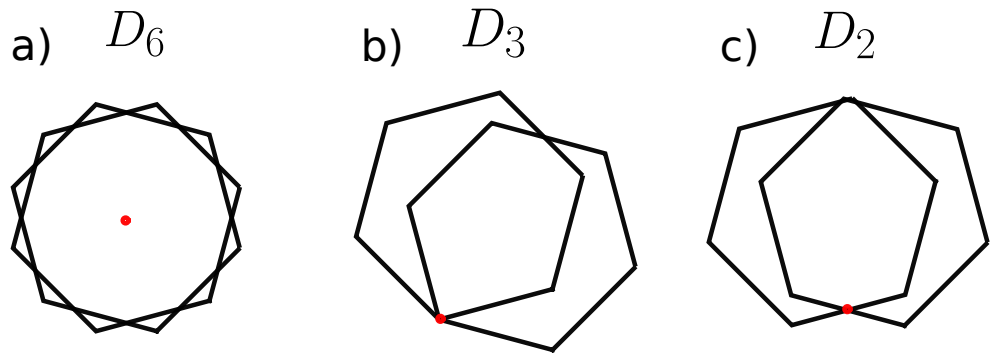

Figure 3.1: Point group of twisted bilayer graphene obtained by twisting with respect to three different twisting centers. a) the twisting center is the center of two overlapping hexagons and the point group of the lattice is D_6. b) the rotation point is a vertical C-C bond and the point group of the lattice is D_3. c) the lattice is twisted with respect to the mid point between two carbon atoms and the point group of the lattice is D_2.

such as an electric field perpendicular to the graphene layers. In this section we show that at small angles, twisted bilayer graphene develops a set of 'emergent' symmetries, which are completely independent on the twisting center and robust with respect to lattice relaxation. The emergence of these symmetries is general to any long-wavelength moiré material with striking consequences also on the physics of twisted TMDs (see Chapter 5).

3.1.1 Emergent D_6 symmetry

We start by recalling the symmetries and irreducible representations of the group D_6, which, as we'll see in the following, emerges in the low energy Bloch states despite the lattice having no symmetries. Specifically, resolving the action of each symmetry operation in the indices that identify the two layers, 1 and 2, the two sublattices within each layer, A and B, and, finally, the two sublattices AB and BA of the moiré superlattice, we have that:

- the rotation C_{3z} by 120° degrees around the z-axis is diagonal in all indices, 1 and 2, A and B, AB and BA;
- the C_{2x} rotation by 180° degrees around the x-axis interchanges 1 with 2, A with B, but is diagonal in AB and BA;
- the C_{2y} rotation by 180° degrees around the y-axis interchanges 1 with 2, AB with BA, but is diagonal in A and B;
- finally, the action of a C_{2z} rotation by 180° degrees around the z-axis is a composite symmetry operation obtained by noting that $C_{2z} = C_{2x} \times C_{2y}$.

In Table 3.1 we list the irreducible representations (irreps) of the D_6 space group and the action on each of them of the symmetry transformations C_{3z}, C_{2x} and C_{2y}. The D_3 group differ from the D_6 one because it lacks of the C_{2z} rotations being generated by the C_{3z} and C_{2y} symmetries only. In order to prove that the system is developing an emergent D_6 symmetry, we relaxed a $\theta = 1.08°$ twisted bilayer whose supercell was built twisting around a vertical C-C bond. In this case, the unrelaxed bilayer posses D_3 symmetry which is in general not preserved during relaxation. Then, we analyze the symmetries of the Bloch states at the high-symmetry points of the spectrum. The little group L at $\mathbf{\Gamma}$ coincides with the full G, while, at $\mathbf{K}_1$ or $\mathbf{K}_2$, L is generated only by C_{3z} for both G=D_6 and G=D_3. It follows that the symmetry properties of the Bloch

	C_{3z}	C_{2x}	C_{2y}
$A_1(1)$	+1	+1	+1
$A_2(1)$	+1	-1	-1
$B_1(1)$	+1	+1	-1
$B_2(1)$	+1	-1	+1
$E_1(2)$	$\begin{pmatrix}\cos\phi & -\sin\phi\\ \sin\phi & \cos\phi\end{pmatrix}$	$\begin{pmatrix}+1 & 0\\ 0 & -1\end{pmatrix}$	$\begin{pmatrix}-1 & 0\\ 0 & +1\end{pmatrix}$
$E_2(2)$	$\begin{pmatrix}\cos\phi & -\sin\phi\\ \sin\phi & \cos\phi\end{pmatrix}$	$\begin{pmatrix}1 & 0\\ 0 & -1\end{pmatrix}$	$\begin{pmatrix}1 & 0\\ 0 & -1\end{pmatrix}$

Table 3.1: Nontrivial irreducible representations of the space group D_6. Each representation has the degeneracy shown in parenthesis. We also list the action of the symmetry operations for each representation, where $\phi = 2\pi/3$.

wavefunctions at $\mathbf{\Gamma}$ can discriminate between G=D_6 and G=D_3 or any other group.
We thus analyze the Bloch states at $\mathbf{\Gamma}$ within the flat bands. Looking at Fig. 3.2, one notes that the Bloch functions have negligible amplitude in the AA zones, being mostly localized in AB/BA [78]. Most importantly, one finds that the Bloch function is not only invariant under C_{3z}, but also possesses well defined symmetry properties under C_{2z} and C_{2x}, specifically it is odd under the former, cf. panel layer #1 A with panel layer #1 B, and even under the latter, cf. panel #1 A with panel layer #2 B. Similarly, the other state within the lower doublet (not shown) is still even under C_{2x}, but also even under C_{2z}. That doublet thus transforms with respect to C_{2x} as an s-orbital. On the contrary, the upper doublet is odd under C_{2x}, thus transforming as a p_z-orbital, one state being even and the other odd under C_{2z}. We thus conclude that close to the charge neutrality point the effective symmetry group is actually D_6 [77], and hence contains also C_{2z}, even if the relaxed structure lacks any point symmetry.

3.1.2 $U_v(1)$ valley symmetry

We stress that the double degeneracy of the flat bands at $\mathbf{\Gamma}$ is generically not to be expected even assuming D_6 symmetry. The accidental degeneracy is due to the fact that the coupling between different Dirac points in different layers, effectively vanishes at small twist angles [11], even though symmetry does not prohibit this coupling to be finite. This phenomenon corresponds to an additional emergent symmetry, dynamical in nature, often referred as valley charge conservation $U_v(1)$ symmetry. The mini Brillouin zone (MBZ) that corresponds to the real space geometry of Fig. 2.2 and its relationship with the original graphene Brillouin zones are shown in Fig. 2.1. Because of the chosen geometry, the Dirac point $K_\phi(K'_\phi)$ of the top layer and $K'\_\phi(K_{-\phi})$ of the bottom one fold onto the same point, K_1 or K_2, of the MBZ, so that a finite matrix element of the Hamiltonian between them is allowed by symmetry. Nevertheless, the matrix element of the one-body component of the Hamiltonian is negligibly small at small twist angles, so that the two Dirac points or *valleys*, remain effectively independent of each other. This implies that the operator

$$\Delta N_v = N_1 - N_2\,, \tag{3.1}$$

where N_1 and N_2 are the occupation numbers of each valley, must commute with the non-interacting Hamiltonian of the tBLG at small angles. That operator is in fact the generator of the $U_v(1)$ symmetry. As we will see in more details in the following Chapter (see 4.0.1), the interplay

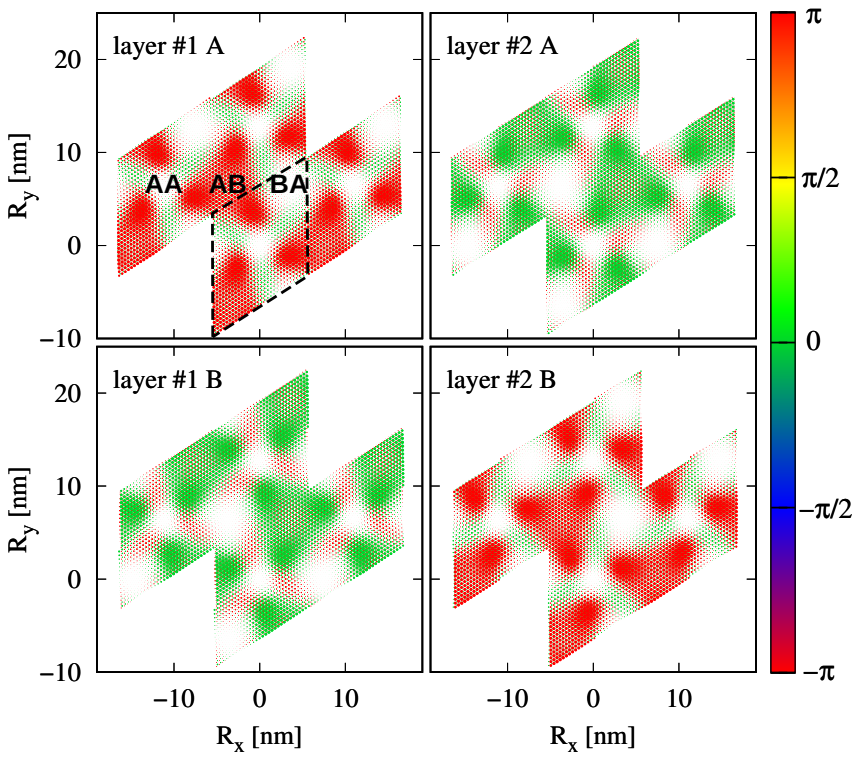

Figure 3.2: Layer (#1-#2) and sublattice (A-B) components of one state within the lowest-energy doublet at $\mathbf{\Gamma}$ in the flat bands. The colour of each point indicates its complex phase, while its size is a measure of its square modulus. Each unit cell (black dashed line in top left panel) has been replicated 3 times to improve visibility. This eigenstate is invariant under C_{3z}, even with respect to C_{2x} and odd under C_{2z}.

between the valley symmetry and C_{2y} is responsible for the additional two-fold degeneracies beyond those of Table 3.1 in both electron band structure and phonon spectra along all the points in the MBZ invariant under that symmetry.

3.2 Symmetry analysis of the Bloch states and Wannier obstruction

In Fig. 3.3 we show the electronic structure and the symmetries of the Bloch states obtained with tight-binding calculations on the relaxed lattice (see Section 2.3.1). The colored circles and triangles at the $\mathbf{\Gamma}$ and $\mathbf{K}$ points, respectively, indicate the irreps that transform like the corresponding Bloch states. As mentioned before at $\mathbf{\Gamma}$ the FBs consist of two doublets, the lower corresponding to the s-like irreps $A_1 + B_1$, and the upper to the p_z-like $A_2 + B_2$. Right above and below the FBs, we find at $\mathbf{\Gamma}$ two quartets, each transforming like $E_1 + E_2$. At $\mathbf{K}$, the FBs are degenerate and form a quartet $E + E$. Consistently with the D_3 little group containing C_{3z} and C_{2y}, at $\mathbf{K}$ we find either quartets, like at the FBs, made of degenerate pairs of doublets, each transforming like E, or doublets transforming like $A_1 + A_2$, where A_1 and A_2 differ in the parity under C_{2y}. As mentioned above, this overall doubling of degeneracies beyond their expected D_6 space group irreps, reflects the valley $U_v(1)$ symmetry. We end by remarking that the so-called 'fragile' topology [75, 77, 76, 79], diagnosed by the odd winding of the Wilson loop (WL) [75], is actually robust against lattice corrugations [80] and relaxation, as shown by panel (c) in Fig. 3.3.

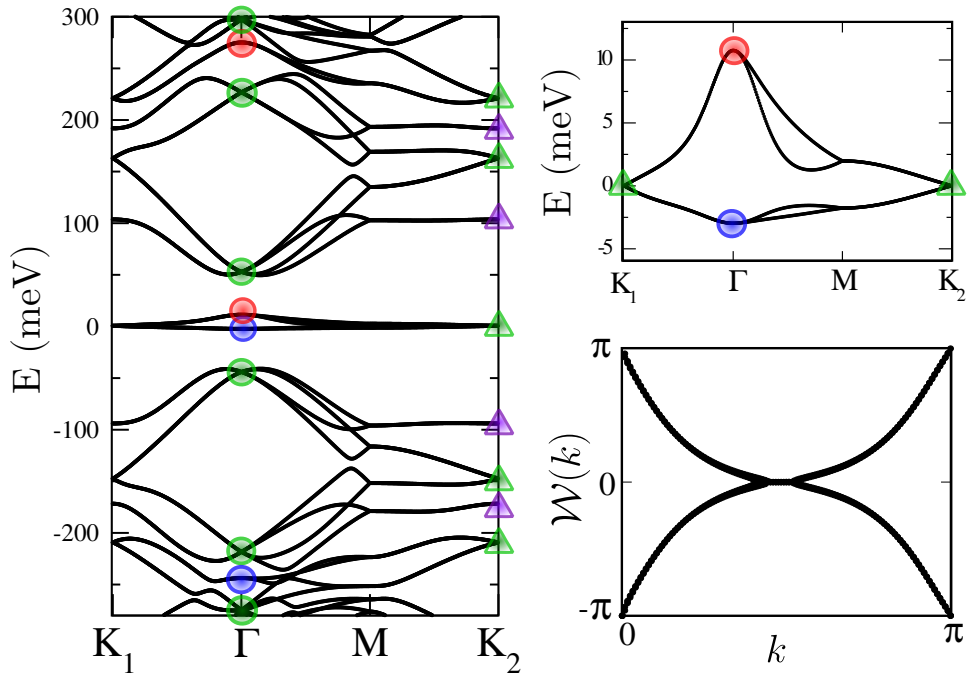

Figure 3.3: (a) Electronic band structure of twisted bilayer graphene at the angle $\theta = 1.08$ after full atomic relaxation. The charge neutrality point is the zero of energy. The irreps at the $\mathbf{\Gamma}$ point are encoded by colored circles, where blue, red and green stand for the $A_1 + B_1$, $A_2 + B_2$ and $E_1 + E_2$ irreps of the D_6 space group, respectively. A_1 and B_1 transform as s-like orbitals with respect to C_{2x} while A_2 and B_2 as p_z orbitals. The two dimensional irreps instead transform as $p_x \pm ip_y$ orbitals. At the $\mathbf{K}_1$ point the E and $A_1 + A_2$ irreps of the little group D_3 are represented by green and violet triangles, respectively. b) Zoom in the FBs region. c) Wilson loop of the four FBs as function of $k = G_2/\pi$.

3.2.1 Wannier Orbitals

There is wide consensus [75, 74, 72, 71, 78] that a proper description of the band structure can be obtained by just assuming that the Wannier orbitals of the flat bands are centered on the AB and BA sites of the honeycomb moiré superlattice, even though their actual weight is often mostly localized on the AA regions. In the following we will denote as L_1 and L_2 the moiré lattice vectors, which span the triangular lattice formed by the AA sites with coordinates $\mathbf{R}_i$ and $\mathbf{R}'_i$. We parametrize the Wannier orbitals $\Psi^{AB}(\mathbf{r} - \mathbf{r}_{AB})$ and $\Psi^{BA}(\mathbf{r} - \mathbf{r}_{BA})$ centered around the AB and BA sites with coordinates $\mathbf{r}_{AB}$ and $\mathbf{r}_{BA}$, respectively, through the functions $\psi_i^{AB}(\mathbf{r} - \mathbf{R}_i)$ and $\psi_i^{BA}(\mathbf{r} - \mathbf{R}'_i)$, $i = 1, 2, 3$, centered instead around AA, see Fig. 3.4. In particular we shall assume that ψ_1^{AB} and ψ_3^{BA} are centered at the origin, taken to coincide with AA center $\mathbf{R}_1 = \mathbf{R}'_3 = \mathbf{0}$, so that $\mathbf{R}_2 = -\mathbf{L}_1$, $\mathbf{R}'_2 = \mathbf{L}_2$, $\mathbf{R}_3 = \mathbf{R}'_1 = \mathbf{L}_1 - \mathbf{L}_2$, $\mathbf{r}_{AB} = (\mathbf{L}_1 - 2\mathbf{L}_2)/3$ and $\mathbf{r}_{BA} = (2\mathbf{L}_1 - \mathbf{L}_2)/3$.
It follows that the most general Bloch function $\Phi_{\mathbf{k}}(\mathbf{r})$ can be written as

$$\begin{aligned}\Phi_{\mathbf{k}}(\mathbf{r}) &= \frac{1}{\sqrt{V}} \sum_{\mathbf{R}} \left(u_{\mathbf{k}}\, \mathrm{e}^{-i\mathbf{k}\cdot(\mathbf{R}+\mathbf{r}_{AB})}\, \Psi^{AB}(\mathbf{r} - \mathbf{r}_{AB} - \mathbf{R}) + v_{\mathbf{k}}\, \mathrm{e}^{-i\mathbf{k}\cdot(\mathbf{R}+\mathbf{r}_{BA})}\, \Psi^{BA}(\mathbf{r} - \mathbf{r}_{BA} - \mathbf{R}) \right) \\ &= \frac{1}{\sqrt{V}} \sum_{\mathbf{R}} \mathrm{e}^{-i\mathbf{k}\cdot\mathbf{R}} \left(u_{\mathbf{k}}\, \psi_{\mathbf{k}}^{AB}(\mathbf{r} - \mathbf{R}) + v_{\mathbf{k}}\, \psi_{\mathbf{k}}^{BA}(\mathbf{r} - \mathbf{R}) \right) \equiv \frac{1}{\sqrt{V}} \sum_{\mathbf{R}} \mathrm{e}^{-i\mathbf{k}\cdot\mathbf{R}}\, \phi_{\mathbf{k}}(\mathbf{r} - \mathbf{R}) \,,\end{aligned} \tag{3.2}$$

where $|u_{\mathbf{k}}|^2 + |v_{\mathbf{k}}|^2 = 1$, V is the area, and

$$\begin{aligned}\psi_{\mathbf{k}}^{AB}(\mathbf{r}) &= \psi_1^{AB}(\mathbf{r})\, \mathrm{e}^{-i\mathbf{k}\cdot(\mathbf{L}_1 - 2\mathbf{L}_2)/3} + \psi_2^{AB}(\mathbf{r})\, \mathrm{e}^{-i\mathbf{k}\cdot(\mathbf{L}_1 + \mathbf{L}_2)/3} + \psi_3^{AB}(\mathbf{r})\, \mathrm{e}^{-i\mathbf{k}\cdot(-2\mathbf{L}_1 + \mathbf{L}_2)/3} \,, \\ \psi_{\mathbf{k}}^{BA}(\mathbf{r}) &= \psi_1^{BA}(\mathbf{r})\, \mathrm{e}^{-i\mathbf{k}\cdot(-\mathbf{L}_1 + 2\mathbf{L}_2)/3} + \psi_2^{BA}(\mathbf{r})\, \mathrm{e}^{-i\mathbf{k}\cdot(-\mathbf{L}_1 - \mathbf{L}_2)/3} + \psi_3^{BA}(\mathbf{r})\, \mathrm{e}^{-i\mathbf{k}\cdot(2\mathbf{L}_1 - \mathbf{L}_2)/3} \,.\end{aligned}$$

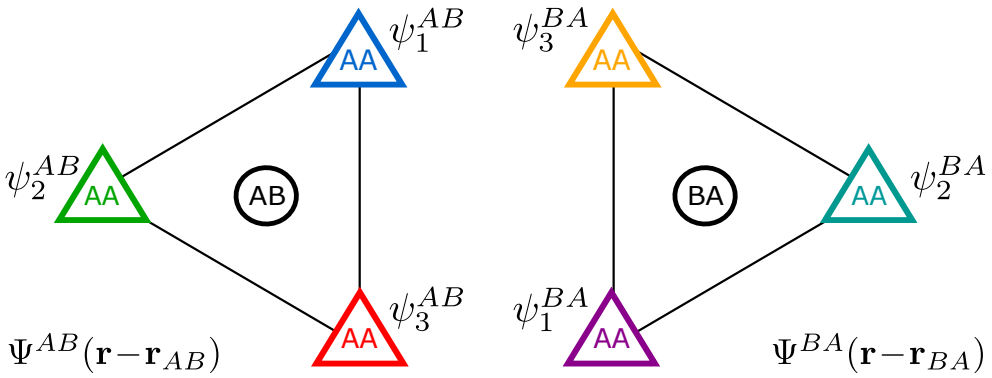

Figure 3.4: Pictorial view of the Wannier functions $\Psi^{AB}(\mathbf{r}-\mathbf{r}_{AB})$ and $\Psi^{BA}(\mathbf{r}-\mathbf{r}_{BA})$ centered at AB and BA sites, respectively. The triangles represent wavefunction components centered around the AA regions, while the combination of the three triangles defines the Wannier orbital, centered instead around AB, left, or BA, right.

We note that, even though $\phi_{\mathbf{k}}(\mathbf{r}-\mathbf{R})$ might be confused with the Wannier function centred in the triangular site $\mathbf{R}$, yet it is not so because of the explicit dependence upon momentum $\mathbf{k}$. In particular, under a symmetry transformation $\mathcal{G}$, such that $\mathbf{r}\to\mathbf{r}_G$ and $\mathbf{k}\to\mathbf{k}_G$,

$$\mathcal{G}\Big(\Phi_{\mathbf{k}}(\mathbf{r})\Big)=\frac{1}{\sqrt{V}}\sum_{\mathbf{R}}\mathrm{e}^{-i\mathbf{k}_G\cdot\mathbf{R}}\,\phi_{\mathbf{k}}(\mathbf{r}_G-\mathbf{R})\,, \tag{3.3}$$

the outcome simplifies only at the high-symmetry $\mathbf{k}$-points, i.e., when $\mathbf{k}_G\equiv\mathbf{k}$ apart from a reciprocal lattice vector, in which case

$$\mathcal{G}\Big(\Phi_{\mathbf{k}}(\mathbf{r})\Big)=\Phi_{\mathbf{k}}(\mathbf{r}_G)\,. \tag{3.4}$$

Going back to the definitions (3.3) and (3.3), we find for the high-symmetry points shown in Fig. 2.1,

$$\begin{aligned}\psi^{AB}_{\mathbf{\Gamma}}(\mathbf{r})&=\psi^{AB}_1(\mathbf{r})+\psi^{AB}_2(\mathbf{r})+\psi^{AB}_3(\mathbf{r})\,,\\ \psi^{BA}_{\mathbf{\Gamma}}(\mathbf{r})&=\psi^{BA}_1(\mathbf{r})+\psi^{BA}_2(\mathbf{r})+\psi^{BA}_3(\mathbf{r})\,,\end{aligned} \tag{3.5}$$

at $\mathbf{\Gamma}$, while at $\mathbf{K}_2$,

$$\begin{aligned}\psi^{AB}_{\mathbf{K}_2}(\mathbf{r})&=\omega\Big(\psi^{AB}_1(\mathbf{r})+\omega\,\psi^{AB}_2(\mathbf{r})+\omega^*\,\psi^{AB}_3(\mathbf{r})\Big),\\ \psi^{BA}_{\mathbf{K}_2}(\mathbf{r})&=\omega^*\Big(\psi^{BA}_1(\mathbf{r})+\omega^*\,\psi^{BA}_2(\mathbf{r})+\omega\,\psi^{BA}_3(\mathbf{r})\Big),\end{aligned} \tag{3.6}$$

and finally at $\mathbf{K}_1$,

$$\begin{aligned}\psi^{AB}_{\mathbf{K}_1}(\mathbf{r})&=\omega^*\Big(\psi^{AB}_1(\mathbf{r})+\omega^*\,\psi^{AB}_2(\mathbf{r})+\omega\,\psi^{AB}_3(\mathbf{r})\Big),\\ \psi^{BA}_{\mathbf{K}_1}(\mathbf{r})&=\omega\Big(\psi^{BA}_1(\mathbf{r})+\omega\,\psi^{BA}_2(\mathbf{r})+\omega^*\,\psi^{BA}_3(\mathbf{r})\Big),\end{aligned} \tag{3.7}$$

where $\omega=\mathrm{e}^{i2\pi/3}$.

Since the Wannier functions are centred at the vertices of the hexagons, where the symmetry is C_3 irrespective of the global symmetry, one could be tempted to rationalize [71, 72] the FBs

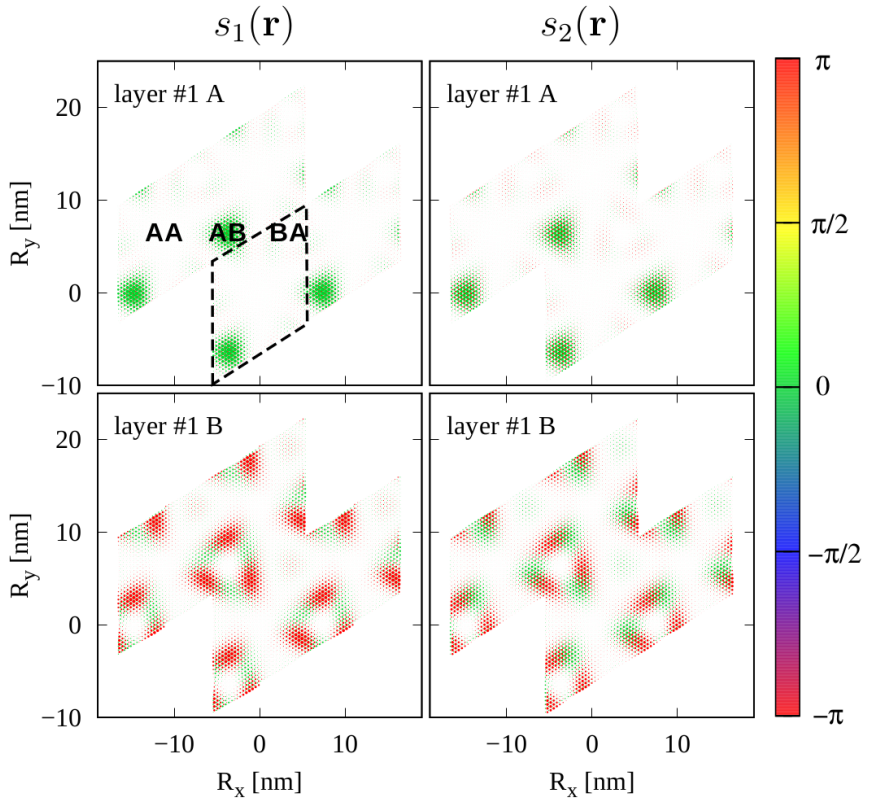

Figure 3.5: Layer #1 and sublattice (A-B) components of $s_1(\mathbf{r})$ (left panel) and $s_2(\mathbf{r})$ (right panel). The colour of each point indicates its complex phase, while its size is a measure of its square modulus. Each unit cell (black dashed line in top left panel) has been replicated 3 times to improve visibility.

mathbfΓ point double degeneracy as due to two different Ψ^{AB}, as well as Ψ^{BA}, see Fig. 3.4, which transform as the two-dimensional irreducible representation of C_3. We find that this assumption is not correct in our case because as we have shown in Section. 3.1.1 the wavefunctions within the flat bands at Γ are instead invariant under C_{3z}, which implies that the Wannier functions must transform as one of the singlet irreps of C_3. Assuming therefore that all the Wannier functions are invariant under C_{3z}, we can parametrize the functions $\psi_i^{AB}(\mathbf{r})$, $i = 1, 2, 3$, of Fig. 3.4 as follows

$$\begin{aligned}
\psi_1^{AB}(\mathbf{r}) &= A(\mathbf{r}) + E_{+1}(\mathbf{r}) + E_{-1}(\mathbf{r}),\\
\psi_2^{AB}(\mathbf{r}) &= A(\mathbf{r}) + \omega\, E_{+1}(\mathbf{r}) + \omega^*\, E_{-1}(\mathbf{r}),\\
\psi_3^{AB}(\mathbf{r}) &= A(\mathbf{r}) + \omega^*\, E_{+1}(\mathbf{r}) + \omega\, E_{-1}(\mathbf{r}),
\end{aligned} \tag{3.8}$$

where $A(\mathbf{r})$ is invariant under C_3, while $E_{\pm1}(\mathbf{r})$ transforms with eigenvalue $\omega^{\pm1} = e^{\pm i2\pi/3}$. Recalling that $\psi_{n+1}^{AB}(\mathbf{r} - \mathbf{L}_2) = C_3(\psi_n^{AB}(\mathbf{r} - \mathbf{0}))$ ($n = 1, 2, 3$ and $n + 3 = n$), one can readily show that the Wannier function $\Psi^{AB}(\mathbf{r})$ shown in Fig. 3.4 is indeed invariant under C_{3z}. Similarly, for $\psi_i^{BA}(\mathbf{r})$ we introduce the functions $A'(\mathbf{r})$ and $E'_{\pm1}(\mathbf{r})$. It follows that the Eqs. (3.5) and (3.6) simplify to

$$\begin{aligned}
\psi_{\mathbf{\Gamma}}^{AB}(\mathbf{r}) &= 3A(\mathbf{r}),\\
\psi_{\mathbf{K}_2}^{AB}(\mathbf{r}) &= 3\omega\, E_{-1}(\mathbf{r}),\\
\psi_{\mathbf{K}_1}^{AB}(\mathbf{r}) &= 3\omega^*\, E_{+1}(\mathbf{r}),
\end{aligned} \tag{3.9}$$

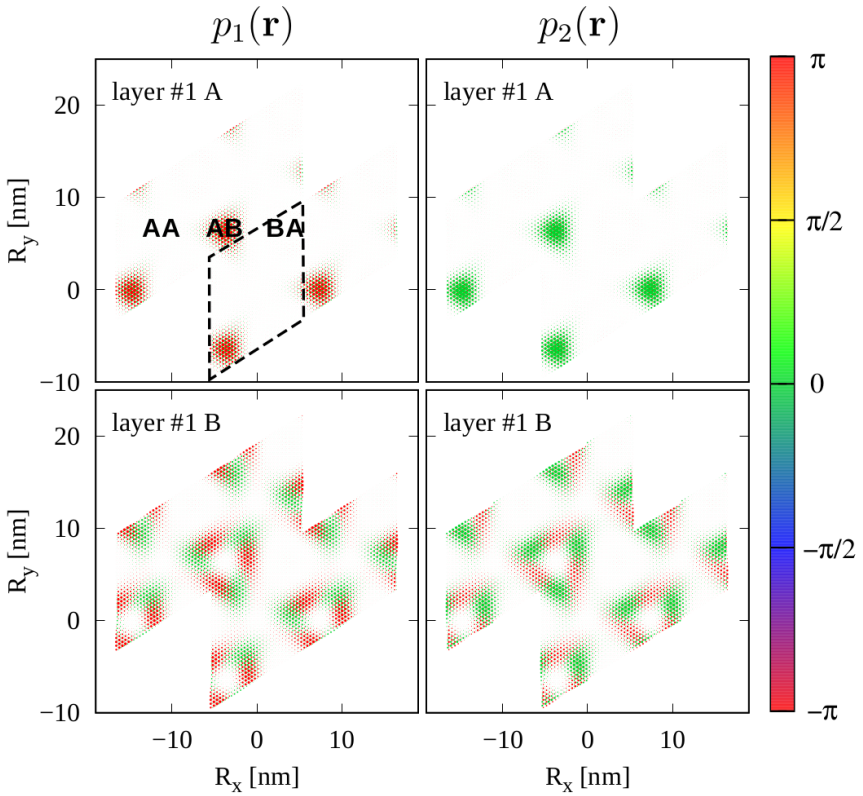

Figure 3.6: Layer #1 and sublattice (A-B) components of $p_1(\mathbf{r})$ (left panel) and $p_2(\mathbf{r})$ (right panel). The colour of each point indicates its complex phase, while its size is a measure of its square modulus. Each unit cell (black dashed line in top left panel) has been replicated 3 times to improve visibility

for AB, and

$$\begin{aligned}\psi^{BA}_{\mathbf{\Gamma}}(\mathbf{r}) &= 3A'(\mathbf{r})\,,\\ \psi^{BA}_{\mathbf{K}_2}(\mathbf{r}) &= 3\omega^*\,E'_{+1}(\mathbf{r})\,,\\ \psi^{BA}_{\mathbf{K}_1}(\mathbf{r}) &= 3\omega\,E'_{-1}(\mathbf{r})\,,\end{aligned} \tag{3.10}$$

for BA. Therefore, studying the Bloch functions at the different high-symmetry points gives direct access to $A(\mathbf{r})$ as well as $E_{\pm1}(\mathbf{r})$, as we show in what follows. If so, AB and BA being equivalent, the function $\phi_{\mathbf{k}}(\mathbf{r})$, see Eqs. (3.2), (3.5), (3.9) and (3.10), at $\mathbf{\Gamma}$ can be written as

$$\phi_{\mathbf{\Gamma}}(\mathbf{r}) = 3A(\mathbf{r}) \pm 3A'(\mathbf{r})\,, \tag{3.11}$$

i.e., sum or difference of the AB and BA components. Since the two combinations cannot be degenerate, in order to describe the band structure we need at least two different s-like and two different p_z-like orbitals for each sublattice AB or BA. It thus follows that there must be two additional doublets above or below the flat-bands, one of s-type and another of p_z-type, both invariant under C_{3z}. As can be seen in Fig. 3.3, above the flat-bands at $\mathbf{\Gamma}$ there are two fourfold degenerate levels that actually transform as the two-dimensional irreducible representation, and hence are not invariant under C_{3z}. The next two states (upper red circle) have instead the right symmetry properties, i.e., they are invariant under three-fold rotations and have well defined parity, actually odd, under C_{2x} (one being even and one odd with respect to C_{2z}). This doublet is therefore the partner of the p_z-doublet in the flat bands. The same holds in the lower energy bands (lower blue circle). With the only difference that the doublet is now even under C_{2x}, hence it is the partner of the s-doublet in the flat bands. Let us focus for instance on the

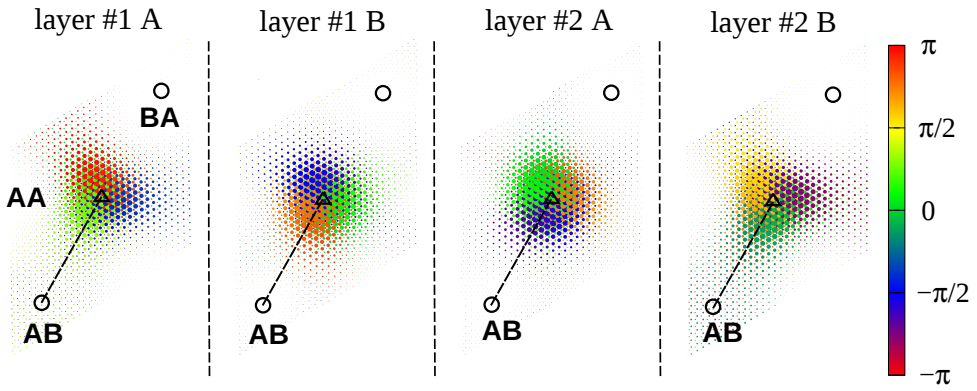

Figure 3.7: Layer and sublattice components in the unit cell of one of the two degenerate Bloch functions at $\mathbf{K}_2$ whose Wannier orbitals are centred on AB.

two s-orbitals, and denote $3A(\mathbf{r})$ either as $s_1(\mathbf{r})$ or $s_2(\mathbf{r})$, and similarly $3A'(\mathbf{r})$ as $s'_1(\mathbf{r})$ or $s'_2(\mathbf{r})$. We assume that the s-doublet below the FBs corresponds to the AB+BA combination, hence, through Eqs. (3.9) and (3.10),

$$\begin{aligned} \phi_{\mathbf{\Gamma}}^{(1+)}(\mathbf{r}) &= s_1(\mathbf{r}) + s'_1(\mathbf{r})\,, \\ \phi_{\mathbf{\Gamma}}^{(2+)}(\mathbf{r}) &= s_2(\mathbf{r}) + s'_2(\mathbf{r})\,. \end{aligned} \tag{3.12}$$

If $\phi_{\mathbf{\Gamma}}^{(1+)}$ is chosen to be even under C_{2z}, so that $\phi_{\mathbf{\Gamma}}^{(2+)}$ is odd, then

$$s'_1 = \mathscr{C}_{2z}(s_1)\,, \qquad s'_2 = -\mathscr{C}_{2z}(s_2)\,. \tag{3.13}$$

The s-doublet within the FBs must therefore be the AB-BA combination

$$\begin{aligned} \phi_{\mathbf{\Gamma}}^{(1-)}(\mathbf{r}) &= s_1(\mathbf{r}) - s'_1(\mathbf{r})\,, \\ \phi_{\mathbf{\Gamma}}^{(2-)}(\mathbf{r}) &= s_2(\mathbf{r}) - s'_2(\mathbf{r})\,, \end{aligned} \tag{3.14}$$

so that $\phi_{\mathbf{\Gamma}}^{(1-)}$ is odd under C_{2z}, while $\phi_{\mathbf{\Gamma}}^{(2-)}$ even. It follows that taking either the sum or the difference between two states belonging to different s-doublets with opposite parity under C_{2z}, we should find wavefunctions centred either in AB or BA. This is indeed the case. In Fig. 3.5 we show the layer #1 sublattice components of $s_1(\mathbf{r})$, left panel, and $s_2(\mathbf{r})$, right panel. The components on layer #2 can be obtained through C_{2x}, and the functions $s'_1(\mathbf{r})$ and $s'_2(\mathbf{r})$ on the sublattice BA through C_{2z}. We can repeat a similar analysis to find the two p_z-type functions, $p_1(\mathbf{r})$ and $p_2(\mathbf{r})$, which are shown in Fig. 3.6.

3.2.2 Bloch functions at K

At the high-symmetry points $\mathbf{K}_2$ and $\mathbf{K}_1 = -\mathbf{K}_2$ the AB and BA Wannier functions are effectively decoupled and degenerate. However, the outcome of numerical diagonalization is a generic linear combination of the degenerate levels. Therefore, in order to identify AB and BA components, we introduced a small perturbation in the Hamiltonian that makes AB and BA inequivalent while preserving the C_{3z} symmetry:

$$V(\mathbf{r}) = -\sum_{j=1}^{3} 2V_0 \sin(\mathbf{g}_j \cdot \mathbf{r}), \tag{3.15}$$

where $\mathbf{g}_1 = \mathbf{G}_1$, $\mathbf{g}_2 = \mathbf{G}_2$, $\mathbf{g}_3 = -\mathbf{G}_1 - \mathbf{G}_2$, and $V_0 \approx 1$ μeV. This function is maximum in AB, minimum in BA and zero in AA. By doing so, the fourfold degenerate states at $\mathbf{K}_{1/2}$ are split by a tiny gap (less than 0.2 μeV) in two doublets, the lower/upper one composed by Bloch states that are combination of BA/AB Wannier orbitals only. In such a way, we can directly obtain the proper lattice-symmetric functions $E_{\pm1}(\mathbf{r})$ and $E'_{\pm1}(\mathbf{r})$ through Eqs. (3.9) and (3.10). Since there are four states at $\mathbf{K}_{1/2}$, there will be two different $E_{+1}(\mathbf{r})$,and similarly for all the other components. In Fig. 3.7 we show the layer and sublattice components of one of the two degenerate Bloch functions at $\mathbf{K}_2$ centred on AB. We note that this Bloch functions transforms under C_{3z} as the expected $E_{-1}(\mathbf{r})$, see Eq. (3.9). We did check that all other Bloch functions at $\mathbf{K}_2$ and $\mathbf{K}_1$ are compatible with Eqs. (3.9) and (3.10).

3.2.3 Wannier obstruction

In the previous section we have shown that each pair of Bloch states at $\mathbf{\Gamma}$ has a partner higher/lower in energy. In other words, considering the additional valley degree of freedom and that the orbitals are centered on the honeycomb formed by the AB/BA regions, atleast eight Wannier orbitals are necessary to faithfully generate the physics around $\mathbf{\Gamma}$. This phenomenon is known as 'Wannier obstruction' [74, 75, 76] because although the system exhibit a set of four energetically isolated bands, they cannot be described by four Wannier orbitals only. The existence of such an obstruction in twisted bilayer graphene has been proved with several methods, most of them introducing the concept of 'fragile topology' [81]. In this picture, the flat bands are the result of a series of avoided crossings between energy levels within the flat bands and the bands above and below. As a consequence of this level repulsion, energy levels are compressed to form the flat bands around neutrality. The complex interference between these levels is finely tuned by the twisting angle. We conclude by stressing that the same symmetry partners of the FB levels at $\mathbf{\Gamma}$ are no less than 300 meV away from them, and in between there are several states with different symmetry. However, as soon as we move away from $\mathbf{\Gamma}$ all those states will be coupled to each other by the Hamiltonian, and thus a description in terms only of few of them is hardly possible. This implies that the number of Wannier orbitals per valley might be even larger than four.

3.3 Wannier model of the flat bands physics in twisted bilayer graphene

As mentioned in Sec. 3.2.3, it is not possible to build a Wannier model for the flat bands of tBLG which contains only four orbitals. Here, inspired by the symmetries of the Bloch states at the high-symmetry points, we enlarge the 8 orbital model proposed previously to include twice as many orbitals. The resulting 16 orbitals model faithfully describes the flat bands physics and topology.

3.3.1 16 orbitals model

All the Wannier orbitals (WOs) considered in this model are centered at the Wyckoff positions $2c$ of the moiré triangular superlattice, i.e., at the AB and BA region centers. While a variety of WOs centered at different Wyckoff positions has been proposed [78, 74, 77, 71, 76, 72, 73, 75, 64], our simple assumption is well suited for our purposes. The site symmetry at the Wyckoff positions $2c$ is D_3, and includes only C_{3z} and C_{2x} with irreps A_1, A_2 and E. Inspired by the symmetries of the Bloch states at the high-symmetry points, see Sec. 3.2), we consider two A_1

and A_2 one-dimensional irreps (1d-irreps), both invariant under C_{3z} and eigenstates of C_{2x} with opposite eigenvalues $c_{2x} = \pm 1$. In addition, we consider one two-dimensional irrep (2d-irrep) E, which transforms under C_{3z} and C_{2x} as the 2d-irreps in Table 3.1, hence comprises eigenstates of C_{2x}, with opposite eigenvalues $c_{2x} = \pm 1$, which are not invariant under C_{3z}.
We define on sublattice $\alpha = AB, BA$ the spin-σ WO annihilation operators $\Psi_{\alpha,\mathbf{R}\sigma}$ and $\Phi_{\alpha,\mathbf{R}\sigma}$ corresponding to the two 1d-irreps (Ψ) or the single 2d-irrep (Φ), respectively

$$\Psi_{\alpha,\mathbf{R}\sigma} = \begin{pmatrix} \Psi_{\alpha,1,s,\mathbf{R}\sigma} \\ \Psi_{\alpha,2,s,\mathbf{R}\sigma} \\ \Psi_{\alpha,1,p,\mathbf{R}\sigma} \\ \Psi_{\alpha,2,p,\mathbf{R}\sigma} \end{pmatrix}, \Phi_{\alpha,\mathbf{R}\sigma} = \begin{pmatrix} \Phi_{\alpha,1,s,\mathbf{R}\sigma} \\ \Phi_{\alpha,2,s,\mathbf{R}\sigma} \\ \Phi_{\alpha,1,p,\mathbf{R}\sigma} \\ \Phi_{\alpha,2,p,\mathbf{R}\sigma} \end{pmatrix}, \tag{3.16}$$

where the subscript s refers to $c_{2x} = +1$, and p to $c_{2x} = -1$, while the labels 1 and 2 refer to the two valleys. It is implicit that each component is itself a spinor that includes fermionic operators corresponding to different WOs that transform like the same irrep. We shall combine the operators of different sublattices into a single spinor

$$\Psi_{\mathbf{R}\sigma} = \begin{pmatrix} \Psi_{AB,\mathbf{R}\sigma} \\ \Psi_{BA,\mathbf{R}\sigma} \end{pmatrix}, \Phi_{\mathbf{R}\sigma} = \begin{pmatrix} \Phi_{AB,\mathbf{R}\sigma} \\ \Phi_{BA,\mathbf{R}\sigma} \end{pmatrix}. \tag{3.17}$$

We further introduce three different Pauli matrices σ_a that act in the moiré sublattice space (AB, BA), μ_a in the $c_{2x} = \pm 1$ space (s, p), and τ_a in the valley space (1, 2), where $a = 0, 1, 2, 3$, $a = 0$ denoting the identity.
With these definitions, the generator (3.1) of the valley $U_v(1)$ symmetry becomes simply

$$\Delta N_v = \sum_{\mathbf{R}\sigma} \left(\Psi^\dagger_{\mathbf{R}\sigma}\, \sigma_0\, \tau_3\, \mu_0\, \Psi_{\mathbf{R}\sigma} + \Phi^\dagger_{\mathbf{R}\sigma}\, \sigma_0\, \tau_3\, \mu_0\, \Phi_{\mathbf{R}\sigma} \right). \tag{3.18}$$

It is now worth deriving the expression of the space group symmetry operations in this notation and representation. By definition, the C_{2x} transformation corresponds to the simple operator

$$\begin{aligned} \mathscr{C}_{2x}\left(\Psi_{\mathbf{R}\sigma}\right) &= \sigma_0\, \tau_0\, \mu_3\, \Psi_{C_{2x}(\mathbf{R})\,\sigma}, \\ \mathscr{C}_{2x}\left(\Phi_{\mathbf{R}\sigma}\right) &= \sigma_0\, \tau_0\, \mu_3\, \Phi_{C_{2x}(\mathbf{R})\,\sigma}. \end{aligned} \tag{3.19}$$

The 180° rotation around the z-axis that connects sublattice AB with BA of each layer (C_{2z}) is not diagonal in the valley indices and can be represented by [75, 74]

$$\begin{aligned} \mathscr{C}_{2z}\left(\Psi_{\mathbf{R}\sigma}\right) &= \sigma_1\, \tau_1\, \mu_0\, \Psi_{C_{2z}(\mathbf{R})\,\sigma}, \\ \mathscr{C}_{2z}\left(\Phi_{\mathbf{R}\sigma}\right) &= \sigma_1\, \tau_1\, \mu_0\, \Phi_{C_{2z}(\mathbf{R})\,\sigma}. \end{aligned} \tag{3.20}$$

Finally, since $C_{2y} = C_{2z} \times C_{2x}$, then

$$\begin{aligned} \mathscr{C}_{2y}\left(\Psi_{\mathbf{R}\sigma}\right) &= \sigma_1\, \tau_1\, \mu_3\, \Psi_{C_{2y}(\mathbf{R})\,\sigma}, \\ \mathscr{C}_{2y}\left(\Phi_{\mathbf{R}\sigma}\right) &= \sigma_1\, \tau_1\, \mu_3\, \Phi_{C_{2y}(\mathbf{R})\,\sigma}. \end{aligned} \tag{3.21}$$

For the sake of simplicity we shall not require the model Hamiltonian to reproduce precisely the shape of all the bands around charge neutrality, especially those above or below the FBs, but only the correct elementary band representation, topology and, obviously, the existence of the four flat bands separated from the all others. Considering for instance only the 32 states at $\mathbf{\Gamma}$

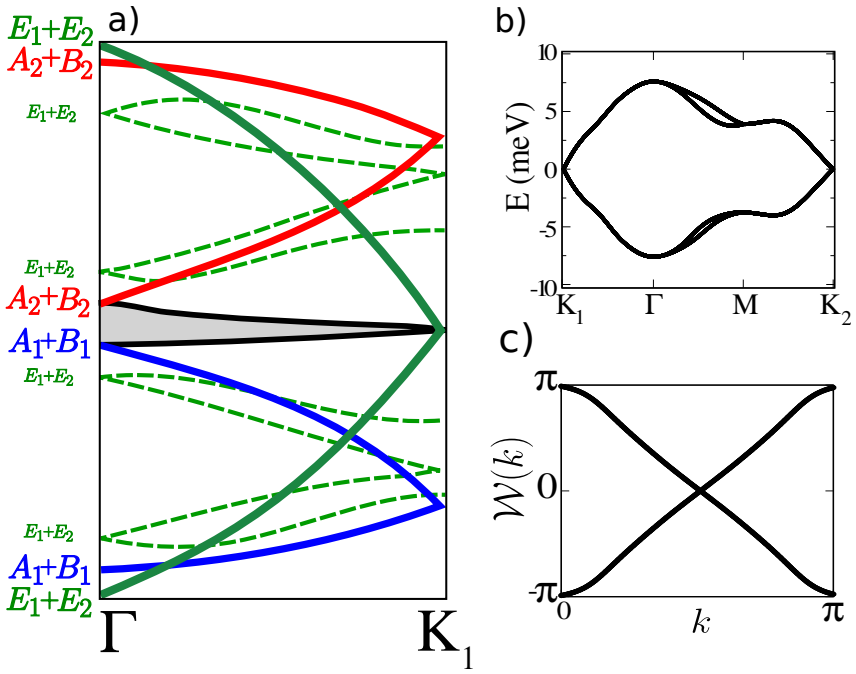

Figure 3.8: Panel a): sketch of the elementary band representation along $\mathbf{\Gamma} \to \mathbf{K}_1$ taking into account the 32 bands closest to the charge neutrality point and without allowing avoided crossing between same symmetry Bloch states. Blue, red and green lines refer to Bloch states that at $\mathbf{\Gamma}$ transform like $A_1 + B_1$, $A_2 + B_2$ and $E_1 + E_2$, respectively. Should we allow for avoided crossings, close to charge neutrality we would obtain the four flat bands shown as black lines surrounding the shaded region. Panel b): the FBs obtained by a model tight-binding Hamiltonian that includes only the solid bands of panel a). Panel c): Wilson loop corresponding to the four bands in panel b) fully occupied.

closest to the charge neutrality point, and maintaining our assumption of WOs centred at the Wyckoff positions $2c$, those states (apart from avoided crossings allowed by symmetry) would evolve from $\mathbf{\Gamma}$ to $\mathbf{K}_1$ in accordance with the D_6 space group as shown in Fig. 3.8. Once we allow same-symmetry Bloch states to repel each other along $\mathbf{\Gamma} \to \mathbf{K}_1$, the band representation can look similar to the real one (Fig. 3.3), including the existence of the four FBs that start at $\mathbf{\Gamma}$ as two doublets, $A_1 + B_1$ and $A_2 + B_2$, and end at $\mathbf{K}_1$ as two degenerate doublets, each transforming as the 2d-irrep E, see the two solid black lines in Fig. 3.8. While this picture looks compatible with the actual band structure, we shall take a further simplification and just consider the thicker red, blue and green bands in Fig. 3.8, which could still produce flat bands with the correct symmetries. This oversimplification obviously implies giving up the possibility to accurately reproduce the shape of the bands above and below the FBs - but it makes the algebra much simpler. Within this approximation the components of the spinor operators in Eq. (3.16) are actually single fermionic operators, so that we limit ourselves to just four WOs for each sublattice, AB or BA, and valley, 1 and 2. Two of such WOs transform like the 1d-irreps, one even, A_1, and the other odd, A_2, under C_{2x}. The other two instead transform like the 2d-irrep E. In order to make the invariance under C_{3z} more explicit, we shall use the transformed spinors

$$\begin{pmatrix} \Phi_{+1,\mathbf{k}\sigma} \\ \Phi_{-1,\mathbf{k}\sigma} \end{pmatrix} = \frac{1}{\sqrt{2}} \begin{pmatrix} 1 & -i \\ 1 & +i \end{pmatrix} \begin{pmatrix} \Phi_{s,\mathbf{k}\sigma} \\ \Phi_{p,\mathbf{k}\sigma} \end{pmatrix}, \tag{3.22}$$

for the 2d-irreps, which correspond to WOs eigenstates of C_{3z}. Moreover, it is convenient to transform also the spinors $\Psi_{\mathbf{k}\sigma}$ of the 1d-irreps in the same way, i.e.,

$$\begin{pmatrix} \Psi_{+1,\mathbf{k}\sigma} \\ \Psi_{-1,\mathbf{k}\sigma} \end{pmatrix} = \frac{1}{\sqrt{2}} \begin{pmatrix} 1 & -i \\ 1 & +i \end{pmatrix} \begin{pmatrix} \Psi_{s,\mathbf{k}\sigma} \\ \Psi_{p,\mathbf{k}\sigma} \end{pmatrix}, \tag{3.23}$$

which correspond to WOs still invariant under C_{3z} but not under C_{2x}, whose representation both in $\Psi_{\mathbf{k}\sigma}$ and $\Phi_{\mathbf{k}\sigma}$ becomes the Pauli matrix μ_1. In conclusion the spinor operators defined above satisfy

$$\begin{aligned} C_{3z}\Big(\Phi_{\mathbf{k}\sigma}\Big) &= \begin{pmatrix} \omega & 0 \\ 0 & \omega^* \end{pmatrix} \Phi_{C_{3z}(\mathbf{k})\,\sigma}\,, \\ C_{3z}\Big(\Psi_{\mathbf{k}\sigma}\Big) &= \Psi_{C_{3z}(\mathbf{k})\,\sigma}\,, \\ C_{2x}\Big(\Phi_{\mathbf{k}\sigma}\Big) &= \mu_1\,\Phi_{C_{3z}(\mathbf{k})\,\sigma}\,, \\ C_{2x}\Big(\Psi_{\mathbf{k}\sigma}\Big) &= \mu_1\,\Psi_{C_{3z}(\mathbf{k})\,\sigma}\,. \end{aligned} \tag{3.24}$$

We shall, for simplicity, consider only nearest and next nearest neighbor hopping between AB and BA region, which correspond to the following functions in momentum space:

$$\begin{aligned} \gamma_1(\mathbf{k}) &= \alpha_{\mathbf{k}}\Big(1 + \mathrm{e}^{-i\mathbf{k}\cdot\mathbf{a}} + \mathrm{e}^{-i\mathbf{k}\cdot\mathbf{b}}\Big), \\ \gamma_{1,+1}(\mathbf{k}) &= \alpha_{\mathbf{k}}\Big(1 + \omega\,\mathrm{e}^{-i\mathbf{k}\cdot\mathbf{a}} + \omega^*\,\mathrm{e}^{-i\mathbf{k}\cdot\mathbf{b}}\Big), \\ \gamma_{1,-1}(\mathbf{k}) &= \alpha_{\mathbf{k}}\Big(1 + \omega^*\,\mathrm{e}^{-i\mathbf{k}\cdot\mathbf{a}} + \omega\,\mathrm{e}^{-i\mathbf{k}\cdot\mathbf{b}}\Big), \end{aligned} \tag{3.25}$$

for first neighbors, and

$$\begin{aligned} \gamma_2(\mathbf{k}) &= \alpha_{\mathbf{k}}\Big(\mathrm{e}^{i\mathbf{k}\cdot(\mathbf{a}-\mathbf{b})} + \mathrm{e}^{-i\mathbf{k}\cdot(\mathbf{a}-\mathbf{b})} + \mathrm{e}^{-i\mathbf{k}\cdot(\mathbf{a}+\mathbf{b})}\Big), \\ \gamma_{2,+1}(\mathbf{k}) &= \alpha_{\mathbf{k}}\Big(\omega\,\mathrm{e}^{i\mathbf{k}\cdot(\mathbf{a}-\mathbf{b})} + \omega^*\mathrm{e}^{-i\mathbf{k}\cdot(\mathbf{a}-\mathbf{b})} + \mathrm{e}^{-i\mathbf{k}\cdot(\mathbf{a}+\mathbf{b})}\Big), \\ \gamma_{2,-1}(\mathbf{k}) &= \alpha_{\mathbf{k}}\Big(\omega^*\mathrm{e}^{i\mathbf{k}\cdot(\mathbf{a}-\mathbf{b})} + \omega\,\mathrm{e}^{-i\mathbf{k}\cdot(\mathbf{a}-\mathbf{b})} + \mathrm{e}^{-i\mathbf{k}\cdot(\mathbf{a}+\mathbf{b})}\Big), \end{aligned} \tag{3.26}$$

for second neighbors, where $\omega = \mathrm{e}^{i2\pi/3}$, $\alpha_{\mathbf{k}} = \mathrm{e}^{i\mathbf{k}\cdot(\mathbf{a}+\mathbf{b})/3}$, and the superlattice constants $\mathbf{a} = R(\sqrt{3}/2, -1/2)$ and $\mathbf{b} = R(\sqrt{3}/2, 1/2)$. Since

$$\begin{aligned} C_{3z}(\mathbf{a}) &= \mathbf{b} - \mathbf{a}\,, C_{3z}(\mathbf{b}) = -\mathbf{a}\,, \\ C_{2x}(\mathbf{a}) &= \mathbf{b}\,, C_{2x}(\mathbf{b}) = \mathbf{a}\,, \end{aligned} \tag{3.27}$$

then, for $n = 1, 2$,

$$\begin{aligned} \gamma_n\Big(C_{3z}(\mathbf{k})\Big) &= \gamma_n(\mathbf{k})\,, \\ \gamma_{n,\pm1}\Big(C_{3z}(\mathbf{k})\Big) &= \omega^{\pm1}\,\gamma_{n,\pm1}(\mathbf{k})\,, \\ \gamma_n\Big(C_{2x}(\mathbf{k})\Big) &= \gamma_n(\mathbf{k})\,, \\ \gamma_{n,\pm1}\Big(C_{2x}(\mathbf{k})\Big) &= \gamma_{n,\mp1}(\mathbf{k})\,, \end{aligned} \tag{3.28}$$

which shows that $\gamma_{n,\pm1}(\mathbf{k})$ transform like the 2d-irrep E.
We assume the following tight-binding Hamiltonian for the 1d-irreps

$$H_{1d-1d} = \sum_{\mathbf{k}\sigma}\Big[-\Delta\,\Psi^\dagger_{\mathbf{k}\sigma}\,\sigma_0\,\mu_1\,\tau_0\,\Psi_{\mathbf{k}\sigma} - \sum_{n=1,2} t^{(n)}_{11}\Big(\gamma_n(\mathbf{k})\,\Psi^\dagger_{\mathbf{k}\sigma}\,\sigma^+\,\mu_0\,\tau_0\,\Psi_{\mathbf{k}\sigma} + H.c.\Big)\Big],$$

where $t_{11}^{(1)}$ and $t_{11}^{(2)}$ are the first and second neighbor hopping amplitudes, respectively, which we assume to be real.
The 2d-irreps have instead the Hamiltonian

$$H_{2d-2d} = -\sum_{\mathbf{k}\sigma}\sum_{n=1}^{2}\left[t_{22}^{(n)}\,\gamma_n(\mathbf{k})\,\Phi_{\mathbf{k}\sigma}^{\dagger}\,\sigma^{+}\,\mu_0\,\tau_0\,\Phi_{\mathbf{k}\sigma} + g_{22}^{(n)}\,\Phi_{\mathbf{k}\sigma}^{\dagger}\,\sigma^{+}\,\hat{\gamma}_n(\mathbf{k})\,\mu_1\,\tau_0\,\Phi_{\mathbf{k}\sigma} + H.c.\right],$$

with real hopping amplitudes, where

$$\hat{\gamma}_n(\mathbf{k}) = \begin{pmatrix}\gamma_{n,+1}(\mathbf{k}) & 0\\ 0 & \gamma_{n,-1}(\mathbf{k})\end{pmatrix}. \tag{3.29}$$

Finally, the coupling between 1d and 2d irreps is represented by the Hamiltonian

$$\begin{aligned}H_{1d-2d} = -\sum_{\mathbf{k}\sigma}\sum_{n=1}^{2} t_{12}^{(n)}\Big[&\Phi_{\mathbf{k}\sigma}^{\dagger}\,\sigma^{+}\,\mu_1\,\hat{\gamma}_n(\mathbf{k})\,\mu_1\,\tau_0\,\Psi_{\mathbf{k}\sigma} + \Psi_{\mathbf{k}\sigma}^{\dagger}\,\sigma^{+}\,\hat{\gamma}_n(\mathbf{k})\,\tau_0\,\Phi_{\mathbf{k}\sigma}\\ &+ i\,\Phi_{\mathbf{k}\sigma}^{\dagger}\,\sigma^{+}\,\mu_1\,\hat{\gamma}_n(\mathbf{k})\,\tau_3\,\Psi_{\mathbf{k}\sigma} + i\,\Psi_{\mathbf{k}\sigma}^{\dagger}\,\sigma^{+}\,\mu_1\,\hat{\gamma}_n(\mathbf{k})\,\tau_3\,\Phi_{\mathbf{k}\sigma} + H.c.\Big],\end{aligned}$$

with real $t_{12}^{(n)}$.
The Hamiltonian thus reads

$$T_{\rm el} = H_{1d-1d} + H_{2d-2d} + H_{1d-2d}\,, \tag{3.30}$$

which, through the equations (3.24) and (3.28), can be readily shown to be invariant under C_{3z} and C_{2x}, and is evidently also invariant under the $U_v(1)$ generator τ_3. In addition, the Hamiltonian must be also invariant under TC_{2z}, where T is the time reversal operator. Noting that

$$\begin{aligned}TC_{2z}\Big(\Phi_{\mathbf{k}\sigma}\Big) &= \sigma_1\,\mu_1\,\Phi_{\mathbf{k}-\sigma}\,,\\ TC_{2z}\Big(\Psi_{\mathbf{k}\sigma}\Big) &= \sigma_1\,\mu_1\,\Psi_{\mathbf{k}-\sigma}\,,\end{aligned} \tag{3.31}$$

one can show that H in (3.30) is also invariant under that symmetry. Finally the minimal tight-binding model Hamiltonian can be written in the more compact form:

$$H_{\rm el} = -\Delta\sum_{\mathbf{R}\sigma}\Psi_{\mathbf{R}\sigma}^{\dagger}\sigma_0\tau_0\mu_3\Psi_{\mathbf{R}\sigma} + T_{\rm el}, \tag{3.32}$$

where Δ splits the s from the p WOs of the 1d-irreps. The model Hamiltonian thus depends on eight parameters. The FBs shown in Fig. 3.8 have been obtained choosing: $\Delta = 10$, $t_{11}^{1} = 2$, $t_{22}^{1} = 5$, $g_{22}^{1} = 10$, $t_{22}^{2} = g_{22}^{2} = -t_{11}^{2} = 1.2$, $t_{12}^{1} = 2$ and $t_{12}^{2} = 0.5$. We emphasize that the FBs arise in this picture from a sequence of avoided crossings between a large set of relatively broad bands that strongly repel each other away from the high symmetry points, rather than from truly localized' WOs.

4

Valley Jahn-Teller Effect in twisted bilayer graphene

In this chapter we introduce a phonon-driven mechanism able to open insulating gaps and mediate superconductivity in the flat bands of magic angle twisted bilayer graphene. Owing to the flatness of these bands, the fractional filling insulators found in [8, 9] are *conjectured* to be Mott Insulators, even though rather anomalous ones, since they turn frankly metallic above a critical temperature or above a threshold Zeeman splitting in a magnetic field (see Section. 1), features not expected from a Mott insulator. Actually, the linear size of the unit cell at the magic angle is as large as ≈ 14 nm, and the effective *on-site* Coulomb repulsion, the so-called Hubbard U, must be given by the charging energy in this large supercell projected onto the FBs, including screening effects due to the gates and to the other bands. Even neglecting the latter, the estimated $U \sim 9$ meV is comparable to the bandwidth of the FBs [82]. Since the FBs are reproducibly found in experiments [14, 8, 9, 15, 16, 17, 23, 62, 63] to be separated from the other bands by a gap of around $\sim 30 - 50$ meV, the actual value of U should be significantly smaller, implying that tBLG might not be more correlated than a single graphene sheet [83]. In turn, this suggests that the insulating behaviour at $\nu = \pm 2$ occupancy might instead be the result of a weak-coupling Stoner or CDW band instability driven by electron-electron and/or electron-phonon interactions, rather than a Mott localization phenomenon.
As pointed out in [77], in order to open an insulating gap the band instability must break the twofold degeneracy at the **K**-points imposed by the D_6 space group symmetry of the moiré superlattice, as well as the additional twofold degeneracy due to the valley charge conservation. In other words, breaking only symmetries of the D_6 group is not enough to open the fractional filling gaps observed in experiments. It is therefore essential to identify a microscopic mechanism that could efficiently break the valley symmetry $U_v(1)$. The most natural candidate is the Coulomb repulsion [77, 84, 85], whose Fourier transform decays more slowly than that of electron hopping, possibly introducing a non negligible coupling among the two valleys even at small twist angles. Indeed DFT-based calculations show a tiny valley splitting [75, 53], almost at the limits of accuracy of the method, which is nevertheless too small to explain the insulating states found in the FBs.
Here we uncover another $U_v(1)$-breaking mechanism involving instead the lattice degrees of

freedom, mostly ignored so far. As mentioned in the first Chapter 2.2, even ab-initio DFT-based calculations fail to predict well defined FBs separated from other bands unless atomic positions are allowed to relax. That alone already demonstrated that the effects of atomic motions in the lattice are not at all negligible in tBLG, further supported by the significant phonon contribution to transport [23, 25, 86]. We calculate the phonon spectrum of the fully-relaxed bilayer at 1.08° twist angle, which shows the presence, among the about thirty thousands phonons, of a small set of very special optical modes, with C-C stretching character, very narrow and uniquely coherent over the moiré supercell Brillouin Zone. Among them, we find a doubly degenerate optical mode that couples to the $U_v(1)$ symmetry much more efficiently than Coulomb repulsion seems to do in DFT calculations. A subsequent frozen-phonon tight-binding calculation shows that this mode is able to fully lift the valley degeneracy even when its lattice deformation amplitude is extremely small. Remarkably, both electrons and phonons are twofold $U_v(1)$ -degenerate, and the coupling of this mode with the electron bands actually realizes an E ⊗ e Jahn-Teller (JT) effect [87]. This effect is able to stabilize insulating states at integer occupancies of the FBs, both even and odd. Moreover, a surprising and important additional result will be that the electron-phonon coupling magnitude controlling this process is extremely large, and not small as one could generally expect for a very narrow band. We therefore studied the superconducting state that might be mediated by the Jahn-Teller coupling.
This Chapter is organized as follows. In subsection 4.0.1 we explain how the valley symmetry enforces two fold degeneracies along most of the high-symmetry lines in the bandstructure of the system. The phonon spectrum and its properties, especially focusing on special optical modes strongly coupled with the valley $U_v(1)$ symmetry, are throughly discussed in section 4.1. Section 4.2 addresses the properties of the superconducting state that might be stabilized by the particular phonon mode identified in the previous section through a mean-field BCS calculation. Finally, in 4.3 we work out the electron-phonon coupling Hamiltonian terms in the continuum model formalism.

4.0.1 SU(2) symmetry and accidental degeneracy along C_{2y} invariant lines

As shown in Fig. 3.3, along all directions that are invariant under C_{2y}, which include the diagonals as well as all the edges of the MBZ, the electronic bands show a twofold degeneracy between Bloch states that transform differently under C_{2y}. These lines corresponds to the domain walls (DWs) in real space. This "accidental" degeneracy is a consequence of the interplay between $U_v(1)$ and C_{2y} symmetries. We can use the operators and Wannier orbitals introduced in Section. 3.3.1 and focus along the $\Gamma \to K_{1,2}$ and $M \to K_{1,2}$ high symmetry lines where:

$$\mathscr{C}_{2y}\left(\Psi_{\mathbf{k}\sigma}\right) = \sigma_1\,\tau_1\,\mu_3\,\Psi_{\mathbf{k}\sigma}\,, \tag{4.1}$$

and similarly for $\Phi_{\mathbf{k}\sigma}$. It follows that the generator of $U_v(1)$, i.e., the operator $\sigma_0\,\tau_3\,\mu_0$, anticommutes with the expression of C_{2y} along the lines invariant under that same symmetry, namely the operator $\sigma_1\,\tau_1\,\mu_3$, and both commute with the Hamiltonian. Then also their product, $\sigma_1\,\tau_2\,\mu_3$, commutes with the Hamiltonian and anticommutes with the other two. The three operators

$$2T_3 = \sigma_0\,\tau_3\,\mu_0, \quad 2T_1 = \sigma_1\,\tau_1\,\mu_3, \quad 2T_2 = \sigma_1\,\tau_2\,\mu_3, \tag{4.2}$$

thus realise an $SU(2)$ algebra and all commute with the Hamiltonian $\hat{H}_{\mathbf{k}}$ in momentum space for any C_{2y}-invariant $\mathbf{k}$-point. This emergent $SU(2)$ symmetry is therefore responsible of the degeneracy of eigenstates with opposite parity under C_{2y}. We note that C_{2x} instead commutes

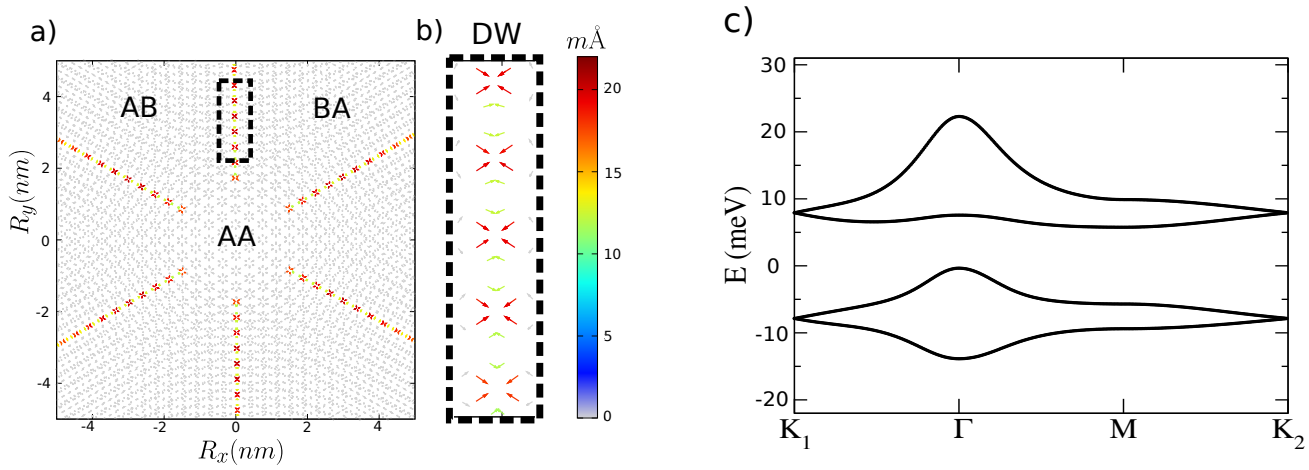

Figure 4.1: Panel a): the displacement field $\boldsymbol{\eta}(\mathbf{r})$, Eq. (4.3), restricted on the DWs: the direction of the atomic displacement is depicted by a small arrow, while its magnitude in mÅ is expressed in colors. Panel b): displacement along the DW area highlighted by a black dashed line in panel a). The overall effect of the distortion is a narrowing of the DW. Panel c): low energy band structure of tBLG at $\theta = 1.08$ after the distortion in panel a). The two-fold degeneracies protected by the valley symmetry are completely lifted.

with $U_v(1)$, so that there is no $SU(2)$ symmetry protection against valley splitting along C_{2x} invariant lines ($\Gamma \to M$).

4.1 Phonons in twisted bilayer graphene

The $U_v(1)$ valley symmetry is an emergent one since, despite the fact that its generator (3.1) does not commute with the Hamiltonian, the spectrum around charge neutrality is nonetheless $U_v(1)$–invariant. It is therefore not obvious to envisage a mechanism that could efficiently break it.
However, since the lattice degrees of freedom play an important role at equilibrium, as discussed in Section 2.2, it is possible that they could offer the means to destroy the $U_v(1)$ valley symmetry. In this Section we shall show that they indeed provide such a symmetry-breaking tool.

4.1.1 Valley splitting lattice modulation

In Section 3.1.2 we mentioned that the valley symmetry arises because, even though inequivalent Dirac nodes of the two layers should be coupled to each other by the Hamiltonian after being folded onto the same point of the MBZ (see Fig. 2.1), at small angle these matrix elements are vanishingly small and thus the valleys are effectively decoupled. That is true if the carbon lattice, although mechanically relaxed, is unperturbed by the presence of the electrons. Once coupling with electrons is considered, we cannot exclude that for example a lattice distortion modulated with the wave vectors connecting the inequivalent Dirac nodes of the two layers, K_ϕ with $K'_{-\phi}$ and K'_ϕ with $K_{-\phi}$ in Fig. 4.2, might instead yield a significant matrix element among the valleys. To investigate that possibility we build an ad-hoc distortion into the bilayer carbon atom positions. We define the vector $\mathbf{Q}_{ij} = \mathbf{K}_{\phi,i} - \mathbf{K}'_{-\phi,j}$, where $i, j = 1, 2, 3$ run over the three equivalent Dirac points of the BZ of each layer, and the D_6 conserving displacement field

$$\boldsymbol{\eta}(\mathbf{r}) = \sum_a \sum_{i,j=1}^{3} \sin\left(\mathbf{Q}_{ij} \cdot \mathbf{r}_a\right) \mathbf{u}_{a,ij}\, \delta(\mathbf{r} - \mathbf{r}_a)\,, \tag{4.3}$$

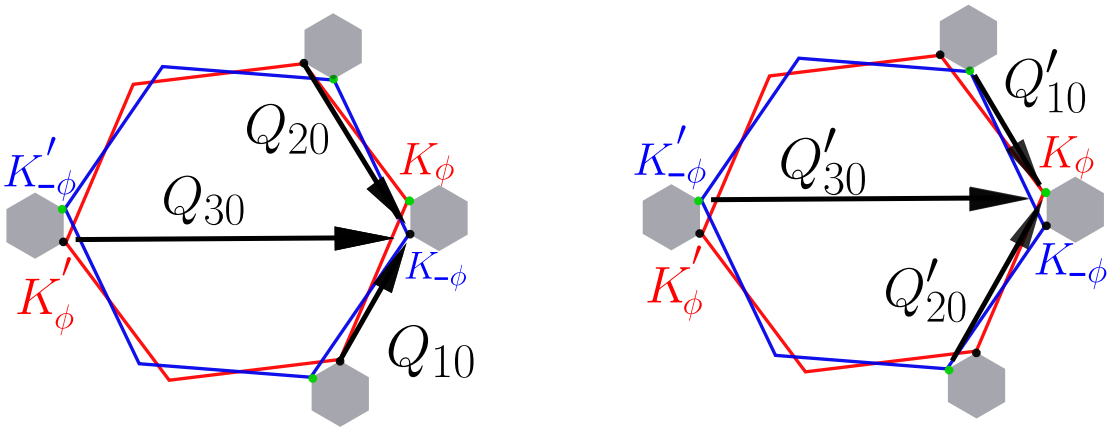

Figure 4.2: Q-vectors which connect inequivalent valleys in different layers used in Eq. 4.3.

where a runs over all atomic positions, and $\mathbf{u}_{a,ij}$ corresponds to a displacement of atom a in direction $\mathbf{Q}_{ij}$, whose (tunable) magnitude is the same for all atoms. In proximity of the AA regions the distortion is locally similar to the graphene breathing mode, the in-plane transverse optical phonon at $\mathbf{K}$ [88] with A_1 symmetry. Since by construction $\mathbf{Q}_{ij}$ is a multiple integer of the reciprocal lattice vectors, $\boldsymbol{\eta}(\mathbf{r})$ has the same periodicity of the unit cell, i.e., the distortion is actually at the $\mathbf{\Gamma}$ point. Moreover, the distortion's D_6 invariance implies no change of space group symmetries.

Since the most direct evidence of the $U_v(1)$ symmetry is the accidental degeneracy in the band structure along all C_{2y}–invariant lines, corresponding just to the DWs directions in real space, we further assume the action of the displacement field $\boldsymbol{\eta}(\mathbf{r})$ to be restricted to a small region in proximity of the DWs, affecting only $\approx 1\%$ of the atoms in the moiré supercell, see top panels in Fig. 4.1. The modified FBs in presence of the displacement field $\boldsymbol{\eta}(\mathbf{r})$ with $\left|\mathbf{u}_{a,ij}\right| = 20$ mÅ are shown in the bottom panel of Fig. 4.1. Remarkably, despite the minute distortion magnitude and the distortion involving only the minority of carbon atoms in the DWs, the degeneracy along $\mathbf{\Gamma} \to \mathbf{K}_1$ and $\mathbf{M} \to \mathbf{K}_2$ is lifted to such an extent that the four bands split into two similar copies. This is remarkable in two aspects. First, we repeat, because there is no space symmetry breaking. The only symmetry affected by the distortion is $U_v(1)$, since, by construction, $\boldsymbol{\eta}(\mathbf{r})$ preserve the full space group symmetries. Second, the large splitting magnitude reflects an enormous strength of the effective electron-phonon coupling, whose origin is interesting. Generally speaking, in fact, broad bands involve large hoppings and large absolute electron-phonon couplings, while the opposite is expected for narrow bands. The large electron-phonon couplings which we find for the low energy bands of tBLG is reminiscent of the broad-band origin of the FBs discussed in Sec. 3.2.3.

4.1.2 The phonon spectrum

We compute phonons in tBLG using the force constants of the non-harmonic potentials that we used to relax the structure:

$$C_{\alpha\beta}(il, js) = \frac{\partial^2 U}{\partial R_{\alpha il} \partial R_{\beta js}} \tag{4.4}$$

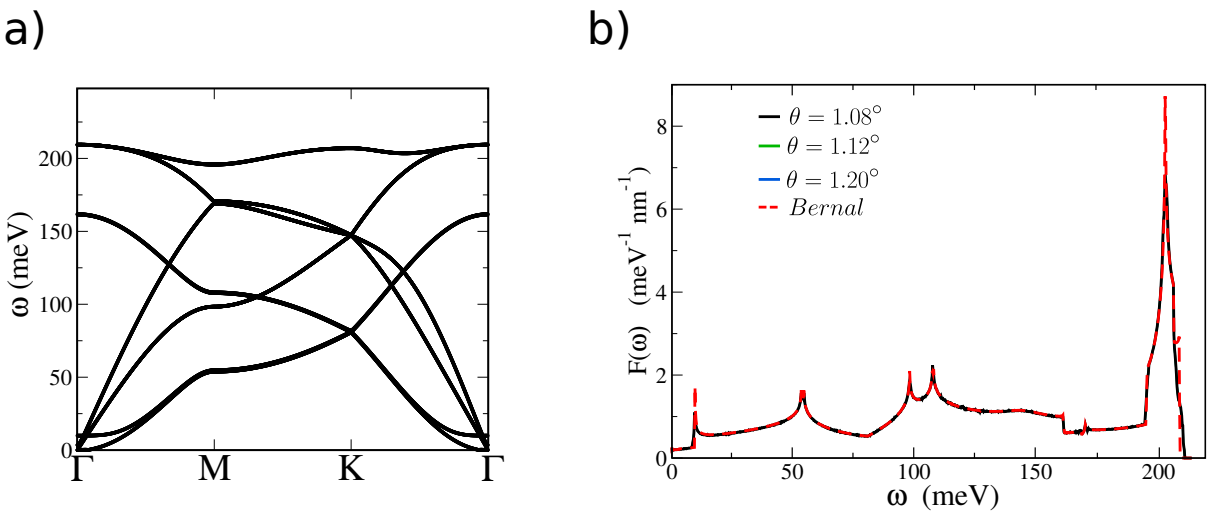

Figure 4.3: a): Phonon dispersion obtained with our choice of intralayer and interlayer potentials in Bernal stacked bilayer graphene. b) Phonon density of states $F(\omega)$ for Bernal stacked bilayer graphene at zero twist angle (red dashed line) and fully relaxed tBLG at $\theta = 1.20°, 1.12°, 1.08°$ (blue, green and black lines).

where (i, j) label the atoms in the unit cell, (l, s) the moiré lattice vectors and $\alpha, \beta = x, y, z$. Then, we define the Dynamical Matrix at phonon momentum $\mathbf{q}$ as:

$$D_{\alpha\beta ij}(\mathbf{q}) = \frac{1}{M_C} \sum_l C_{\alpha\beta}(il, j0) e^{-i\mathbf{q}R_l} \tag{4.5}$$

where M_C is the carbon atom mass. Using the above relation we determine the eigenvalue equation for the normal modes of the system and the phonon spectrum:

$$\sum_{j\beta} D_{\alpha\beta ij}(\mathbf{q}) \epsilon_{j\beta}(\mathbf{q}) = \omega^2_{\mathbf{q}} \epsilon_{i\alpha}(\mathbf{q}) \tag{4.6}$$

where $\omega_{\mathbf{q}}$ denote the energy of the normal mode $\epsilon(\mathbf{q})$. The phonon dispersion of Bernal stacked bilayer graphene obtained with this method is shown Fig. 4.3 a). As can be seen, the transverse optical (TO) modes at K are found at $\omega \approx 207$ meV. As a consequence, the Jahn-Teller modes discussed in the main text, which vibrate in the same way on the graphene scale, have similar frequency. However, the frequency of the TO modes in graphene is strongly sensitive to the choice of the intralayer potential used [89], so that these modes can be predicted to have frequencies as low as ≈ 170 meV [90, 91]. This implies that also the JT modes may be observed at a lower frequencies than ours. Fig. 4.3 shows the phonon density of states $F(\omega)$ for tBLG at three different twist angles in comparison with the Bernal bilayer. As previously reported [92, 93], $F(\omega)$ is almost independent of the twist angle, which only affects the inter-layer van der Waals forces, much weaker than the in-plane ones arising from the stiff $C - C$ bonds. As a consequence, phonons in tBLG are basically those of the Bernal stacked bilayer. This is true except for a small set of special phonon modes, clearly distinguishable in Fig. 4.4 that depicts the phonon spectrum zoomed in a very narrow energy region ≈ 0.04 *meV* around the high frequency graphene **K**-point peak of the phonon density of states. Specifically, within the large number of energy levels of all other highly dispersive phonon bands, unresolved in the narrow energy window, a set of 10 almost dispersionless modes emerges. We note that these special modes show the same accidental degeneracy doubling along the C_{2y} invariant lines as that of the electronic bands around the charge neutrality point.

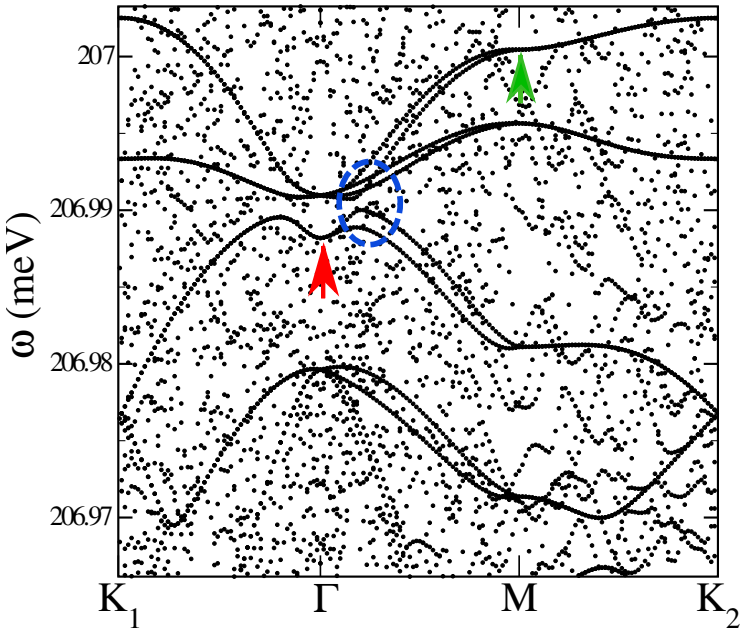

Figure 4.4: Zoom in the optical region of the phonon spectrum of the fully relaxed tBLG at $\theta = 1.08$. Among many scattered energy levels of highly dispersive branches (not resolved in this narrow energy window) a set of 10 narrow continuous branches stands out (no line drawn through data points, which just fall next to one another). The degeneracy of these modes is twice that expected by D_6 space symmetry, similar in this to electronic bands. The two-fold degenerate mode with the highest overlap with the deformation $\boldsymbol{\eta}(\mathbf{r})$, drawn in Fig. 4.5, is marked by a red arrow, while the mode at **M** used in section 4.1.5 by a green arrow. The avoided crossing which occurs close to **Γ** is encircled by a blue dashed line.

Similar to the electronic degeneracy, whose underlying $U_v(1)$ symmetry arises from vanishingly weak hopping matrix elements between interlayer **K**-**K**' points in the Hamiltonian, the mechanically weak van der Waals interlayer coupling here leads to an effective $U_v(1)$ symmetry for this group of lattice vibrations. Their poor dispersion is connected with a displacement which is non-uniform in the supercell, and is strongly modulated on the moiré length scale, a distinctive feature of these special modes that we shall denote as 'moiré phonons'. Their existence has been recently confirmed in experiments [94]. In particular, the vibration is maximum in the center of the AA zones, finite in the DWs, and negligible in the large AB and BA Bernal regions. The overlap between the displacement $\boldsymbol{\eta}(\mathbf{r})$ in (4.3) and the 33492 phonons of the $\theta = 1.08°$ tBLG at the **Γ** point is non-negligible only for those moiré phonons. In particular, we find the highest overlap with the doubly degenerate mode marked by a red arrow in Fig. 4.4, and which transforms like $A_1 + B_1$. In Fig. 4.5a) we show the real space distortion corresponding to the A_1 component of the doublet, where the displacement direction is represented by small arrows, while its intensity is encoded in colors. This inspection of the eigenvectors of these modes at the atomistic level reveals a definite underlying single-layer graphene character, specifically that of the A_1 symmetry transverse optical mode at **K**. Since the graphene **K**-point does *not* fold into the bilayer Γ-point, their appearance along the whole **Γ** → **K** line in the spectrum of the fully relaxed bilayer must be merely a consequence of relaxation, a relaxation that is particularly strong precisely in the AA and DW regions.

4.1.3 Insulating state at charge neutrality

We will next focus on the effect on the electronic band structure of a carbon atom displacement corresponding to the two degenerate phonon modes A_1 and B_1 at **Γ**, which should affect the valley

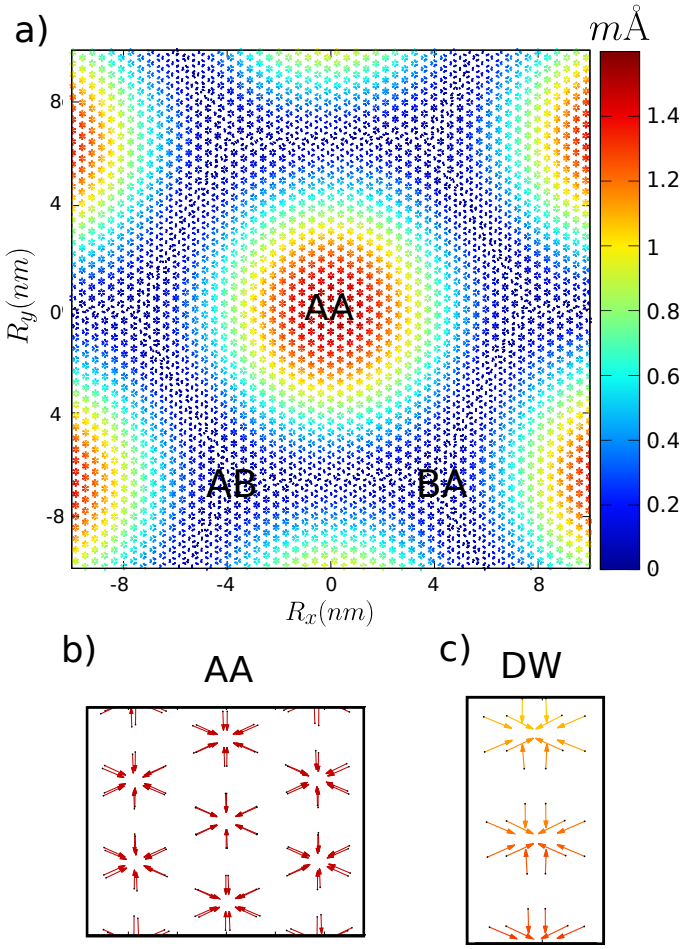

Figure 4.5: Panel a): atomic displacements on one of the two layers corresponding to the A_1-symmetry moiré mode of the phonon doublet marked by a red arrow in Fig. 4.4. The direction of displacement is represented by a small arrow centered at each atomic position, while its modulus is encoded in colors. The mean displacement per atom is 0.57 mÅ. Panel b): zoom in the center of an AA region, shown for both layers. Panel c): zoom along one of the domain walls. Note the similarity with the ad-hoc displacement in Fig. 4.1.

symmetry as the displacement in Fig. 4.1. In order to verify that, we carried out a frozen phonon calculation of the modified FB electronic structure with increasing intensity of the deformation. Remarkably, despite transforming as different irreps (A_1 or B_1), both frozen phonon distortions are not only degenerate, but have exactly the same effect on the bands. As soon as the lattice is distorted, see Fig. 4.6 b), the fourfold degeneracy at $\mathbf{K}_1$ and $\mathbf{K}_2$, and the twofold one at Γ and $\mathbf{M}$ is lifted, and small avoided crossings appear and start to move from $\mathbf{K}_{1(2)}$ towards the $\mathbf{M}$ points. Once they cross $\mathbf{M}$, they keep moving along $\mathbf{M} \rightarrow \mathbf{\Gamma}$, see Fig. 4.6 c). However, along these directions, the C_{2x} symmetry prevents the avoided crossings, and thus leads to six elliptical Dirac cones. Finally, once they reach $\mathbf{\Gamma}$ at a threshold value of the distortion, the six Dirac points annihilate so that a gap opens at the charge neutrality point (CNP), see Fig. 4.6 d). This gap-opening mechanism is very efficient, with large splittings even for small values of the atomic displacement amplitude shown in Fig. 4.6. For instance, an average displacement as small as ≈ 0.5 mÅ per atom is enough to completely separate the four FBs and to open a gap at charge neutrality.

We emphasize that this occurs without breaking any spatial symmetry of the tBLG, just $U_v(1)$. As a consequence, the insulator state possesses a non trivial topology, as highlighted by the

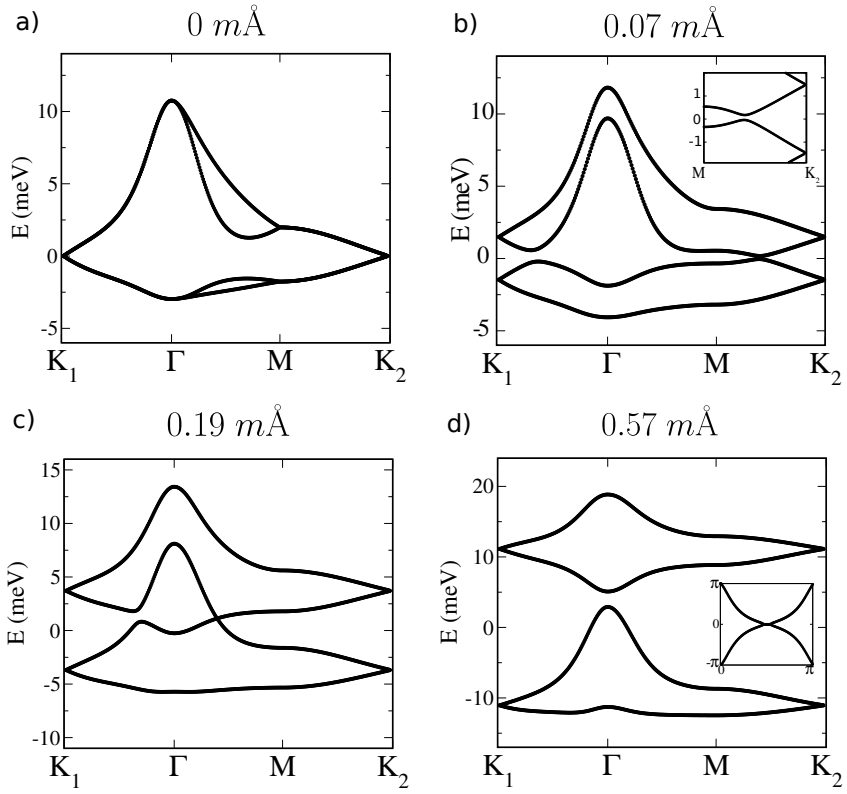

Figure 4.6: Evolution of the FBs when the lattice is distorted with increasing intensity along one of the two modes indicated by a red arrow in Fig. 4.4. Panel (a) undistorted. Panel (b) mean displacement per atom 0.07 mÅ. In the inset we show the avoided crossing along $\mathbf{M} \to \mathbf{K}_2$. Panel (c) mean displacement 0.19 mÅ. Now the avoided crossing appears as a genuine crossing protected by C_{2x} symmetry along $\mathbf{\Gamma} \to \mathbf{M}$, which actually leads to Dirac points. Panel (d) mean displacement 0.57 mÅ, opening a gap between the FBs. Inset: Wilson loop of the lowest two bands in panel d).

odd-winding of the Wilson loop of the lowest two bands, shown in the inset of the same figure 4.6 d). In turn, the non trivial topology of the system implies the existence of edge states within the gap separating the two lower flat bands from the two upper ones. We thus recalculated the band structure freezing the moiré phonon with A_1 symmetry at $\mathbf{\Gamma}$ in a ribbon geometry, which is obtained by cutting the tBLG along two parallel domain walls in the y-direction at a distance of 7 supercells. The ribbon has therefore translational symmetry along y, but it is confined in the x-direction. In Fig. 4.7 we show the single-particle energy levels as function of the momentum k_y along the y-direction. Edge states within the gap at charge neutrality are clearly visible. In particular, we find for each edge two counter-propagating modes.

As a matter of fact, recent experiments do report the existence of a finite gap also at charge neutrality [14, 20, 18, 27, 22], which is actually bigger than at other non zero integer fillings, and appears without a manifest breakdown of time reversal symmetry T [14] or C_{2z} symmetry [20], and with the FBs still well separated from other bands [20]. These evidences seem not to support an interaction driven gap, which would entail either T or T C_{2z} symmetry breakings [14, 95], or else the FBs touching other bands at the $\mathbf{\Gamma}$ point [14]. Our phonon-driven insulator at charge neutrality breaks instead $U_v(1)$ and, eventually, C_{2y} if the frozen phonon has B_1 character, both symmetries experimentally elusive. However, the edge states that we predict could be detectable by STM or STS, thus providing support or disproving the mechanism that we uncovered.
We end mentioning that near charge neutrality there are compelling evidences of a substantial breakdown of C_{3z} symmetry [16, 17, 20], which, although is not expected to stabilize on its own

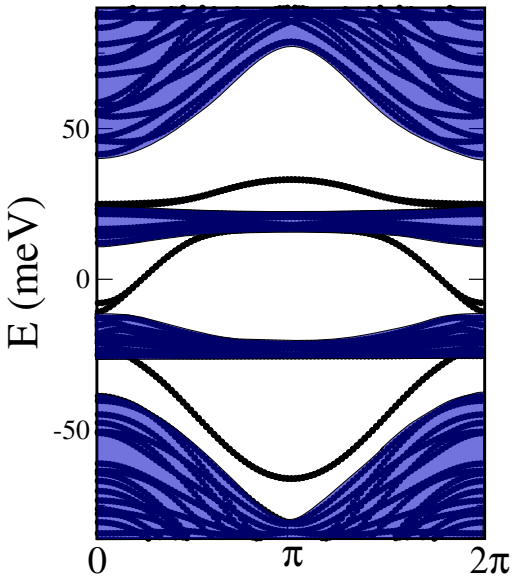

Figure 4.7: The band structure of twisted bilayer graphene at $\theta \approx 1.08°$ in a ribbon geometry with open boundary conditions. The atomic structure inside the unit cell (replicated 7 times along the x direction) has been deformed with the A_1 symmetric moiré phonon mode. With a mean deformation amplitude of $\approx$ 1.14 mÅ, that mode is so strongly coupled to open a large electronic gap at CNP of $\approx$ 25 meV. The bulk bands have been highlighted in blue to emphasize the presence of edge states both within the phonon-driven FBs gap and the gaps above and below them.

an insulating gap unless the latter were in fact just a pseudo gap [95], still it is worth being properly discussed, which we postpone to Section 4.1.6.

4.1.4 E ⊗ e Jahn-Teller effect

The evidence that the two degenerate modes marked by a red arrow in Fig. 4.4 produce the same band structure in a frozen-phonon distortion is reminiscent of a E ⊗ e Jahn-Teller effect, i.e., the coupling of a doubly degenerate vibration with a doubly degenerate electronic state [87].
Let us consider the action of the two Γ-point A_1 and B_1 phonon modes, hereafter denoted as q_1 and q_2, along the C_{2y} invariant lines. We note that the A_1 mode, q_1, although invariant under the D_6 group elements, is able to split the degeneracy along those lines. Therefore it must be coupled to the electrons through a D_6 invariant operator that does not commute with the $U_v(1)$ generator τ_3. That in turn cannot but coincide with C_{2y} itself, which, along the invariant lines, is the operator $T_1 = \sigma_1 \tau_1 \mu_3/2$ in Eq. (4.2). On the other hand, the B_1 mode, q_2, is odd under C_{2y}, and thus it must be associated with an operator that anticommutes with C_{2y} and does not commute with τ_3. The only possibility that still admits a $U(1)$ valley symmetry is the operator $T_2 = \sigma_1 \tau_2 \mu_3/2$ in Eq. (4.2). Indeed, with such a choice, the electron-phonon Hamiltonian is

$$H_{\text{el-ph}} = -g \left(q_1 T_1 + q_2 T_2 \right), \tag{4.7}$$

with g the coupling constant. This commutes with the operator

$$J_3 = T_3 + L_3 = \frac{\tau_3}{2} + \mathbf{q} \wedge \mathbf{p}\,, \tag{4.8}$$

(where $\mathbf{p} = (p_1, p_2)$ the conjugate variable of the displacement $\mathbf{q} = (q_1, q_2)$), the generator of a generalized $U_v(1)$ symmetry that involves electron and phonon variables. As anticipated, the

Hamiltonian (4.7) describes precisely a E ⊗ e Jahn-Teller problem [87, 96, 97].
Since the phonon mode **q** is almost dispersionless, see Fig. 4.4, we can think of it as the vibration of a moiré supercell, as if the latter were a single, though very large, molecule, and the tBLG a molecular conductor. In this language, the band structures shown in Fig. 4.6 would correspond to a static Jahn-Teller distortion. However, since the phonon frequency is substantially larger than the width of the flat bands, we cannot exclude the possibility of a dynamical Jahn-Teller effect that could mediate superconductivity [96, 98], or even stabilize a Jahn-Teller Mott insulator [97] in presence of a strong enough interaction.
The Jahn-Teller nature of the electron-phonon coupling entails a very efficient mechanism to split the accidental degeneracy, linear in the displacement within a frozen phonon calculation. However, this does not explain why an in-plane displacement as small as 0.57 mÅ is able to split the formerly degenerate states at **Γ** by an amount as large as 15 meV, see Fig. 4.6 d), of the same order as the original width of the flat bands. To clarify that, we note that this displacement would yield a change in the graphene nearest neighbor hopping of around $\delta t \simeq 3.6$ meV, see Eq. (2.15), which in turn entails a splitting at **Γ** of $6\,\delta t \sim 21$ meV, close to what we observe. We believe that such correspondence is not accidental, but indicates that the actual energy scale underneath the flat bands is on the order of the bare graphene bandwidth, rather than the flat bandwidth itself. We shall return on this issue later in Section 4.2.

4.1.5 Insulating states at other commensurate fillings

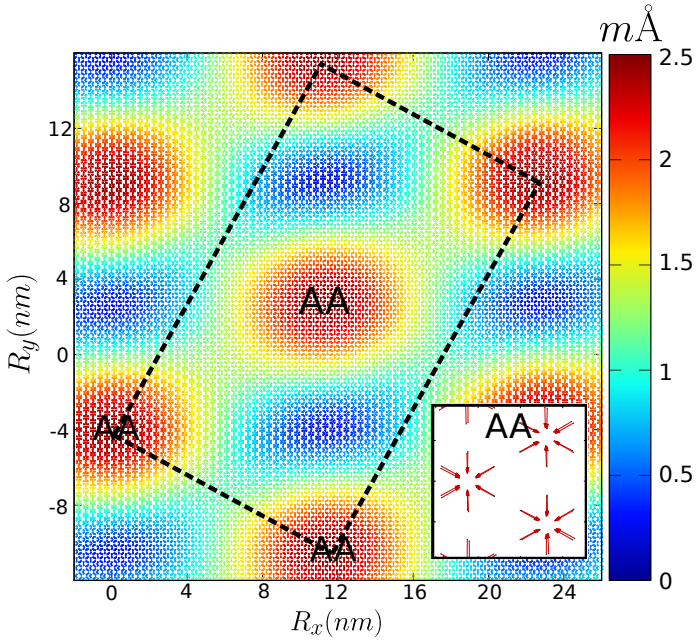

Figure 4.8: Atomic displacements on one of the two layers corresponding to one of the moiré modes at *M* marked by a green arrow in Fig. 4.4. The direction of displacement is represented by a small arrow centered at each atomic position, while its modulus is encoded in colors. The mean deformation is 1.8 mÅ and leads to the DOS in Fig. 4.9. The inset shows a zoom in the AA region close to the origin. The rectangular unit cell, now containing twice the number of atoms, is highlighted by a black dashed line.

The Γ-point distortion described above can lead to an insulating state at charge neutrality, possibly connected with the insulating state very recently reported [14, 20]. The same phonon branch might also stabilize insulating states at other integer occupancies of the mini bands besides charge neutrality. However, this necessarily requires freezing a mode at a high-symmetry

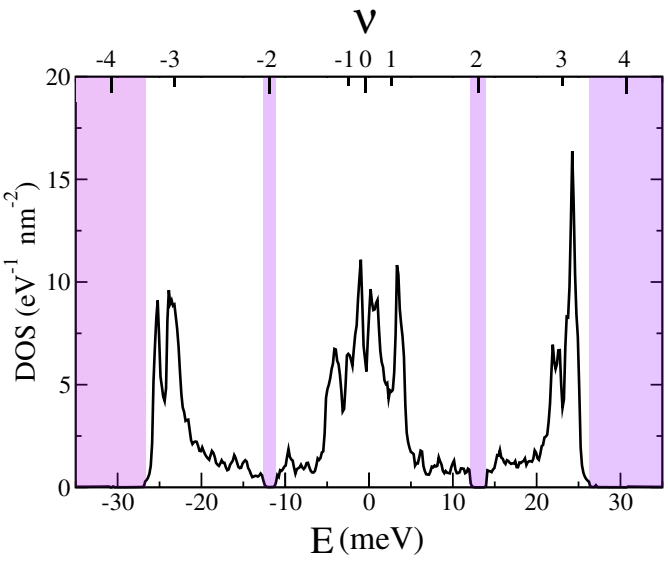

Figure 4.9: Density of states in the flat bands region after the tBLG has been distorted by one of the two degenerate modes at **M** marked by a green arrow in Fig. 4.4. A mesh of 40×40 points in the MBZ has been used. The DOS is expressed as function of energy, the zero corresponding to the CNP, and corresponding occupancy ν of the FBs. The band gaps at $\nu = \pm 2, \pm 4$ are highlighted in violet. The mean displacement per atom is 1.8 mÅ.

k-point different from **Γ** in order to get rid of the band touching at the Dirac points, $\mathbf{K}_1$ and $\mathbf{K}_2$, protected by the C_{6z} symmetry. We consider one of the two degenerate phonon modes at the **M**-point marked by a green arrow in Fig. 4.4. This mode has similar features as the Jahn-Teller one at **Γ**, even if it belongs to an upper branch due to an avoided crossing along $\mathbf{\Gamma} \rightarrow \mathbf{M}$ (blue dashed line in Fig. 4.4). In Fig. 4.8 we depict this mode, which still transforms as the A_1 of graphene **K**-point on the microscopic graphene scale, but whose long-wavelength modulation now forms a series of ellipses elongated along some of the DWs, thus macroscopically breaking the C_{3z} symmetry of the moiré superlattice.
In Fig. 4.9 we show the DOS of the FBs obtained by a frozen-phonon realistic tight-binding calculation. Besides the band gaps at $\nu = \pm 4$, which separates the FBs from the others bands, now small gaps opens at $\nu = \pm 2$ with an average atomic displacement of 1.8 mÅ induced by the mode at **M**.
Finally we also considered a more exotic multi-component distortion induced by a combination of the modes at the three inequivalent **M** points, which quadruples the unit cell (see Fig. 4.10). The resulting DOS of the FBs is shown in Fig. 4.11, and displays small gaps at the odd integer occupancies $\nu = 1$ and $\nu = \pm 3$. The very qualitative conclusion of this exploration is that frozen phonon distortions with various **k**-vectors can very effectively yield Peierls-like insulating states at integer hole/electron fillings. Of course all distortions at **k**-points different from Γ also represent super-superlattices, with an enlargement of the unit cell that should be verifiable in such a Peierls state, even if the displacement is a tiny fraction of the equilibrium C–C distance. We note here that the the zone boundary phonons are less effective in opening gaps at non zero integer fillings than the zone center phonons are at the charge neutrality point. The reason is that away from charge neutrality the Jahn-Teller effect alone is no longer sufficient; one needs to invoke zone boundary phonons that enlarge the unit cell, and thus open gaps at the boundaries of the folded Brillouin zone. The efficiency of such gap opening mechanism is evidently lower than that of the Jahn-Teller **Γ**-point mode.

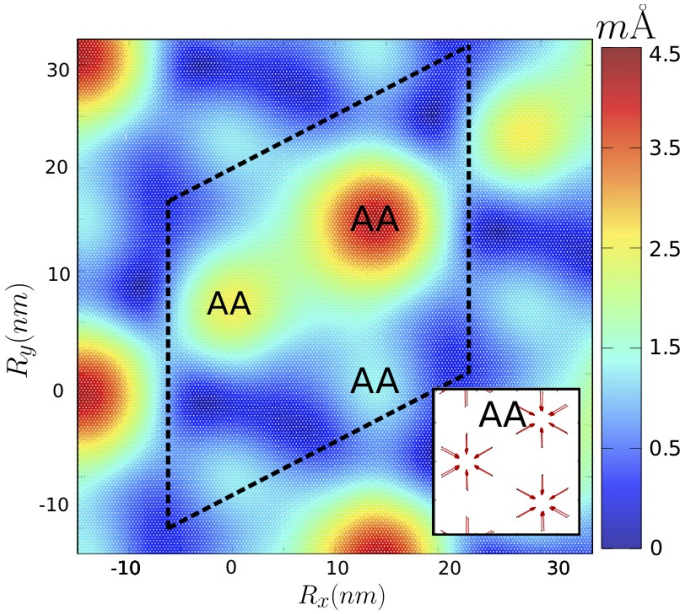

Figure 4.10: Atomic displacements on one of the two layers corresponding to multicomponent deformation obtained combining moiré JT phonons at three inequivalent **M** points. The mean deformation is 1.7 mÅ and leads to the DOS in Fig. 4.11. The intensity of displacement is encoded in colors. The inset shows a zoom in one of the AA regions when both layers are considered. The unit cell, denoted by a black dashed line, is four times larger than the original one.

4.1.6 C_{3z} symmetry breaking

We observe that the multicomponent distortion with the phonons frozen at the inequivalent **M** points leads to a width of the FBs five times larger than in the undistorted case, see Fig. 4.11 as opposed to Fig. 4.6 a), which is not simply a consequence of the tiny gaps that open at the boundary of the reduced Brillouin zone. Such substantial bandwidth increase suggests that the tBLG may be intrinsically unstable to C_{3z} symmetry breaking, especially near charge neutrality. Electron-electron interaction treated in mean-field does a very similar job [17]. Essentially, both interaction- and phonon-driven mechanisms act right in the same manner: they move the two van Hove singularities of the fully symmetric band structure away from each other, and split them into two, with the net effect of increasing the bandwidth. As such, those two mechanisms will cooperate to drive the C_{3z} symmetry breaking, or enhance it when explicitly broken by strain, not in disagreement with experiments [16, 17, 20]. The main difference is that the moiré phonons also break $U_v(1)$, and thus are able to open gaps at commensurate fillings that C_{3z} symmetry breaking alone would not do.

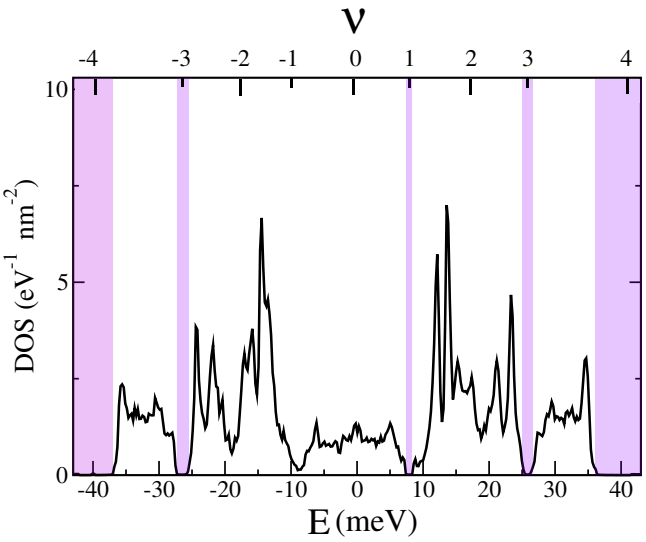

Figure 4.11: Electronic density of states with a multicomponent lattice distortion obtained by freezing a combination of the modes at the three inequivalent **M** points. Band gaps at $\nu = +1, \pm 3, \pm 4$ are highlighted in violet. The mean displacement per atom is 1.7 mÅ.

4.2 Phonon mediated superconductivity

In this Section we work out the properties of the superconducting state that might be stabilized by the moiré Jahn-Teller phonons. Neglecting their extremely small dispersion, we can write their Hamiltonian simply as

$$H_{\text{ph}} = \frac{\omega}{2} \sum_{\mathbf{R}} \left(\mathbf{p}_{\mathbf{R}} \cdot \mathbf{p}_{\mathbf{R}} + \mathbf{q}_{\mathbf{R}} \cdot \mathbf{q}_{\mathbf{R}} \right), \tag{4.9}$$

with $\omega \simeq 207$ meV.
Rather than trying to model more faithfully the Jahn-Teller coupling (4.7), we shall follow a simplified approach based just on symmetry considerations.
In general, we could integrate out the phonons to obtain a retarded electron-electron attraction that can mediate superconductivity. However, since here the phonon frequency is much larger that the bandwidth of the FBs, where the chemical potential lies, we can safely neglect retardation effects making a BCS-type approximation virtually exact. The attraction thus becomes instantaneous and can be represented as in Fig. 4.12. The phonon couples electrons in nearest neighbor AB and BA regions, giving rise to an inter-moiré site spin-singlet pairing, a state which we expect to be much less affected by Coulomb repulsion than an on-site one. Therefore, neglecting Coulomb repulsions we can concentrate on the pairing channel between nearest neighbor AB and BA regions. The scattering processes in Fig. 4.12 imply that the pairing channels are only $\tau_1 \mu_0$ and $\tau_1 \mu_3$, corresponding to inter valley pairing, as expected because time reversal interchanges the two valleys.
Having assumed pairing between Wannier orbitals centered in nearest neighbor AB and BA regions, we must identify pair functions in momentum space that connect nearest neighbor unit cells, and transform properly under C_{3z}. These functions are

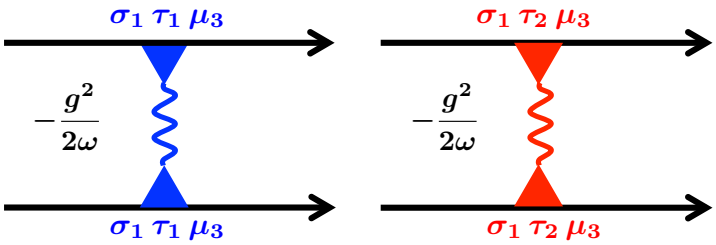

Figure 4.12: Phonon mediated attraction. The two scattering channels corresponds to the two phonons and have the same amplitude $g^2/2\omega$.

$$\begin{aligned}\gamma(\mathbf{k}) &= e^{i\mathbf{k}\cdot(\mathbf{a}+\mathbf{b})/3}\left(1+e^{-i\mathbf{k}\cdot\mathbf{a}}+e^{-i\mathbf{k}\cdot\mathbf{b}}\right),\\ \gamma_{+1}(\mathbf{k}) &= e^{i\mathbf{k}\cdot(\mathbf{a}+\mathbf{b})/3}\left(1+\omega\, e^{-i\mathbf{k}\cdot\mathbf{a}}+\omega^* e^{-i\mathbf{k}\cdot\mathbf{b}}\right),\\ \gamma_{-1}(\mathbf{k}) &= e^{i\mathbf{k}\cdot(\mathbf{a}+\mathbf{b})/3}\left(1+\omega^* e^{-i\mathbf{k}\cdot\mathbf{a}}+\omega\, e^{-i\mathbf{k}\cdot\mathbf{b}}\right),\end{aligned} \tag{4.10}$$

where $\omega = e^{i2\pi/3}$. Specifically, $\gamma(\mathbf{k}) \sim A_1$ is invariant under C_{3z}, while

$$\gamma_{\pm1}\big(C_{3z}(\mathbf{k})\big) = \omega^{\pm1}\,\gamma_{\pm1}(\mathbf{k})\,. \tag{4.11}$$

In other words, $(\gamma_{+1}(\mathbf{k}), \gamma_{-1}(\mathbf{k}))$ form a representation of the 2d-irrep $E = (E_{+1}, E_{-1})$ in which C_{3z} is diagonal with eigenvalues ω and ω^*.

Here it is more convenient to transform the spinor $\Phi_{\mathbf{k}\sigma}$

$$\begin{pmatrix}\Phi_{+1,\mathbf{k}\sigma}\\ \Phi_{-1,\mathbf{k}\sigma}\end{pmatrix} = \frac{1}{\sqrt{2}}\begin{pmatrix}1 & -i\\ 1 & +i\end{pmatrix}\begin{pmatrix}\Phi_{s,\mathbf{k}\sigma}\\ \Phi_{p,\mathbf{k}\sigma}\end{pmatrix}, \tag{4.12}$$

so that $\Phi_{\pm1,\mathbf{k}\sigma}$ is associated with a WO that transforms like $E_{\pm1}$. Under the assumption of pairing diagonal in the irreps, we can construct the following spin-singlet Cooper pairs:

$$\sum_\sigma \sigma\,\Phi^\dagger_{+1,AB,\mathbf{k}\sigma}\,\tau_1\,\Phi^\dagger_{+1,BA,-\mathbf{k}-\sigma} \;\sim\; E_{-1,\mathbf{k}}\,, \tag{4.13}$$

$$\sum_\sigma \sigma\,\Phi^\dagger_{-1,AB,\mathbf{k}\sigma}\,\tau_1\,\Phi^\dagger_{-1,BA,-\mathbf{k}-\sigma} \;\sim\; E_{+1,\mathbf{k}}\,, \tag{4.14}$$

$$\frac{1}{\sqrt{2}}\sum_\sigma \sigma\Big(\Phi^\dagger_{+1,AB,\mathbf{k}\sigma}\,\tau_1\,\Phi^\dagger_{-1,BA,-\mathbf{k}-\sigma} + (-)\Phi^\dagger_{-1,AB,\mathbf{k}\sigma}\,\tau_1\,\Phi^\dagger_{+1,BA,-\mathbf{k}-\sigma}\Big) \;\sim\; A_{1(2),\mathbf{k}}\,, \tag{4.15}$$

$$\frac{1}{\sqrt{2}}\sum_\sigma \sigma\,\Psi^\dagger_{AB,\mathbf{k}\sigma}\,\tau_1\,\mu_{0(3)}\,\Psi^\dagger_{BA,-\mathbf{k}-\sigma} \;\sim\; A'_{1(2),\mathbf{k}}\,, \tag{4.16}$$

which can be combined with the $\mathbf{k}$-dependent functions in (4.10) to give pair operators that transform like the irreps of D_3. For instance, multiplying (4.13) by $\gamma_{+1}(\mathbf{k})$, (4.14) by $\gamma_{-1}(\mathbf{k})$, (4.15) with the plus sign by $\gamma(\mathbf{k})$, or (4.16) with μ_0 by $\gamma(\mathbf{k})$, we obtain pair operators that all transform like A_1. We shall denote their sum as $\mathbf{A}^\dagger_{1\mathbf{k}}$, and, similarly, all other symmetry combinations as $\mathbf{A}^\dagger_{2\mathbf{k}}$ and $\mathbf{E}^\dagger_{\pm1,\mathbf{k}}$. Evidently, since in our modeling the FBs are made of 1d and 2d irreps, the gap function

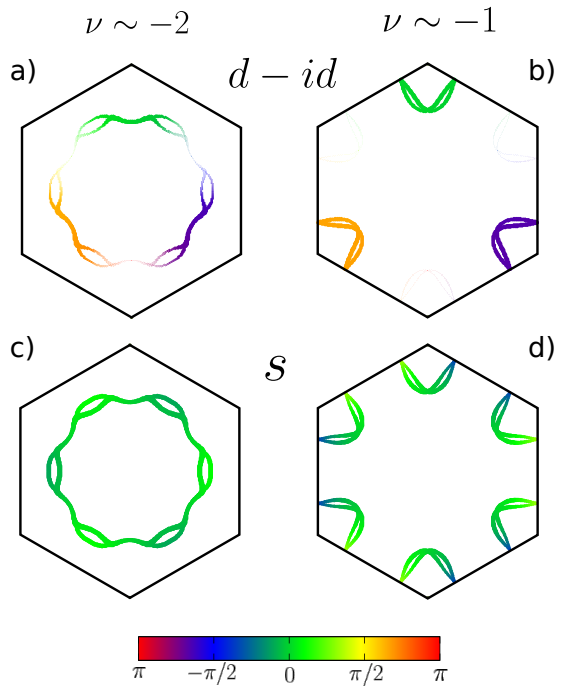

Figure 4.13: Pair amplitudes $\Delta(k)^\dagger$ of the leading superconducting channels: $d - id$-wave (a-b) and extended s-wave (c-d). In each panel we show the hexagonal MBZ and the phase amplitudes restricted to a narrow region close to the Fermi surfaces corresponding to the occupancies $\nu \sim -2$ (a-c) and $\nu \sim -1$ (b-d). The phase of the superconducting order parameter is expressed in color. Note that the double line are due to the fact that two bands cross the chemical potential at different $\mathbf{k}$-points.

will in general involve a combination of $\gamma(\mathbf{k})$ and $\gamma_{\pm 1}(\mathbf{k})$, namely, it will be a superposition of s and $d \pm id$ symmetry channels. The dominant channel will depend on which is the prevailing WO character of the Bloch states at the chemical potential, as well as on the strength of the scattering amplitudes in the different pairing channels, $\mathbf{A}^\dagger_{1\mathbf{k}}$, $\mathbf{A}^\dagger_{2\mathbf{k}}$ and $\mathbf{E}^\dagger_{\pm 1,\mathbf{k}}$.
In general, we may expect the totally-symmetric A_1 channel to have the largest amplitude, thus we assume the following expression of the phonon-mediated attraction

$$H_{\text{el-el}} \simeq -\frac{\lambda}{V} \sum_{\mathbf{kp}} \mathbf{A}^\dagger_{1\mathbf{k}} \mathbf{A}_{1\mathbf{p}} \,, \tag{4.17}$$

that involves a single parameter $\lambda \sim g^2/2\omega$. We treat the full Hamiltonian (3.32) plus (4.17) in mean field allowing for a superconducting solution, which is always stabilized by the attraction provided the density of states is finite at the chemical potential. We find that superconductivity opens a gap everywhere in the Brillouin zone. Since

$$\langle \mathbf{A}^\dagger_{1\mathbf{k}} \rangle = \gamma_{+1}(\mathbf{k}) \langle E_{-1,\mathbf{k}} \rangle + \gamma_{-1}(\mathbf{k}) \langle E_{+1,\mathbf{k}} \rangle + \gamma(\mathbf{k}) \langle A_{1,\mathbf{k}} \rangle + \gamma(\mathbf{k}) \langle A'_{1,\mathbf{k}} \rangle \,, \tag{4.18}$$

the order parameter may have finite components with different symmetries, $E_{\pm 1}$ and A_1. In the model calculation all components acquire similar magnitude, implying a mixture of s and $d \pm id$ wave symmetries. In Fig. 4.13 we show $\langle A'_{1,\mathbf{k}} \rangle$ and $\langle E_{-1,\mathbf{k}} \rangle$ at the Fermi surface corresponding to densities $\nu \approx -1$ and $\nu \approx -2$ with respect to charge neutrality. We conclude by emphasizing that the Cooper pair is made by one electron in AB and one in BA, thus leading, in the spin-singlet channel, to extended s and/or $d \pm id$ symmetries. That is merely a consequence of the phonon mode and electron-phonon properties, hence it does not depend on the above modeling of the FBs.

There are already in literature several proposals about the superconducting states in tBLG. Most of them, however, invoke electron correlations as the element responsible, or strongly effecting the pairing [99, 77, 100, 101, 102, 85, 103, 104, 105, 106, 107, 108, 109, 110, 111, 112, 113, 114, 115]. There are few exceptions [116, 29, 25] that instead propose, as we do, a purely phonon mediated attraction. In both works [116] and [29] the tBLG phonons are assumed to coincide with the single layer graphene ones, as if the interlayer coupling were ineffective in the phonon spectrum, which is not what we find for the special modes discussed above. Moreover, they both discuss the effects of such phonons only in a continuum model for the FBs. In particular, the authors of [116] consider a few selected graphene modes, among which the transverse optical mode at **K** that has the largest weight in the tBLG phonon that we consider. They conclude that such graphene mode mediates $d \pm id$ pairing in the A_2 channel, $\tau_1\,\mu_3$ in our language, leading to an order parameter odd upon interchanging the two layers. On the contrary, the authors of [29] focus just on the acoustic phonons of graphene, and conclude they stabilize an extended s-wave order parameter.

4.3 Coupling to moiré phonons in the continuum model formalism of twisted bilayer graphene

In this Section we work out how the Jahn-Teller mechanism described previously can be implemented in the continuum model formalism. This method is more manageable than the realistic tight-binding modelling of Section 2.3.1, whose results can be reproduced with much less effort. In addition, the continuum model formalism has the great advantage of providing a full quantum mechanical expression of the electron-phonon Hamiltonian, which may allow going beyond a simple frozen-phonon calculation , and thus describing phenomena like a dynamical Jahn-Teller effect and the phonon-mediated superconductivity.

4.3.1 Perturbation induced by a static atomic displacement

We derive in the continuum model the expression of the perturbation induced by a collective atomic displacement. Under a generic lattice deformation, the in-plane atomic positions $\mathbf{x}_{i\alpha}$ change according to

$$\mathbf{x}_{i\alpha} \equiv \mathbf{R}_i + \mathbf{r}_{i\alpha} \to \mathbf{R}_i + \mathbf{r}_\alpha + \boldsymbol{u}_i(\mathbf{x}_{i\alpha}) = \mathbf{x}_{i\alpha} + \boldsymbol{u}_i(\mathbf{x}_{i\alpha})\,, \tag{4.19}$$

where i is now labeling a generic unit cell position. Since the phonon modes we are going to study involve only in-plane atomic displacements, we assume that z-coordinate of each carbon atom does not vary. It follows that a generic potential in the two-centers approximation and at linear order in the displacement reads

$$T\Big(\mathbf{x}_{i\alpha} - \mathbf{x}_{j\beta}, z_{i\alpha} - z_{j\beta}\Big) \to T\Big(\mathbf{x}_{i\alpha} - \mathbf{x}_{j\beta}, z_{i\alpha} - z_{j\beta}\Big) + \boldsymbol{W}\Big(\mathbf{x}_{i\alpha} - \mathbf{x}_{j\beta}, z_{i\alpha} - z_{j\beta}\Big) \cdot \Big(\boldsymbol{u}_i(\mathbf{x}_{i\alpha}) - \boldsymbol{u}_j(\mathbf{x}_{j\beta})\Big)\,, \tag{4.20}$$

We further neglect the dependence on z, which we will take into account by distinguishing at the end between different scattering channels, intra- and inter-layers, so that:

$$\boldsymbol{W}(\mathbf{r}) = \frac{1}{N}\sum_{\mathbf{q}} \mathrm{e}^{i\mathbf{q}\cdot\mathbf{r}}\, \boldsymbol{W}(\mathbf{q}) = \boldsymbol{\nabla}\, T(\mathbf{r}) = i\,\frac{1}{N}\sum_{\mathbf{q}} \mathbf{q}\, T(\mathbf{q})\, \mathrm{e}^{i\mathbf{q}\cdot\mathbf{r}}\,, \tag{4.21}$$

namely

$$\boldsymbol{W}(\mathbf{q}) = i\mathbf{q}\, T(\mathbf{q}) = i\mathbf{q}\, T(q)\,, \tag{4.22}$$

assuming that $T(\mathbf{q})$ depends only on $q = |\mathbf{q}|$.

4.3.2 Deformation fields approximating the Jahn-Teller moiré phonon modes

In the previous Section 4.1.2, we pointed out the existence of a pair of high-frequency optical modes at the $\mathbf{\Gamma}$ point of the MBZ, which are extremely efficient in lifting the valley degeneracies observed in the band structure. These two modes, microscopically, both look as the well-known in-plane optical phonon modes of graphene at $\mathbf{K}$, which transform as the A_1 and B_1 irreducible representations. These two irreducible representations differ by the fact that B_1 is odd with respect to $\mathbf{C_{2z}}$ and $\mathbf{C_{2y}}$, while A_1 is even with respect to all symmetries of the D_6 space group. Although the complexity of these modes is hard to capture by a simple analytical expression, their effect on the band structure can be well approximated introducing the following deformation fields

$$\begin{aligned} \boldsymbol{u}_c^{(a)}\left(\mathbf{x}_\alpha^{(a)}\right) &= \sum_{i=1}^{3}\sum_{j=0}^{2} \boldsymbol{u}_\alpha^{(a)}(\mathbf{Q}_{ij})\,\cos\left((\mathbf{R}^{(a)}+\mathbf{r}_\alpha^{(a)})\cdot\mathbf{Q}_{ij}\right), \\ \boldsymbol{u}_s^{(a)}\left(\mathbf{x}_\alpha^{(a)}\right) &= \sum_{i=1}^{3}\sum_{j=0}^{2} \boldsymbol{v}_\alpha^{(a)}(\mathbf{Q}_{ij})\,\sin\left((\mathbf{R}^{(a)}+\mathbf{r}_\alpha^{(a)})\cdot\mathbf{Q}_{ij}\right). \end{aligned} \tag{4.23}$$

were $\mathbf{Q}_{ij}$ are the k-vectors connecting different valleys and depicted in Fig.4.2, while $a = 1, 2$ is the layer index. Since the transformation $\mathbf{C}_g$ ($g = 3z, 2x$) is a symmetry operation even in the distorted lattice, we have that

$$\mathbf{C}_g\left(\mathbf{x}_\alpha^{(a)}\right) = \mathbf{x}_\beta^{(b)} \longrightarrow \mathbf{C}_g\left(\boldsymbol{u}^{(a)}(\mathbf{x}_\alpha^{(a)})\right) = \boldsymbol{u}^{(b)}(\mathbf{x}_\beta^{(b)})\,. \tag{4.24}$$

By noting that the set of momenta $\{\mathbf{Q}_{ij}\}$ is invariant under $\mathbf{C}_{3z}$ and $\mathbf{C}_{2x}$, it immediately follows that, for $g = 3z, 2x$

$$\begin{aligned} \mathbf{C}_g\left(\boldsymbol{u}_\alpha^{(a)}(\mathbf{Q}_{ij})\right) &= \boldsymbol{u}_\beta^{(b)}\left(\mathbf{C}_g(\mathbf{Q}_{ij})\right). \\ \mathbf{C}_g\left(\boldsymbol{v}_\alpha^{(a)}(\mathbf{Q}_{ij})\right) &= \boldsymbol{v}_\beta^{(b)}\left(\mathbf{C}_g(\mathbf{Q}_{ij})\right). \end{aligned} \tag{4.25}$$

On the contrary, $\{\mathbf{Q}_{ij}\}$ is not invariant under C_g ($g = 2y, 2z$), and the phonon modes are either even (A_1) or odd (B_1) under these symmetries. Therefore, recalling that $\mathbf{C}_{2z}$ exchanges the two sublattices,

$$\begin{aligned} \mathbf{C}_{2z}\left(\boldsymbol{u}_A^{(a)}(\mathbf{Q}_{ij})\right) &= -\boldsymbol{u}_A^{(a)}(\mathbf{Q}_{ij}) = \pm\boldsymbol{u}_B^{(a)}(\mathbf{Q}_{ij}), \\ \mathbf{C}_{2z}\left(\boldsymbol{v}_A^{(a)}(\mathbf{Q}_{ij})\right) &= -\boldsymbol{v}_A^{(a)}(\mathbf{Q}_{ij}) = \mp\boldsymbol{v}_B^{(a)}(\mathbf{Q}_{ij}). \end{aligned} \tag{4.26}$$

If we choose

$$\boldsymbol{u}_A^{(a)}(\mathbf{Q}_{ij}) = \boldsymbol{u}_B^{(a)}(\mathbf{Q}_{ij})\,, \boldsymbol{v}_A^{(a)}(\mathbf{Q}_{ij}) = \boldsymbol{v}_B^{(a)}(\mathbf{Q}_{ij})\,, \tag{4.27}$$

then the cosine distortion in (4.23) $\boldsymbol{u}_c^{(a)}\left(\mathbf{x}_\alpha^{(a)}\right)$ transforms as B_1, while the sine one, $\boldsymbol{u}_s^{(a)}\left(\mathbf{x}_\alpha^{(a)}\right)$, as A_1. They both can be shortly written as

$$\boldsymbol{u}^{(a)}\left(\mathbf{x}_\alpha^{(a)}\right) = \sum_{i=1}^{3}\sum_{j=0}^{2}\left[\boldsymbol{u}^{(a)}\left(\mathbf{Q}_{ij}\right)\mathrm{e}^{i\left(\mathbf{R}^{(a)}+\mathbf{r}_\alpha^{(a)}\right)\cdot\mathbf{Q}_{ij}} + c.c.\right], \tag{4.28}$$

where $\boldsymbol{u}^{(a)}(\mathbf{Q}_{ij})^* \equiv \boldsymbol{u}^{(a)}(-\mathbf{Q}_{ij})$ and $\boldsymbol{u}^{(a)}(\mathbf{Q}_{ij})$ is real for the B_1 distortion and imaginary for A_1. We end by pointing out that $\boldsymbol{W}(\mathbf{q})$ satisfies

$$\mathbf{C}_g(\boldsymbol{W}(\mathbf{q})) = \boldsymbol{W}\left(\mathbf{C}_g(\mathbf{q})\right), \tag{4.29}$$

for all symmetry operations of the lattice, in particular

$$\mathbf{C}_{2z}\Big(\boldsymbol{W}(\mathbf{q})\Big) = -\boldsymbol{W}(\mathbf{q}) = \boldsymbol{W}\Big(\mathbf{C}_{2z}(\mathbf{q})\Big) = \boldsymbol{W}(-\mathbf{q}) = \boldsymbol{W}(\mathbf{q})^* \,. \tag{4.30}$$

4.3.3 Phonon induced Hamiltonian matrix elements

A lattice distortion involving the A_1 or B_1 phonons generates a matrix element between layer a momentum $\mathbf{k} \sim \mathbf{K}^{(a)}$ and layer b momentum $\mathbf{p} \sim -\mathbf{K}^{(b)}$, where we recall that $\mathbf{K}^{(1)} = \mathbf{K}_2$ and $\mathbf{K}^{(2)} = \mathbf{K}_1$ in Fig. 2.1(d):

$$\begin{aligned} W(a,\mathbf{k},\alpha;b,\mathbf{p},\beta) = \quad & \frac{1}{N^2}\sum_{\mathbf{q}\mathbf{Q}_{ij}}\sum_{\mathbf{R}^{(a)}\mathbf{R}^{(b)}} \boldsymbol{W}(-\mathbf{q})\cdot\Big[\boldsymbol{u}^{(a)}\Big(\mathbf{Q}_{ij}\Big)\,\mathrm{e}^{-i\left(\mathbf{k}+\mathbf{q}-\mathbf{Q}_{ij}\right)\cdot\left(\mathbf{R}^{(a)}+\mathbf{r}_\alpha^{(a)}\right)}\;\mathrm{e}^{i(\mathbf{p}+\mathbf{q})\cdot\left(\mathbf{R}^{(b)}+\mathbf{r}_\beta^{(b)}\right)} \\ & \qquad -\boldsymbol{u}^{(b)}\Big(\mathbf{Q}_{ij}\Big)\,\mathrm{e}^{-i(\mathbf{k}+\mathbf{q})\cdot\left(\mathbf{R}^{(a)}+\mathbf{r}_\alpha^{(a)}\right)}\;\mathrm{e}^{i\left(\mathbf{p}+\mathbf{q}+\mathbf{Q}_{ij}\right)\cdot\left(\mathbf{R}^{(b)}+\mathbf{r}_\beta^{(b)}\right)}\Big] \\ = \quad & \sum_{\mathbf{q}\mathbf{Q}_{ij}}\sum_{\mathbf{G}^{(a)}\mathbf{G}^{(b)}} \boldsymbol{W}(-\mathbf{q})\cdot\Big[\delta_{-\mathbf{q},\mathbf{k}-\mathbf{Q}_{ij}+\mathbf{G}^{(a)}}\,\delta_{-\mathbf{q},\mathbf{p}+\mathbf{G}^{(b)}}\,\boldsymbol{u}^{(a)}\Big(\mathbf{Q}_{ij}\Big)\,\mathrm{e}^{i\mathbf{G}^{(a)}\cdot\mathbf{r}_\alpha^{(a)}-i\mathbf{G}^{(b)}\cdot\mathbf{r}_\beta^{(b)}} \\ & \qquad -\delta_{-\mathbf{q},\mathbf{k}+\mathbf{G}^{(a)}}\,\delta_{-\mathbf{q},\mathbf{p}+\mathbf{Q}_{ij}+\mathbf{G}^{(b)}}\,\boldsymbol{u}^{(b)}\Big(\mathbf{Q}_{ij}\Big)\,\mathrm{e}^{i\mathbf{G}^{(a)}\cdot\mathbf{r}_\alpha^{(a)}-i\mathbf{G}^{(b)}\cdot\mathbf{r}_\beta^{(b)}}\Big]. \end{aligned}$$

We can readily follow the same steps outlined in section 2.3.2 to identify the $\mathbf{G}^{(a)}$ and $\mathbf{G}^{(b)}$ reciprocal lattice vectors that enforce momentum conservation and maximize the matrix element $W(-\mathbf{q}) = W(\mathbf{q})$. Therefore, we shall not repeat that calculation and jump directly to the results.

The lattice distortion introduces a perturbation both intra-layer and inter-layer. The former, in the representation introduced in Appendix A, has the extremely simple expression:

$$\delta\hat{H}^{\parallel}_{x(y)}(\mathbf{k})_{\mathbf{Q}\mathbf{Q}'} = \tau_{x(y)}\sum_{i=1}^{3}\left(\delta_{\mathbf{Q}'-\mathbf{Q},\mathbf{q}_i}+\delta_{\mathbf{Q}-\mathbf{Q}',\mathbf{q}_i}\right)\hat{T}_i(g,g') \equiv \tau_{x(y)}\,\delta\hat{H}^{\parallel}_{\mathbf{Q}\mathbf{Q}'}\,, \tag{4.31}$$

where τ_x refers to the A_1 mode, τ_y to the B_1 one, and the matrices $\hat{T}_i(g,g')$ have the same expression as those in Eq. (2.30), with u and u' replaced, respectively, by g and g'.

The inter layer coupling has a simpler expression, since, as we mentioned previously, opposite valleys in different layers fold on the same momentum in the MBZ, and thus the coupling is diagonal in $\mathbf{Q}$ and $\mathbf{Q}'$ and reads

$$\delta\hat{H}^{\perp}_{x(y)}(\mathbf{k})_{\mathbf{Q}\mathbf{Q}'} = \delta_{\mathbf{Q},\mathbf{Q}'}\,\gamma\,\sigma_0\,\tau_{x(y)} \equiv \tau_{x(y)}\,\delta\hat{H}^{\perp}_{\mathbf{Q}\mathbf{Q}'}\,. \tag{4.32}$$

As before τ_x and τ_y refers to the A_1 and B_1 modes, respectively.
It is worth remarking that, because of the transformation (A.11), which exchanges the sublattices in the valley $\zeta = -1$, the diagonal elements of the matrices $\hat{T}_i(g,g')$ in (4.31) and σ_0 in (4.32) refer to the opposite sublattices, while the diagonal elements to the same sublattice, right the opposite of the unperturbed Hamiltonian (A.12).

Let us rephrase the above results in second quantization and introducing the quantum mechanical character of the phonon mode. In the continuum model, a plane wave with momentum $\mathbf{k}+\mathbf{G}$, where $\mathbf{G} = n\mathbf{G}_1 + m\mathbf{G}_2$ is a reciprocal lattice vector of the MBZ, in layer $i = 1,2$, valley $\zeta = +1$

and with sublattice components described by a two-component spinor $\chi_{\mathbf{k}+\mathbf{G}}$ can be associated to a two component spinor operator according to

$$e^{i(\mathbf{k}+\mathbf{G})\cdot\mathbf{r}}\,\chi_{\mathbf{k}+\mathbf{G}} \longrightarrow \Psi^{(i)}_{+1,\mathbf{k}+\mathbf{G}}\,. \tag{4.33}$$

For any $\mathbf{G}$ we can write, see Eq. (A.2),

$$\mathbf{G} = \mathbf{K}_1 - \mathbf{Q}_A = \mathbf{K}_2 - \mathbf{Q}_B\,, \tag{4.34}$$

and thus define

$$\begin{aligned}\Psi^{(1)}_{+1,\mathbf{k}+\mathbf{G}} &= \Psi^{(1)}_{+1,\mathbf{k}+\mathbf{K}_2-\mathbf{Q}_B} \equiv \Psi_{\mathbf{k},\mathbf{Q}_B,+1}\,,\\ \Psi^{(2)}_{+1,\mathbf{k}+\mathbf{G}} &= \Psi^{(1)}_{+1,\mathbf{k}+\mathbf{K}_1-\mathbf{Q}_A} \equiv \Psi_{\mathbf{k},\mathbf{Q}_A,+1}\,.\end{aligned} \tag{4.35}$$

We note that $\mathbf{K}_{+\phi} + \mathbf{K}_{-\phi} \equiv \mathbf{G}_k = (2k+1)\,(\mathbf{G_1} + \mathbf{G}_2)$, which allows us defining the operators in valley $\zeta = -1$ as

$$\begin{aligned}\Psi^{(1)}_{-1,\mathbf{k}+\mathbf{G}-\mathbf{G}_k} &= \Psi^{(1)}_{-1,\mathbf{k}-\mathbf{K}_{+\phi}-\mathbf{Q}_A} \equiv \sigma_x\,\Psi_{\mathbf{k},\mathbf{Q}_A,-1}\,,\\ \Psi^{(2)}_{-1,\mathbf{k}+\mathbf{G}-\mathbf{G}_k} &= \Psi^{(2)}_{+1,\mathbf{k}-\mathbf{K}_{-\phi}-\mathbf{Q}_B} \equiv \sigma_x\,\Psi_{\mathbf{k},\mathbf{Q}_B,-1}\,,\end{aligned} \tag{4.36}$$

where, in accordance with our transformation in Eq. (A.11), we interchange the two sublattices in valley $\zeta = -1$ through σ_x. We note that the mismatch momentum $\mathbf{G}_k$ is just what is provided by the phonon modes. Absorbing the valley index into two additional components of the spinors, and introducing back the spin label, the second quantized Hamiltonian can be written in terms of four component spinor operators $\Psi_{\mathbf{k}\sigma,\mathbf{Q}}$, where, $\mathbf{Q} = \mathbf{Q}_A$ refer to layer 2 if the valley index $\zeta = +1$ and layer 1 if $\zeta = -1$, while $\mathbf{Q} = \mathbf{Q}_B$ to layer 1 if $\zeta = +1$, and layer 2 if $\zeta = -1$.
Next, we introduce a two component dimensionless variable $\mathbf{q_0} = (q_1, q_2)$, and its conjugate one, $\mathbf{p_0} = (p_1, p_2)$, where q_1 and q_2 are the phonon coordinates of the A_1 and B_1 modes at $\mathbf{\Gamma} = \mathbf{0}$, respectively. Using the above defined operators, the full quantum mechanical Hamiltonian reads

$$H = \sum_{\mathbf{kQ}\sigma}\Big[\,\Psi^{\dagger}_{\mathbf{k}\sigma\mathbf{Q}}\,\hat{H}_{\mathbf{QQ}'}(\mathbf{k})\,\Psi_{\mathbf{k}\sigma\mathbf{Q}'} + \Psi^{\dagger}_{\mathbf{k}\sigma\mathbf{Q}}\big(\boldsymbol{q_0}\cdot\boldsymbol{\tau}\,\delta\hat{H}_{\mathbf{QQ}'}\big)\Psi_{\mathbf{k}\sigma\mathbf{Q}'}\,\Big] + \frac{\omega_{\mathbf{0}}}{2}\Big(\,\mathbf{p_0}\cdot\mathbf{p_0} + \mathbf{q_0}\cdot\mathbf{q_0}\Big)\,, \tag{4.37}$$

where $\omega_{\mathbf{0}}$ is the phonon frequency, equal for both A_1 and B_1 modes, $\boldsymbol{\tau} = (\tau_x, \tau_y)$, and

$$\begin{aligned}\hat{H}_{\mathbf{QQ}'}(\mathbf{k}) &= \delta_{\mathbf{QQ}'}\,v\,\tau_z\,(\mathbf{k}-\mathbf{Q})\cdot\boldsymbol{\sigma} + \tau_0\sum_{i=1}^{3}\Big(\delta_{\mathbf{Q}'-\mathbf{Q},\mathbf{q}_i} + \delta_{\mathbf{Q}-\mathbf{Q}',\mathbf{q}_i}\Big)\,\hat{T}_i(u,u')\,,\\ \delta\hat{H}_{\mathbf{QQ}'} &= \delta\hat{H}^{\parallel}_{\mathbf{QQ}'} + \delta\hat{H}^{\perp}_{\mathbf{QQ}'} = \sum_{i=1}^{3}\Big(\delta_{\mathbf{Q}'-\mathbf{Q},\mathbf{q}_i} + \delta_{\mathbf{Q}-\mathbf{Q}',\mathbf{q}_i}\Big)\,\hat{T}_i(g,g') + \delta_{\mathbf{Q},\mathbf{Q}'}\,\gamma\,.\end{aligned} \tag{4.38}$$

As in Eq.4.7, we observe that the Hamiltonian (4.37) still possesses a valley $U_v(1)$ symmetry, with generator

$$J_z = \frac{1}{2}\sum_{\mathbf{kQ}\sigma}\Psi^{\dagger}_{\mathbf{k}\sigma\mathbf{Q}}\,\sigma_0\,\tau_z\,\Psi_{\mathbf{k}\sigma\mathbf{Q}} + \mathbf{q_0}\wedge\mathbf{p_0} \equiv T_z + L_z\,, \tag{4.39}$$

where T_z is half the difference between the number of electrons in valley $\zeta = +1$ and the one in valley $\zeta = -1$, while L_z is the angular momentum of the phonon mode. The Hamiltonian (4.37) actually realises a $e \otimes E$ Jahn-Teller model.

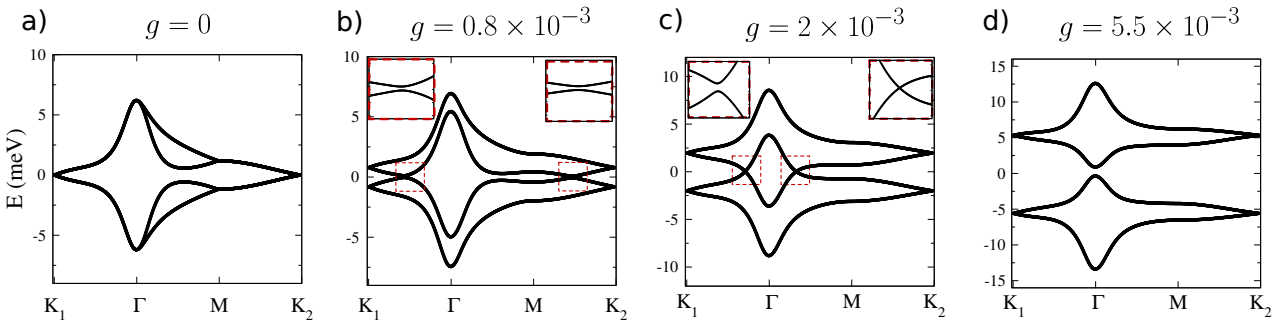

Figure 4.14: Band structure of $2\phi = 1.08°$ twisted bilayer graphene with increasing frozen phonon deformation intensity g. The other parameters used in this calculation are: $u = 0.0761$, $u' = 0.1031$, $g' = g/10$ and $\gamma = g/2.5$. a) Undistorted case. b) Slightly distorted lattice. Two small avoided crossings occur along the $\mathbf{K}_1 \to \mathbf{\Gamma}$ and $\mathbf{M} \to \mathbf{\Gamma}$ lines. c) By further increasing the distortion intensity the four bands further separate. The avoided crossing along $\mathbf{K}_1 \to \mathbf{\Gamma}$ persists, while a genuine crossing occur along $\mathbf{\Gamma} \to \mathbf{M}$. d) A gap at charge neutrality has finally opened.

It is straightforward to generalise the above result to an atomic displacement modulated with the wave vectors $\mathbf{Q}_{ij} + \boldsymbol{P}$, where $\boldsymbol{P} \in$ MBZ. Since $\mathbf{Q}_{ij}$ are multiples of the MBZ reciprocal lattice vector, such displacement is at momentum $\boldsymbol{P}$, and can be considered as the previous one at $\mathbf{\Gamma}$, shown in Fig. 4.2, on top of which we add an additional incommensurate long wavelength component. Since $\boldsymbol{P}$ is small as compared to the vectors $\mathbf{Q}_{ij}$, we shall assume that the displacement has the same expression of Eq. (4.28), with the only difference that

$$e^{\pm i\left(\mathbf{R}^{(a)}+\mathbf{r}_\alpha^{(a)}\right)\cdot\mathbf{Q}_{ij}} \longrightarrow e^{\pm i\left(\mathbf{R}^{(a)}+\mathbf{r}_\alpha^{(a)}\right)\cdot\left(\mathbf{Q}_{ij}\pm\boldsymbol{P}\right)} . \tag{4.40}$$

The full quantum mechanical Hamiltonian becomes

$$\begin{aligned} H = \sum_{\mathbf{kQ}\sigma} \Psi^\dagger_{\mathbf{k}\sigma\mathbf{Q}}\, \hat{H}_{\mathbf{QQ}'}(\mathbf{k})\, \Psi_{\mathbf{k}\sigma\mathbf{Q}'} + \sum_{\mathbf{kQ}\boldsymbol{P}\sigma} \Psi^\dagger_{\mathbf{k}\sigma\mathbf{Q}}\Big(\boldsymbol{q}_{-\boldsymbol{P}}\cdot\boldsymbol{\tau}\,\delta\hat{H}_{\mathbf{QQ}'}(\boldsymbol{P})\Big)\Psi_{\mathbf{k}+\boldsymbol{P}\sigma\mathbf{Q}'} \\ + \frac{1}{2}\sum_{\boldsymbol{P}} \omega_{\boldsymbol{P}}\left(\mathbf{p}_{\boldsymbol{P}}\cdot\mathbf{p}_{-\boldsymbol{P}} + \mathbf{q}_{\boldsymbol{P}}\cdot\mathbf{q}_{-\boldsymbol{P}}\right), \end{aligned} \tag{4.41}$$

where $\delta\hat{H}_{\mathbf{QQ}'}(\boldsymbol{P})$ is the same as $\delta\hat{H}_{\mathbf{QQ}'}$ in Eq. (4.38) with $\boldsymbol{P}$-dependent constants $g_{\boldsymbol{P}}$, $g'_{\boldsymbol{P}}$, and $\gamma_{\boldsymbol{P}}$, invariant under the little group at $\boldsymbol{P}$. In this general case, the generator of $U_v(1)$ reads

$$J_z = \frac{1}{2}\sum_{\mathbf{kQ}\sigma} \Psi^\dagger_{\mathbf{k}\sigma\mathbf{Q}}\,\sigma_0\,\tau_z\,\Psi_{\mathbf{k}\sigma\mathbf{Q}} + \sum_{\boldsymbol{P}} \mathbf{q}_{\boldsymbol{P}}\wedge\mathbf{p}_{-\boldsymbol{P}}\,. \tag{4.42}$$

4.3.4 Frozen phonon band structure in the continuum model formalism

We perform a frozen phonon calculation with the continuum model formalism and benchmark it with the tight-binding calculation done in Section. 4.1.3. We neglect the phonon energy, last term in Eq. (4.37), and fix $\mathbf{q} = (q_1, q_2)$ to some constant value. Because of the $U_v(1)$ symmetry, what matters is just the modulus q of $\mathbf{q}$. In practice we have taken $\mathbf{q} = (1, 0)$, and studied the band structure varying the coupling constants g, setting $g' = g/10$ and $\gamma = g/2.5$, and assuming the following parameters: $\hbar v/a_0 = 2.1354\ eV$ [117]; $u = 0.0761\ eV$ and $u' = 0.1031\ eV$ [53]. This choice fits well the microscopic tight-binding calculations of Fig. 4.6. As shown in Fig. 4.14, as

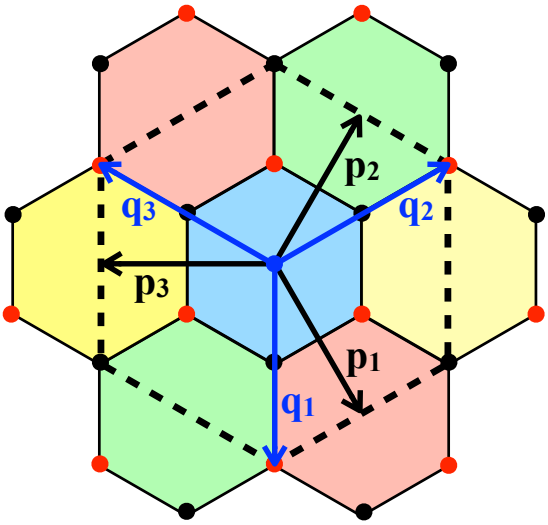

Figure 4.15: Reduced Brillouin zones with the multicomponent distortion at **M**, shown as coloured hexagons, while the four times larger hexagon drawn with a dashed line is the undistorted MBZ. The vectors $\mathbf{p}_i$, black arrows, and $\mathbf{q}_i$, blue arrow, for $i = 1, \ldots, 3$, are also shown. Note that $\mathbf{p}_1 = \boldsymbol{A}'$ and $\mathbf{p}_2 = \boldsymbol{B}'$ are also the reciprocal lattice vectors of the reduced Brillouin zone. The black and red circles are the positions of the sublattice vectors $\mathbf{Q}_A$ and $\mathbf{Q}_B$, respectively, defined in Eq. (4.48).

soon as the frozen phonon terms are turned on, all the degeneracies in the band structure arising due to the valley symmetry are lifted. This occur with a set of avoided crossings which move from $\mathbf{K} \to \mathbf{M}$ and from $\mathbf{K} \to \boldsymbol{\Gamma}$ (Fig.4.14b)). In particular, the crossings that move from $\mathbf{K} \to \mathbf{M}$ eventually meet at **M**, forming (six) Dirac nodes, which then move towards $\boldsymbol{\Gamma}$ (Fig. 4.14c)). Finally, at a threshold value of g, a gap opens at the charge neutrality point (Fig. 4.14d)). Such gap keeps increasing as the deformation amplitude increases.

4.3.5 Moiré phonons at M in the continuum model formalism

The phonon modes considered in the previous section were at position $\boldsymbol{\Gamma}$ of the MBZ, thus preserving the periodicity of the moiré superlattice. As pointed out before, these modes are able to open a gap in the band structure only at charge neutrality. Gap opening at different commensurate fillings requires freezing finite momentum phonons (see Section 4.1.5). Here, we consider the multicomponent distortion shown in Fig. 4.10 which involves the modes at the three inequivalent **M** points in the MBZ:

$$\mathbf{M}_1 = \frac{\boldsymbol{G}_1}{2}\,, \mathbf{M}_2 = \mathbf{C}_{3z}(\mathbf{M}_1) = \frac{\boldsymbol{G}_2}{2}\,, \mathbf{M}_3 = \mathbf{C}_{3z}(\mathbf{M}_2) = -\frac{\boldsymbol{G}_1 + \boldsymbol{G}_2}{2}\,. \tag{4.43}$$

Freezing a multiple distortion at all these points reduces by a quarter the Brillouin zone, see Fig. 4.15, which has now the reciprocal lattice vectors

$$\boldsymbol{A}' = \mathbf{M}_1\,, \boldsymbol{B}' = \mathbf{M}_2\,. \tag{4.44}$$

Since $\mathbf{M}_i$, $i = 1, 2, 3$, are small as compared to the vectors $\mathbf{Q}_{ij}$ introduced in the previous section, we can make the same assumption (4.40) that leads to the Hamiltonian (4.41), namely assume that the displacement induced by the multiple distortion has the same expression of Eq. (4.28), with the only difference that

$$e^{i\left(\mathbf{R}^{(a)}+\mathbf{r}_\alpha^{(a)}\right)\cdot\mathbf{Q}_{ij}} \longrightarrow \sum_{n=1}^{6} e^{i\left(\mathbf{R}^{(a)}+\mathbf{r}_\alpha^{(a)}\right)\cdot\left(\mathbf{Q}_{ij}+\mathbf{p}_n\right)} \tag{4.45}$$

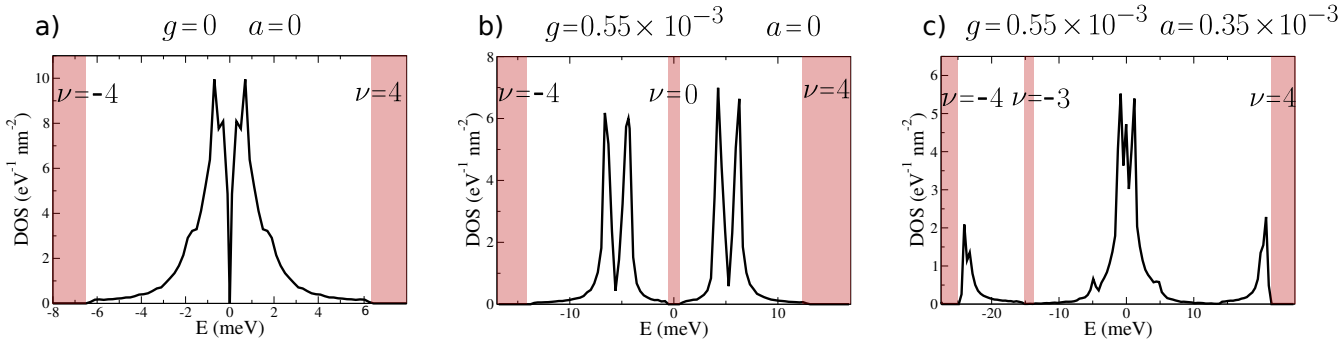

Figure 4.16: Density of states around charge neutrality obtained with the Hamiltonian (4.48) with $g' = g/10$, $\gamma = g/2.5$, $a' = a/10$ and $\alpha = a/2.5$. Gaps are highlighted in red, and the corresponding filling factor is ν. a) The undistorted lattice density of states. b) The density of states obtained by deforming the lattice with only the distortion at $\mathbf{\Gamma}$, which opens a gap at charge neutrality. c) Density of states obtained using both the Γ and the $\mathbf{M}$ multicomponent distortions. Here a gap opens at filling of 1 electron (3 holes with respect to neutrality) per unit cell.

where

$$\mathbf{p}_1 = -\mathbf{p}_4 = \boldsymbol{M}_1 = \boldsymbol{A}' \,, \quad \mathbf{p}_2 = -\mathbf{p}_5 = \boldsymbol{M}_2 = \boldsymbol{B}' \,, \quad \mathbf{p}_3 = -\mathbf{p}_6 = \boldsymbol{M}_3 = -\boldsymbol{A}' - \boldsymbol{B}' \tag{4.46}$$

are the additional long wavelength modulation vectors on top of the leading short wavelength ones at $\mathbf{Q}_{ij}$. The vectors $\mathbf{q}_i$ defined in Eq. (A.3) can be written in terms of the new reciprocal lattice vectors $\boldsymbol{A}'$ and $\boldsymbol{B}'$ as

$$\mathbf{q}_1 = \frac{2}{3}\,(\boldsymbol{A}' - \boldsymbol{B}'), \quad \mathbf{q}_2 = \frac{2}{3}\,(\boldsymbol{A}' + 2\boldsymbol{B}'), \quad \mathbf{q}_3 = \frac{2}{3}\,(-2\boldsymbol{A}' - \boldsymbol{B}')\,. \tag{4.47}$$

Both $\mathbf{p}_i$ and $\mathbf{q}_i$, $i = 1, 2, 3$, are shown in Fig. 4.15. Considering all momenta $\mathbf{k}$ within the new BZ, the light blue hexagon in Fig. 4.15, and assuming that, besides the multicomponent distortion at $\mathbf{M}$, there is still a distortion at $\mathbf{\Gamma}$, the Hamiltonian can be written again as a matrix $\hat{H}_{\mathbf{Q}\mathbf{Q}'}(\mathbf{k})$, which now reads

$$\begin{aligned}\hat{H}_{\mathbf{Q}\mathbf{Q}'}(\mathbf{k}) = \delta_{\mathbf{Q},\mathbf{Q}'}\; v\,\tau_z\big(\mathbf{k}-\mathbf{Q}\big)\cdot\boldsymbol{\sigma} + \tau_0 \sum_{i=1}^{3}\Big(\delta_{\mathbf{Q}'-\mathbf{Q},\mathbf{q}_i} + \delta_{\mathbf{Q}-\mathbf{Q}',\mathbf{q}_i}\Big)\,\hat{T}_i(u,u') + \gamma\,\delta_{\mathbf{Q},\mathbf{Q}'}\;\tau_x \\ + \tau_x \sum_{i=1}^{3}\Big(\delta_{\mathbf{Q}'-\mathbf{Q},\mathbf{q}_i} + \delta_{\mathbf{Q}-\mathbf{Q}',\mathbf{q}_i}\Big)\,\hat{T}_i(g,g') \;+ \alpha\,\tau_x \sum_{i=1}^{6}\Big(\delta_{\mathbf{Q}'-\mathbf{Q},\mathbf{p}_i} + \delta_{\mathbf{Q}-\mathbf{Q}',\mathbf{p}_i}\Big) \\ + \tau_x \sum_{i=1}^{3}\sum_{j=1}^{6}\Big(\delta_{\mathbf{Q}'-\mathbf{Q},\mathbf{q}_i+\mathbf{p}_j} + \delta_{\mathbf{Q}-\mathbf{Q}',\mathbf{q}_i+\mathbf{p}_j}\Big)\,\hat{T}_i(a,a')\,,\end{aligned}$$

where the matrices $\hat{T}_i(x,x')$ are those in Eq. (2.30), though they depend on different set of parameters, (u,u'), (g,g') and (a,a'). The crucial difference with respect to the Hamiltonian (4.38) with only the $\mathbf{\Gamma}$-distortion, is that the $\mathbf{Q}$ vectors span now the sites of the honeycomb lattice generated by the new fourfold-smaller Brillouin zone, hence they are defined through

$$\mathbf{Q} = \Big\{\mathbf{Q}'_A\,,\,\mathbf{Q}'_B\Big\} = \begin{cases}\mathbf{Q}'_A = \dfrac{\boldsymbol{A}'-\boldsymbol{B}'}{3} + n\boldsymbol{A}' + m\boldsymbol{B}'\,, \\ \mathbf{Q}'_B = -\dfrac{\boldsymbol{A}'-\boldsymbol{B}'}{3} + n\boldsymbol{A}' + m\boldsymbol{B}'\,,\end{cases} \tag{4.48}$$

and shown in Fig. 4.15 as black and red circles, respectively, and must not be confused with those in Eq. (A.2). In Fig. 4.16 we show the density of states around neutrality of the Hamiltonian

(4.48). The first two cases corresponds to undistorted and Γ-only distorted structures, while the third panel involves also the **M** multicomponent distortion. As can be seen, a gap now opens at the partial filling of 1 electron per unit cell. As it was shown in Section 4.1.5, other phonons or combinations of them can open gaps at any integer filling of the four electronic flat bands.

5

Γ-valley Transition metal dichalcogenide moiré bands

Transition metal dichalcogenides (TMDs) are an emerging class of two dimensional materials with features that make them attractive for applications and fundamental studies of novel physical phenomena. Unlike graphene, TMDs monolayers are binary compounds composed by two chalchogen (X) atoms per metal (M) site. Most TMDs exist in two structural phases characterized by either octahedral (1T) or trigonal prismatic (2H) coordination of metal atoms [5]. In this Chapter we focus on 2H group-VI TMDs, whose moiré heterostructures are currently under active investigation [40, 34, 35, 36, 37, 118, 119, 120].

In Section 5.1 we select those TMDs homobilayers in which the valence band maximum (VBM) is at the Brillouin zone center Γ. In these cases, the bilayer valence band maxima is a layer-antibonding state that is energetically separated with respect to its bonding counterpart by several hundreds of meV.

This observation motivates the construction in Section 5.2.1 of a one-band continuum model in which the antibonding state is not explicitly included, and which is similar at first sight to the one band Hamiltonian of K-valley heterobilayers [39]. We find however that as a consequence of the emergent D_6 symmetry described in Section 5.2.1, Γ-valley homobilayers simulate 2D honeycomb lattice physics, opening up a new chapter of strong correlation physics in moiré superlattices.

The parameters of the continuum model are tuned to match the DFT bandstructures of Section 5.2.2, that are performed directly at small angles with the inclusion of lattice relaxation. Then, in Section 5.2.3, we demonstrate the usefulness of the continuum model by using it to predict the bandstructure of twisted TMDs at angles where full microscopic calculations are prohibitive. By using the Topological Quantum Chemistry technique [121], we show that the first three set of bands is formed by Wannier orbitals sitting on honeycomb or kagome lattices. In Section 5.2.4 we discuss the symmetries and band centers evolution of the moiré bands in terms of Wannier orbitals transforming as harmonic oscillator eigenvalues.

5.1 Aligned bilayer bandstructure *vs.* Stacking

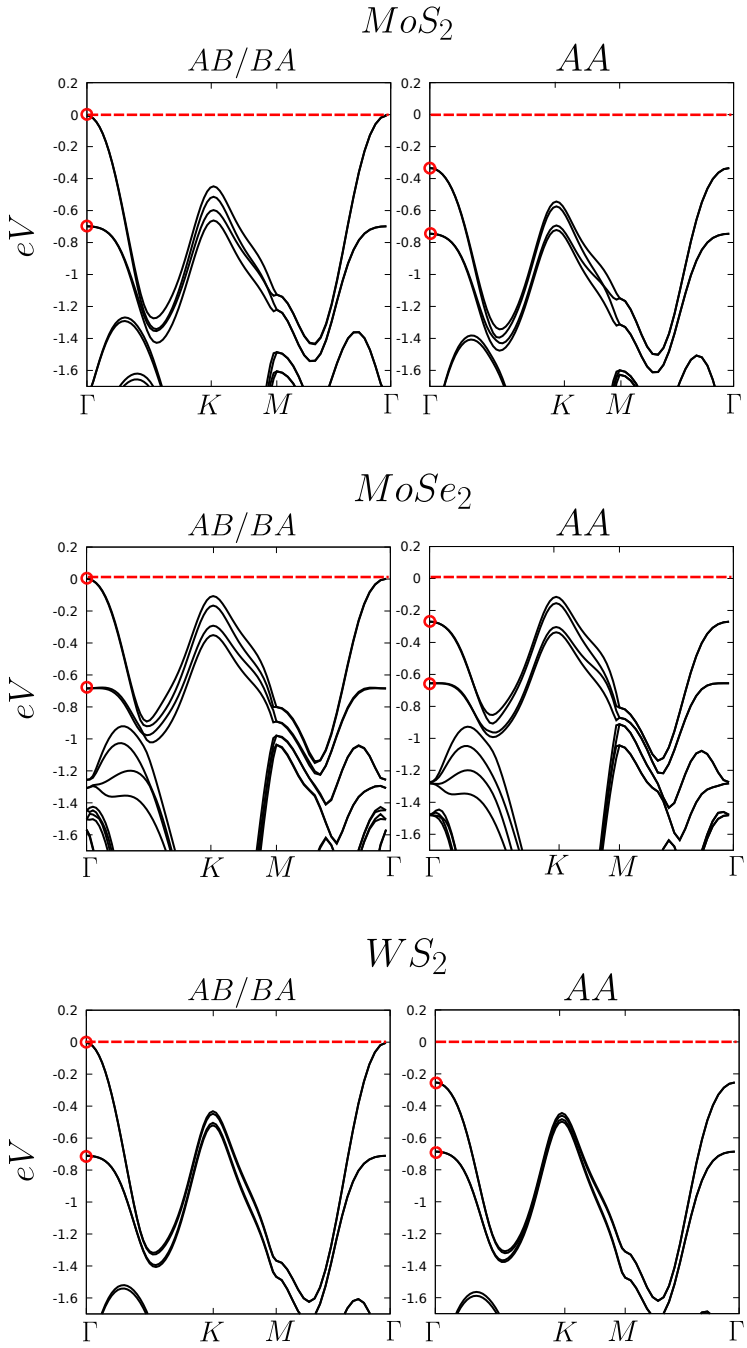

Figure 5.1: Bilayer DFT bandstructures for relaxed MoS_2, $MoSe_2$ and WS_2 with AA and AB/BA stacking. The VBM energy is denoted by a red dashed line while the layer bonding and antibonding valence states at Γ are denoted by red circles.

In bulk TMDs with 2H structure, the valence band maximum (VBM) is located at the Brillouin-zone center Γ point [5]. This property is a consequence of the valence band orbital character [122], which is dominated by metal d_{z^2}/chalcogen p_z antibonding orbitals whose out-of-plane orientation generates strong inter-layer hybridization that pushes band energies near the Γ-point up. The valence band maximum is at the two-dimensional Γ-point all the way from bulk to bilayer in WS_2, MoS_2 and $MoSe_2$, the materials on which we focus. We performed a systematic analysis of the stacking dependence of these untwisted bilayer electronic structures to identify

the valence band edges at two high-symmetry stacking (AA and AB/BA).
The calculations were performed with QUANTUM ESPRESSO [123, 124] using the Perdew-Burke-Ernzerhof (PBE) generalized gradient approximation (GGA) functional. The weak van-der-Waals (vdW) forces acting between the layers were taken into account by means of the non-local vdW functional vdW-DF2-C09 [125, 126], which has been shown to give good results over a broad range of layered materials [127, 128]. Spin orbit coupling (SOC) is included in these calculations. For all the elements considered except Tungsten (W) we used fully relativistic ultrasoft pseudopotentials from pslibrary.1.0.0 [129]; the Tungsten (W) pseudopotential was instead taken from the SG15-ONCV [130] library. The plane-wave basis used to sample the reciprocal space was selected with a kinetic energy cutoff of 55 Ry for the wave functions, while a 500 Ry cutoff energy was is used to represent the charge density. The BZ was sampled by an $20 \times 20 \times 1$ Monkhorst-Pack k-point grid. We initially relaxed the monolayer unit cells in order to determine the lattice parameters a_0. Then, we relaxed the bilayers geometry with a vacuum layer of 20 Å.
In Fig.5.1 we show the bandstructures of AA and AB/BA stacked MoS_2, $MoSe_2$ and WS_2. As can be seen, the VBM is always located at the $\mathbf{\Gamma}$ point. At this point, the orbital character is dominated by out-of-plane oriented metal d_z and chalcogen p_z orbitals, so that the VBM is strongly sensitive to the interlayer distance which is larger by ≈ 0.7Å in the AA stacking case. This leads to a $300 - 350$ meV $\mathbf{\Gamma}$ energy difference between the two configurations. In any case, the bilayer valence band maxima is a layer-antibonding state that is energetically separated with respect to its bonding counterpart by several hundreds of meV. This is emphasized by red circles in Fig 5.1. We checked their energy separation for bilayers with a generic relative stacking vector $\mathbf{d}$ taken on a 10x10 real space grid of the unit cell vectors. We found that the lowest energy separations occur for AA stacking, and that the separation is never lower than 350-400 meV, thus justifying our one-band model assumption of Section. 5.2.2.

5.2 Twisted Homobilayers

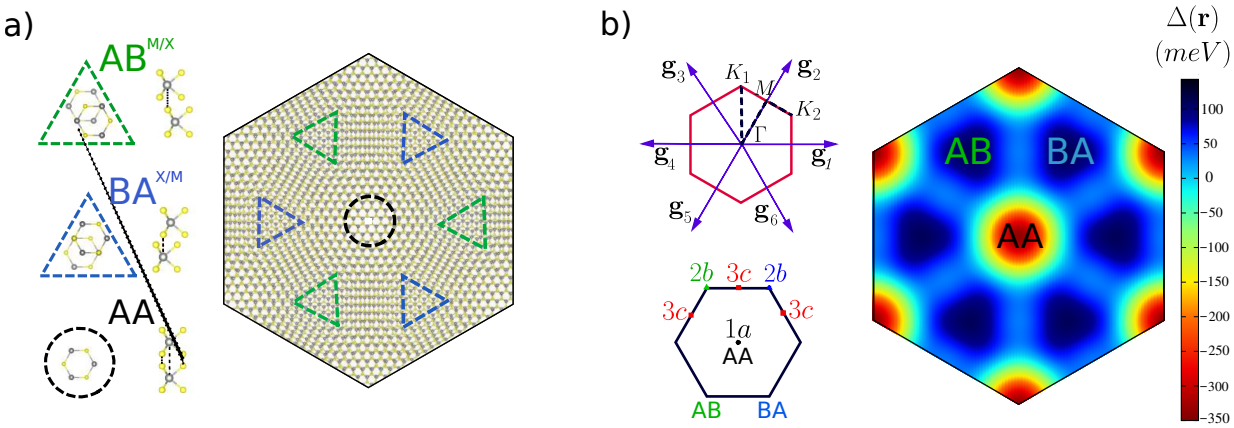

Figure 5.2: a) The three high symmetry configurations in β homobilayers: $BA^{X/M}$, $AB^{M/X}$ and AA. On the left, the moirè pattern formed in a $\theta = 3.15°$ homobilayer is illustrated. The Bernal stacked regions, whose centers form an honeycomb lattice are denoted by green and blue triangles, and the AA region by a black circle. b) The first shell ($s = 1$) of moirè reciprocal lattice vectors used to expand the moirè potential and the the maximal Wyckoff positions of wallpaper group 17. On the left we show the moirè potential $\Delta(\mathbf{r})$ for MoS_2, which is attractive for holes on the hexagonal network formed by the AB/BA regions.

Twisted heterostructures between binary van der Waals monolayers, like TMDs but unlike graphene, occur in two distinct configurations - referred to here as α and β [43] . The two configurations differ by a 180° rotation of the top layer with respect to the metal axis. In 5.2 (a) we show a β twisted bilayer in which AA regions form a triangular lattice and are surrounded by six Bernal ($AB^{M/X}$ and $BA^{X/M}$) regions that form a honeycomb network. In the $BA^{X/M}/AB^{M/X}$ areas a metal atom (M) on one layer is directly on top/below a chalcogen atom (X) on the other layer. The two regions are related by a reflection that exchanges the two layers. In α bilayers, on the other hand, the ($AB^{M/M}$ and $BA^{X/X}$) Bernal stacked regions are structurally and energetically different. In the following we will focus on β bilayers and we will omit the apex in the AB/BA labeling.

5.2.1 Emergent D_6 symmetry in the homobilayers moiré potential

We derive the valence band moiré Hamiltonian from first principles following the approach outlined in [131]. The main difference compared to the procedure adopted in previous works [39, 132] is that we obtain continuum model parameters directly from the *ab initio* electronic structure of fully relaxed twisted bilayers. In our low-energy model we retain only the anti-bonding state at $\mathbf{\Gamma}$, which, as shown in the previous Section, is energetically isolated from other bands by 350-800 meV because of interlayer hybridization. Neglecting spin-orbit coupling, which vanishes at the $\mathbf{\Gamma}$-point by Kramer's theorem, we obtain the following simple single band $k \cdot p$ Hamiltonian:

$$\mathscr{H} = -\frac{\hbar^2 k^2}{2m^*} + \Delta(\mathbf{d}), \tag{5.1}$$

where m^* is the effective mass and $\Delta(\mathbf{d})$ is the potential felt by holes at the valence band maximum as a function of the relative displacement $\mathbf{d}$ between the two aligned layers.
The two-dimensional lattice periodicity of the aligned bilayers implies that $\Delta(\mathbf{d})$ is a periodic function. Threefold rotations with respect to the z-axis (C_{3z}) require that $\Delta(\mathbf{d})$ is equal to $\Delta(C_{3z}\mathbf{d})$. Moreover, two bilayers stacked by $\mathbf{d}$ and $C_{2z}\mathbf{d} = -\mathbf{d}$ are mapped into each other by a $z \leftrightarrow -z$ mirror and hence have the same bandstructure. This property, which is peculiar to β homobilayers, further implies that $\Delta(\mathbf{d}) = \Delta(C_{2z}\mathbf{d})$, *i.e.* that $\Delta(\mathbf{d})$ is a six-fold symmetric function. As a consequence the moirè potential, and hence the Hamiltonian in (5.1), are D_6 symmetric objects. The extrema of this potential are either at $\mathbf{d} = 0$ (AA stacking) or at $\mathbf{d} = \pm(\mathbf{a}_1 + \mathbf{a}_2)/3$ (AB and BA stacking), where $\mathbf{a}_1 = a_0(1, 0)$ and $\mathbf{a}_2 = a_0(-1/2, \sqrt{3}/2)$ are the primitive lattice vectors of the monolayer.

5.2.2 Continuum model for twisted Homobilayers

Twisting by a small angle θ yields a local interlayer displacement $\mathbf{d} = \theta\hat{z} \times \mathbf{r}$. Replacing $\mathbf{d}$ in Eq. 5.1 with $\mathbf{r}$ then retains the potential's symmetries and magnifies positions to yield a moiré potential described by the following Fourier expansion:

$$\Delta(\mathbf{r}) = \sum_s \sum_{j=1}^{6} V_s \exp\left(i\mathbf{g}_j^s \cdot \mathbf{r} + \phi_s\right) \tag{5.2}$$

where $\mathbf{g}_{j+1}^s = C_{6z}\mathbf{g}_j^s$ is the s-th shell of six moiré $\mathbf{g}$ vectors ordered with increasing $|\mathbf{g}|$. The phase factors ϕ_s are constrained by the C_{6z} symmetry to be either 0 or π. We solve for the moiré Hamiltonian Bloch states by expanding in plane waves:

$$\langle \mathbf{k} + \mathbf{g}' | \mathscr{H} | \mathbf{k} + \mathbf{g} \rangle = -\delta_{\mathbf{g},\mathbf{g}'} \frac{\hbar^2 |\mathbf{k}+\mathbf{g}|^2}{2m^*} + \Delta(\mathbf{g} - \mathbf{g}'), \tag{5.3}$$

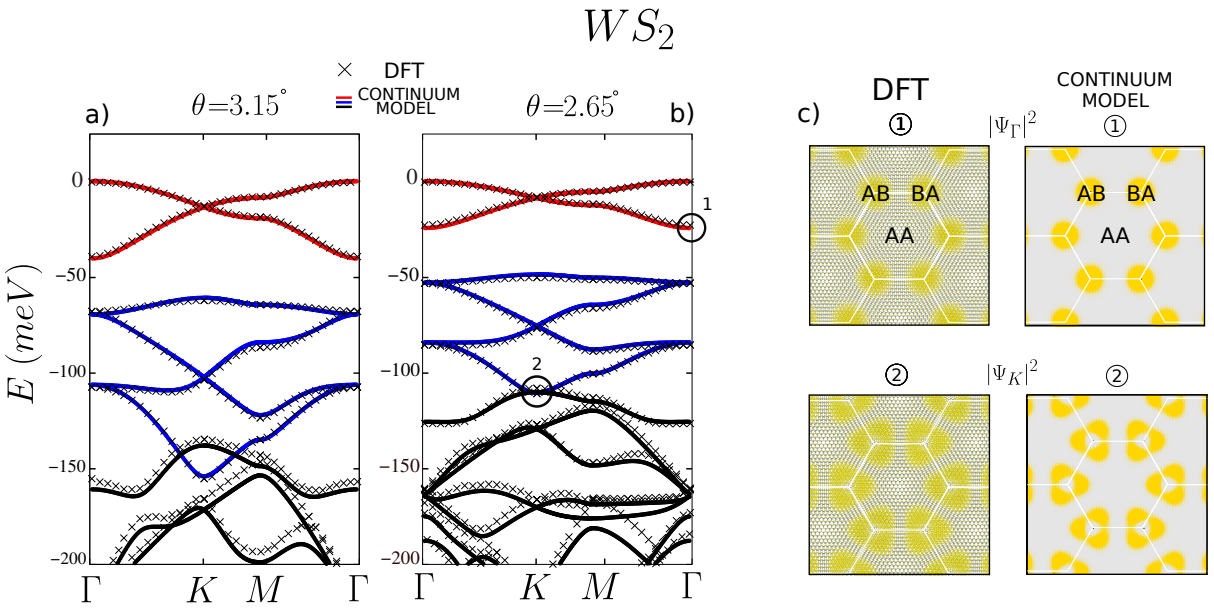

Figure 5.3: DFT vs continuum model. a,b) Twisted WS_2 bandstructure obtained with DFT (black crosses) and continuum model (colored lines) at two different twisting angles $\theta = 3.15°, 2.65°$. Similar plots for twisted MoS_2 and $MoSe_2$ can be found in 5.4. The valence band maximum is set to $E = 0$ and the bands originating from s and $p_x \pm ip_y$ moiré Wannier orbitals are colored in red and blue respectively. c) Charge density distributions of two selected Bloch states encircled in b) as obtained with DFT and with the continuum model.

where $\mathbf{k}$ is a wavevector in the moiré Brillouin-zone. The applicability of this low-energy model does not rely on commensurability between the moiré pattern and the underlying lattice. Even though the twisted lattice has only D_3 symmetry [132], the moiré Hamiltonian (5.3) inherits the D_6 symmetry of the moiré potential (5.2). This emergent low-energy property has profound consequences for the low energy moiré bands, and is the main focus of this paper. The emergence of symmetries not present in the underlying lattice is a common [10, 77] and intriguing feature of moirè materials.

	WS_2	MoS_2	$MoSe_2$
V_1	33.5	39.45	36.8
V_2	4.0	6.5	8.4
V_3	5.5	10.0	10.2
$\phi_{1,2,3}$	π	π	π
m^*	0.87	0.9	1.17
a_0	3.18	3.182	3.295

Table 5.1: Parameters of the moiré Hamiltonian (Eq. (5.3)) for the three TMD β-homobilayers considered in this paper. $V_{1,2,3}$ are in meV, m^* is in bare electron mass units, and the triangular lattice constant a_0 is in Angstroms.

We performed large scale ab-initio calculations on the relaxed $\theta = 2.65°, 3.15°$ twisted supercells. Due to the large volume of these supercells, containing more than 2800 atoms, these calculations required massive parallelization over more than 4000-5000 CPUs. Although most of the details of these calculations are similar to those described in the previous section, here we did not include SOC, whose effect vanishes at $\mathbf{\Gamma}$ (see Fig. 5.1) due to Kramer's theorem.

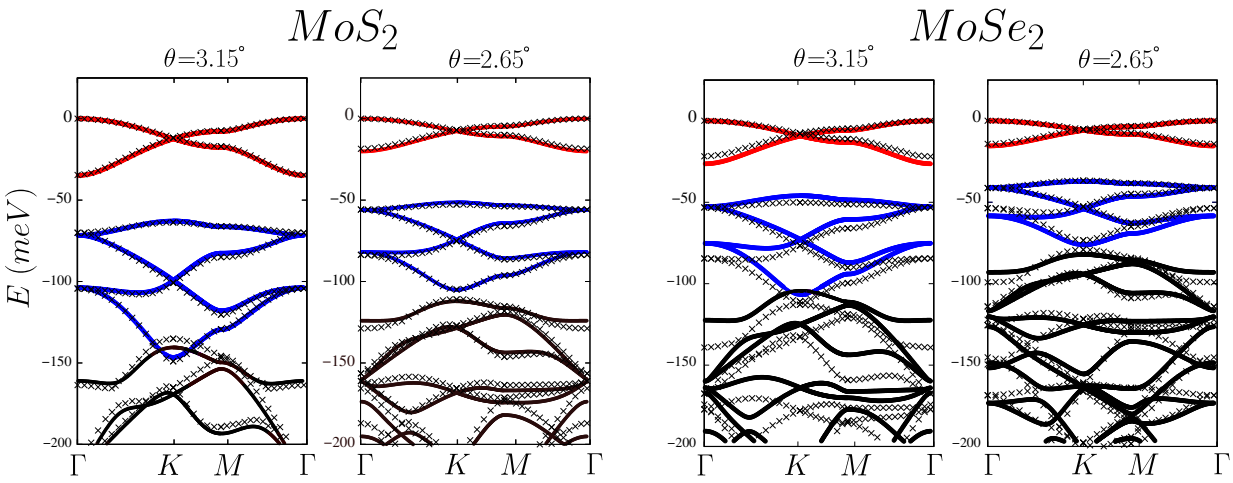

Figure 5.4: Twisted MoS_2 and $MoSe_2$ bandstructures obtained with DFT (black crosses) and continuum model (colored lines) at two different twist angles $\theta = 3.15°, 2.65°$. The valence band maximum is set to $E = 0$ and the bands originating from s and $p_x \pm ip_y$ moiré Wannier orbitals are colored in red and blue respectively

Instead we used scalar relativistic pseudopotentials from the SSSP efficiency library [133], which required lower plane wave and charge density kinetic energy cutoffs equal to 40 *Ry* and 320 *Ry* respectively. We sampled the BZ only at the **Γ** point. The atomic positions were optimized with the convergence criterion that all components of the forces acting on the atoms must be less than 10^{-3} Ry/bohr. The relaxation was performed along all the spatial directions in order to capture not only the interlayer corrugation but also the local in-plane strain patterns [120, 134, 135, 42]. The parameters (V_s, ϕ_s, m^*) of the continuum model were adjusted to match the DFT bandstructures.
As shown in Fig. 5.3 and 5.4, we found that expanding up to the third shell $s = 3$ was sufficient to accurately fit the low energy bandstructures and the charge density distribution of the relaxed bilayers. The model parameters for twisted WS_2, MoS_2 and $MoSe_2$ are listed in 5.1. As a consequence of the out-of-plane nature of the p_z and d_{z^2} orbitals involved at the **Γ** VBM the amplitude of the moirè potential V_s is more than five times larger than for K-valley TMDs [39, 132]. Furthermore, since the VBM in the Bernal stacked regions is higher in energy than in the AA regions (fixing $\phi_s = \pi$), the minimum of the potential felt by holes in the valence bands lies on the hexagonal lattice formed by the AB/BA regions (see Fig.5.2(b)). The physics of the moiré band edges in **Γ**-valley β TMDs homobilayers is therefore generated by orbitals sitting on a honeycomb lattice opening up a new chapter of strong correlation physics in moiré superlattices. Finally, the Hamiltonian presented here can be easily generalized to describe **Γ** α-homobilayers or heterobilayers by simply relaxing the ($\phi_s = 0, \pi$) constraint imposed by the emergent D_6 symmetry.

5.2.3 Twist angle dependence of the bandstructure

We now demonstrate the efficacy of the continuum model by using it to predict the bandstructure of twisted TMDs at angles where full microscopic calculations are prohibitive. To reveal the moiré band physics more fully we employ Topological Quantum Chemistry theory [121] to identify the symmetries and centers of the Wannier orbitals underlying the moiré bands by i) computing the symmetry of the Bloch states and classifying them in terms of the irreducible representations (irreps) of the little groups at the corresponding high symmetry points and ii) comparing the list of irreps with the Elementary Band Representatons (EBR) of the space group

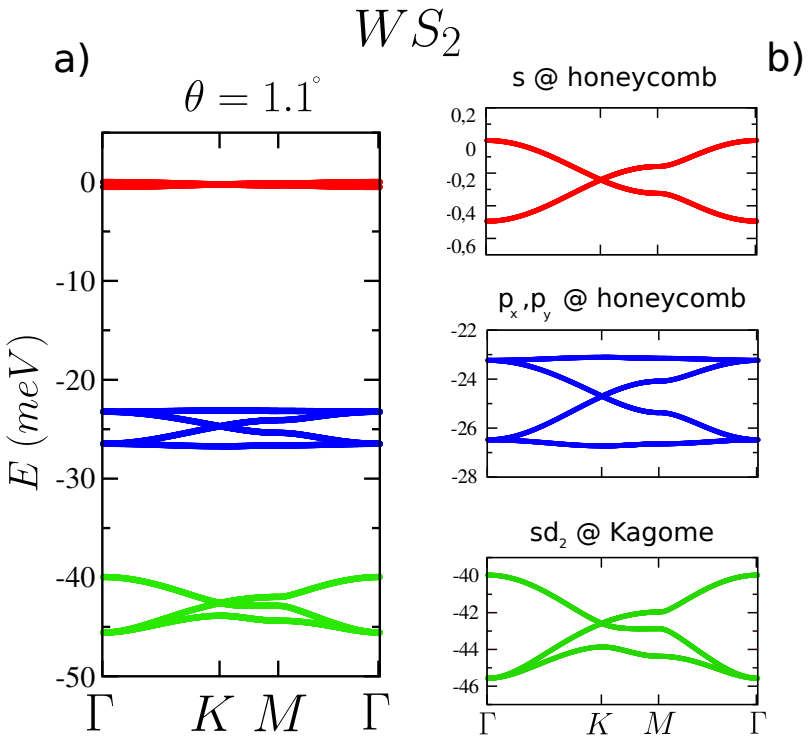

Figure 5.5: a) Bandstructure of $\theta = 1.1°$ twisted WS_2. b) The first set of bands has a bandwidth of ≈ 0.5 *meV* and is formed by s orbitals on an honeycomb lattice. The second is formed by $p_x \pm ip_y$ orbitals on the honeycomb and has a bandwidth of ≈ 3.2 *meV* . The third set of bands, formed by a set of hybridized sd_2 orbitals on a kagome lattice, has a bandwidth of ≈ 5.75 meV.

P6mm listed on the Bilbao Crystallographic server [136].
In Fig.5.5 the band structure of $\theta = 1.1°$ twisted WS_2 is shown. Consistent with the emergent honeycomb structure of the moirè potential, the first set of bands is formed by a pair of s-like orbitals centered in the AB/BA regions. These bands are non-degenerate at $\mathbf{\Gamma}$, form a Dirac node at K, and are topologically equivalent to the π bands of graphene. Consistent with previous studies on MoS_2 [42], the second set of bands, is instead formed by $p_x \pm ip_y$ orbitals on an honeycomb [137] that form a pair of almost dispersionless bands and also have a Dirac node at **K**. The third set of bands is even more intriguing, because it is formed by an odd (three) number of bands, a feature inconsistent with orbitals on an honeycomb. The symmetry analysis reveals that they are generated by orbitals centered on the $3c$ Wyckoff positions, which lie at the mid point between two honeycomb sites (see Fig.5.2 b). Interestingly, the lattice formed by this Wyckoff positions is a kagome lattice, a prominent platform to host frustration and spin liquid physics [138, 139]. The topology of these bands, which have one flat band and a Dirac node, further confirms the kagome picture. To understand these bands in terms of the hexagonal moirè potential of the system, we need two orbitals on different honeycomb sites to hybridize. As a consequence of this hybridization, the Wannier centers move from the honeycomb AB/BA sites (2b) to their midpoints (3c), effectively turning the honeycomb into a kagome lattice.

5.2.4 Twisted TMDs as coupled harmonic oscillators

We have performed a systematic analysis of all the bands within ≈ 110 meV below the VBM as a function of twist angle. This analysis is summarized in Fig. 5.6, where the band centers of the first five sets of bands bands are represented by colored circles whose saturation represents the corresponding bandwidths. The band centers and separations asymptotically evolve linearly

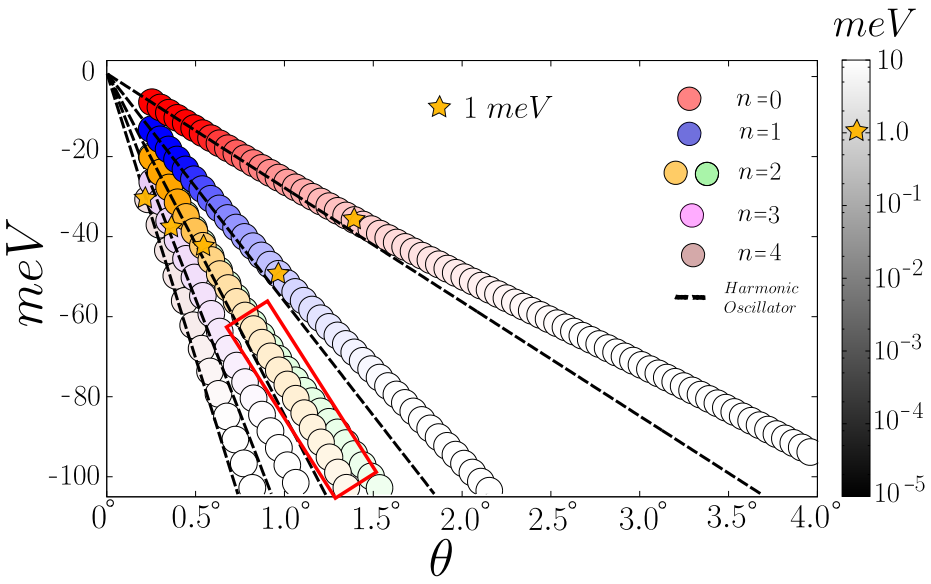

Figure 5.6: Band center of the five lowest energy bands in twisted MoS_2 as a function of twist angle. The bandwidth is encoded in color with the 1 meV bandwidth threshold marked by a star. The black dashed lines correspond to the $n = 0-4$ harmonic oscillator eigenvalues with an oscillator frequency that is proportional to twist angle. Within the red rectangle, the $n = 2$ levels split in two sets of kKagome bands (in green and orange) as a consequence of the sd_2 orbital hybridization.

with the inverse moirè length $a_M^{-1} \propto \theta$, whereas the bandwidths decrease exponentially with θ. This behaviour can be understood [39, 140] by making an harmonic approximation to the moiré potential near its maxima; $\Delta(\mathbf{r}) \approx -\gamma(\mathbf{r}/a_M)^2/2$ where $\gamma = 8\pi^2(V_1 + 6V_2 + 4V_3)$ for β-homobilayers.

The black dashed lines in Fig. 5.6 are the $n = 0-4$ eigenvalues of this harmonic oscillator problem. The good agreement identifies the harmonic oscillators wavefunctions as Wannier functions. Within this approximation, the ratio between the Wannier wavefunction size to the moiré period scales as $a_W/a_M \approx \theta^{1/2}$, implying that the overlap between neighboring Wannier functions and the bandwidths are $\propto e^{-\theta}$. The absence of magic angles in this systems is in sharp contrast with twisted bilayer graphene case [141, 142, 10, 75, 30].

The symmetries of the 2D harmonic oscillator wavefunctions further confirm this picture since the $n = 0$ orbital is an s state and the $n = 1$ doublet is spanned by $p_x \pm ip_y$. The $n = 3$ harmonic oscillator orbitals consist of one s and two d orbitals per honeycomb site. The EBR analysis shows that over a broad intermediate twist angles ($0.85° < \theta < 1.4°$) the six $n = 2$ orbitals per unit cell separate into two groups of three which can be identified as sd_2 bonding and antibonding bands centered on kagome lattice sites located half-way the honeycomb sites. This situation is known to give rise to kagome lattice physics [143], but has not been realized experimentally. The splitting between bonding and antibonding bands decreases with the angle until, at a critical $\theta_c \approx 0.85$, the six bands merge. By further decreasing the angle the bands disconnect again, this time forming sets of 2 and 4 bands separated by a small gap, whose dispersion resemble that of the s and $p_x \pm ip_y$ bands. We observed similar behaviour also in the $n = 3, 4$ sets of energy bands. This feature is due to high order terms not included in our simple harmonic oscillator approximation. In particular, the topology of these sub-bands is always that induced by orbitals (s or p) whose angular momenta is lower than two, consistent with the constraints imposed by a triangular quantum well [144]. We expect this behaviour to be even further enhanced by the strong reconstruction observed at very small angles, which tends to expand and sharpen the triangular Bernal domains [120].

6
Conclusions

This PhD thesis concerns our research activity in the rapidly growing field of moiré 2D materials. We initially focused on modeling the electronic and structural properties of twisted bilayer graphene. In this system, the slowly-varying local registry between the two layers along the moiré leads to a substantial lattice relaxation, which has been modeled by means of classical molecular dynamics with state-of-the-art force fields. In essence, relaxation acts as a torsion field winding around the AA regions in opposite directions for the two layers, with net effect of shrinking the AA regions, enlarging the more energetically favorable Bernal stacked regions, thus effectively forming triangular domains. In addition, the interlayer distance of the AA regions increases with respect to that of the Bernal zones, leading to significant out-of-plane buckling deformations.
The lattice relaxation has profound effects on the electronic bandstructure of the system that we computed by means of tight-binding and continuum model calculations. The microscopic tight-binding formalism has the advantage to rely on the real space atomic positions within the unit cell, thus being suitable to work with lattice deformations. However, the large number of atoms contained in the small-angle unit cell of twisted bilayer graphene makes any calculation more involved than that rather tough, if not computationally impossible. To cope with it, we introduced the continuum model formalism, which is much less computationally demanding. In both these formalisms, the set of extremely narrow bands of magic angle twisted bilayer graphene are isolated in energy by sizable band gaps only if lattice relaxation is included in the calculation.
Given the fact that the four flat bands are isolated in energy, it looks tempting to compute the corresponding Wannier orbitals, thus obtaining an effective four orbital model useful to perform many-body calculations. To do so, one has to figure out what are the symmetries of the problem, which is not straightforward as the exact point group of a twisted lattice depends on structural details not controllable in experiments, such as the twisting center or commensurability. Nevertheless, we showed that at small angles and low energy the system develops a set of emergent D_6 and $U(1)$ valley symmetries, which are robust to lattice relaxation and independent on the exact point group of the lattice. Then, we characterized the flat bands Bloch states in terms of these symmetries, showing that at least eight Wannier orbitals are necessary, but probably not sufficient, to describe the complex flat bands topology. This is reminiscent of the fact that these bands originate from an intricate set of avoided crossings

between energy levels around neutrality. As a consequence of such level repulsion, which is finely tuned by the twisting angle, a set of bands is compressed around neutrality, although they remain strongly entangled with the others. This mechanism is completely different from that in twisted TMDs or hBN, where there are no magic angles and the bandwidth continuously decreases with the twist angle. Although complicated, we built a minimal (number of orbitals) model for the flat bands, in which 8 Wannier orbitals per valley are introduced.
This 'broad band' origin of the flat bands together with the observed phenomenology of the insulating states of Refs. [8, 9], which turn metallic above a threshold Zeeman splitting or above a critical temperature, suggest that they might arise from a weak-coupling Stoner or CDW band instability driven by electron–electron and/or electron–phonon interactions, rather than from the Mott's localization phenomenon in presence of strong correlations.
We showed that twisted bilayer graphene supports an extremely large electron-phonon coupling that might be responsible for the observed insulating and superconducting states. In particular, we found that a pair of degenerate optical phonons couples strongly with the valley degrees of freedom, also doubly degenerate, realizing a so-called $E \otimes e$ Jahn-Teller coupling. The JT coupling lifts very efficiently all degeneracies which arise from the valley symmetry, and may lead, for an average atomic displacement as small as few mÅ, to large gaps (tens of meV) at most the integer fillings of the narrow bands. Some of these insulating states might posses non-trivial topology as testified by the odd winding of the Wilson loop. The phonons involved in this mechanism are a peculiarity of moiré materials, as their vibration is localized within the AA regions, with little or negligible atomic movement within the other regions of the moiré . Similar modes are routinely found in the entire phonon spectrum of the system (even in the acoustic region) and have been dubbed as 'moiré phonons'.
Justified by the large electron phonon coupling that we found, we worked out the possible superconducting state stabilized by these phonons. In a mean field BCS framework, the pairing instability occur in the spin-singlet Cooper channel, which may condense a superconducting order parameter in the extended s-wave and/or $d \pm id$-wave symmetry.
In the final part of this Thesis we focus on twisted Transition metal dichalchogenides bilayers. We derive a continuum model Hamiltonian for those homobilayers in which the valence band edge is located around the Brilluoin zone center, such as WS_2, MoS_2 and $MoSe_2$. Their continuum model is obtained by fitting large scale ab-initio calculations with the inclusion of lattice relaxation. Then, we apply the continuum model approach to derive the bandstructure of twisted TMDs at angles were fully microscopic calculations are prohibitive. Interestingly, also these systems develop an emergent D_6 symmetry, and effectively realize a honeycomb lattice physics.
By performing a symmetry analysis of the Bloch states, we show that in energetic order the first three bands realize i) a single-orbital model on a honeycomb lattice, ii) a two-orbital model on a honeycomb lattice, and iii) a single-orbital model on a kagome lattice. The lowest energy bands provides a convenient realization of artificial graphene, but with a fine-structure constant that can be tuned simply by varying twist angle. The second set of bands is formed by $p_x \pm ip_y$ orbitals on a honeycomb lattice, and is a promising candidate to study orbital and nematic order. Thanks to an sd_2 hybridization of honeycomb lattice orbitals, the third set of bands realizes a kagome lattice model and is expected to host spin-liquid physics. Since all models have bandwidths that can be adjusted simply by varying twist angles or by applying pressure, they provide an enticing platform to study the exotic properties of strongly correlation physics on the honeycomb and kagome lattices.

A

A more convenient continuum model representation

For the purposes of Section 4.3, it is actually more convenient to use the alternative representation of the Hamiltonian derived in Ref. [75].
We translate $\mathbf{K}'_{\phi} = -\mathbf{K}_2$ so that it falls on $\mathbf{K}_{-\phi} = \mathbf{K}_2$, and similarly $\mathbf{K}'_{-\phi} = -\mathbf{K}_1$ on $\mathbf{K}_{\phi} = \mathbf{K}_1$, see Fig. 2.1 (d). This implies that the diagonal parts of the Hamiltonian $\hat{H}^{(i)}_{\zeta}(\mathbf{k})$, where $i = 1, 2$ is the layer index and $\zeta = \pm 1$ the valley one, become simply

$$\begin{aligned}
\hat{H}^{(2)}_{+1}(\mathbf{k}) &= -v\left(\mathbf{k} - \mathbf{K}_2\right) \cdot \left(\sigma_x\,,\, \sigma_y\right), \\
\hat{H}^{(1)}_{-1}(\mathbf{k}) &= -v\left(\mathbf{k} - \mathbf{K}_2\right) \cdot \left(-\sigma_x\,,\, \sigma_y\right) = v\left(\mathbf{k} - \mathbf{K}_2\right) \cdot \boldsymbol{\sigma}^T\,, \\
\hat{H}^{(1)}_{+1}(\mathbf{k}) &= -v\left(\mathbf{k} - \mathbf{K}_1\right) \cdot \left(\sigma_x\,,\, \sigma_y\right), \\
\hat{H}^{(2)}_{-1}(\mathbf{k}) &= -v\left(\mathbf{k} - \mathbf{K}_1\right) \cdot \left(-\sigma_x\,,\, \sigma_y\right) = v\left(\mathbf{k} - \mathbf{K}_1\right) \cdot \boldsymbol{\sigma}^T\,.
\end{aligned} \tag{A.1}$$

Following Ref. [75], we define a set of vectors

$$\mathbf{Q} = \left\{\mathbf{Q}_A\,,\, \mathbf{Q}_B\right\} = \begin{cases} \mathbf{Q}_A = \mathbf{K}_2 + n\mathbf{G}_1 + m\mathbf{G}_2\,, \\ \mathbf{Q}_B = \mathbf{K}_1 + n\mathbf{G}_1 + m\mathbf{G}_2\,, \end{cases} \tag{A.2}$$

which span the vertices of the MBZs, where $\mathbf{Q}_A$, black circles in Fig. A.1, correspond to valley $\zeta = +1$ in layer 2 and valley $\zeta = -1$ in layer 1, while $\mathbf{Q}_B$, red circles in Fig. A.1, correspond to valley $\zeta = +1$ in layer 1 and valley $\zeta = -1$ in layer 2. In addition we define

$$\mathbf{q}_1 = \mathbf{K}_1 - \mathbf{K}_2\,, \mathbf{q}_2 = \mathbf{q}_1 + \mathbf{G}_2\,, \mathbf{q}_3 = \mathbf{q}_1 - \mathbf{G}_1\,. \tag{A.3}$$

Next, we redefine the momenta for layers 1 and 2 as, respectively,

$$\mathbf{p} - \mathbf{K}_2 \to \mathbf{k}' - \mathbf{Q}_B\,, \mathbf{k} - \mathbf{K}_1 \to \mathbf{k}' - \mathbf{Q}_A\,, \tag{A.4}$$

thus

$$\begin{aligned}
\mathbf{k} &= \mathbf{k}' + \mathbf{K}_1 - \mathbf{Q}_A\,, \\
\mathbf{p} &= \mathbf{k}' + \mathbf{K}_2 - \mathbf{Q}_B\,,
\end{aligned} \tag{A.5}$$

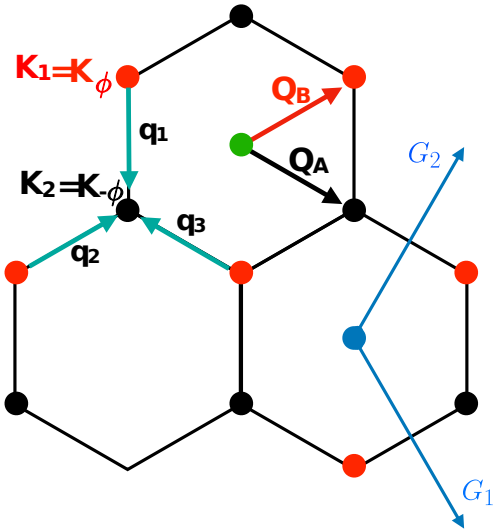

Figure A.1: The lattice in momentum space of Ref. [75]. The $\mathbf{Q}_A$ and $\mathbf{Q}_B$ vectors span the lattice formed by the $\mathbf{K}$ points of the two twisted monolayer Brillouin zones.

so that the selection rules transforms into

$$\begin{aligned}
&\mathbf{p} = \mathbf{k} \;\Rightarrow\; \mathbf{Q}_A - \mathbf{Q}_B = \mathbf{q}_1 \;\Rightarrow\; \mathbf{Q}_B = \mathbf{Q}_A - \mathbf{q}_1\,,\\
&\mathbf{p} = \mathbf{k} + \mathbf{G}_2 \;\Rightarrow\; \mathbf{Q}_A - \mathbf{Q}_B = \mathbf{q}_1 + \mathbf{G}_2 \;\Rightarrow\; \mathbf{Q}_B = \mathbf{Q}_A - \mathbf{q}_2\,,\\
&\mathbf{p} = \mathbf{k} - \mathbf{G}_1 \;\Rightarrow\; \mathbf{Q}_A - \mathbf{Q}_B = \mathbf{q}_1 - \mathbf{G}_1 \;\Rightarrow\; \mathbf{Q}_B = \mathbf{Q}_A - \mathbf{q}_3\,.
\end{aligned} \tag{A.6}$$

With those definitions, and denoting the conserved momentum $\mathbf{k}'$ as $\mathbf{k}$, the Hamiltonian of valley ζ now reads

$$\begin{aligned}
\hat{H}^{\zeta}_{\mathbf{Q}\mathbf{Q}'}(\mathbf{k}) = {}& \delta_{\mathbf{Q}\mathbf{Q}'}\, v\, \zeta\, (\mathbf{k} - \mathbf{Q}) \cdot (\sigma_x, \zeta\, \sigma_y)\\
&+ \sum_{i=1}^{3} \left(\delta_{\mathbf{Q}'-\mathbf{Q},\mathbf{q}_i} + \delta_{\mathbf{Q}-\mathbf{Q}',\mathbf{q}_i}\right) \hat{T}^{\zeta}_i(u,u')\,,
\end{aligned} \tag{A.7}$$

where

$$\begin{aligned}
\hat{T}^{\zeta}_1(u,u') &= u\,\sigma_0 + u'\,\sigma_x\,,\\
\hat{T}^{\zeta}_2(u,u') &= u\,\sigma_0 + u'\left(\cos\frac{2\pi}{3}\,\sigma_x + \zeta\,\sin\frac{2\pi}{3}\,\sigma_y\right),\\
\hat{T}^{\zeta}_3(u,u') &= u\,\sigma_0 + u'\left(\cos\frac{2\pi}{3}\,\sigma_x - \zeta\,\sin\frac{2\pi}{3}\,\sigma_y\right) = \sigma_x\,\hat{T}^{\zeta}_2(u,u')\,\sigma_x\,.
\end{aligned} \tag{A.8}$$

In particular,

$$\hat{T}^{-\zeta}_i(u,u') = \sigma_x\,\hat{T}^{\zeta}_i(u,u')\,\sigma_x\,. \tag{A.9}$$

One can further simplify the notation introducing the Pauli matrices τ_a, $a = 0, x, y, z$, with τ_0 the identity, that act in the valley subspace, and thus write

$$\begin{aligned}
\hat{H}_{\mathbf{Q}\mathbf{Q}'}(\mathbf{k}) = {}& \delta_{\mathbf{Q}\mathbf{Q}'}\, v\, \tau_z\, (\mathbf{k} - \mathbf{Q}) \cdot\; \Omega\,\boldsymbol{\sigma}\,\Omega\\
&+ \tau_0 \sum_{i=1}^{3} \left(\delta_{\mathbf{Q}'-\mathbf{Q},\mathbf{q}_i} + \delta_{\mathbf{Q}-\mathbf{Q}',\mathbf{q}_i}\right) \Omega\,\hat{T}_i(u,u')\,\Omega\,,
\end{aligned} \tag{A.10}$$

where $\hat{T}_i(u,u') \equiv \hat{T}_i^{+1}(u,u')$, and Ω is the real unitary operator

$$\Omega = \sigma_x \, \frac{1-\tau_z}{2} + \sigma_0 \, \frac{1+\tau_z}{2} = \sigma_x \, \mathrm{P}_{\zeta=-1} + \sigma_0 \, \mathrm{P}_{\zeta=+1} \ , \tag{A.11}$$

being P_ζ the projector onto valley ζ, which actually interchanges sublattice A with B in the valley $\zeta = -1$. Applying the unitary operator Ω we thus obtain

$$\begin{aligned} \Omega \, \hat{H}_{\mathbf{Q}\mathbf{Q}'}(\mathbf{k}) \, \Omega \to \hat{H}_{\mathbf{Q}\mathbf{Q}'}(\mathbf{k}) &= \delta_{\mathbf{Q}\mathbf{Q}'} \, v \, \tau_z \, (\mathbf{k}-\mathbf{Q}) \cdot \boldsymbol{\sigma} \\ &\quad + \tau_0 \sum_{i=1}^{3} \left(\delta_{\mathbf{Q}'-\mathbf{Q},\mathbf{q}_i} + \delta_{\mathbf{Q}-\mathbf{Q}',\mathbf{q}_i} \right) \hat{T}_i(u,u') \, , \end{aligned} \tag{A.12}$$

which has the advantage of having a very compact form.

Bibliography

[1] P. Ajayan, P. Kim, and K. Banerjee. Two-dimensional van der waals materials. *Physics Today*, 69:38, Sep 2016.

[2] Sheneve Z. Butler, Shawna M. Hollen, Linyou Cao, Yi Cui, Jay A. Gupta, Humberto R. Gutiérrez, Tony F. Heinz, Seung Sae Hong, Jiaxing Huang, Ariel F. Ismach, Ezekiel Johnston-Halperin, Masaru Kuno, Vladimir V. Plashnitsa, Richard D. Robinson, Rodney S. Ruoff, Sayeef Salahuddin, Jie Shan, Li Shi, Michael G. Spencer, Mauricio Terrones, Wolfgang Windl, and Joshua E. Goldberger. Progress, challenges, and opportunities in two-dimensional materials beyond graphene. *ACS Nano*, 7(4):2898–2926, Apr 2013.

[3] V. P. Gusynin and S. G. Sharapov. Unconventional integer quantum hall effect in graphene. *Phys. Rev. Lett.*, 95:146801, Sep 2005.

[4] Yuanbo Zhang, Yan-Wen Tan, Horst L. Stormer, and Philip Kim. Experimental observation of the quantum hall effect and berry's phase in graphene. *Nature*, 438(7065):201–204, Nov 2005.

[5] Sajedeh Manzeli, Dmitry Ovchinnikov, Diego Pasquier, Oleg V. Yazyev, and Andras Kis. 2d transition metal dichalcogenides. *Nature Reviews Materials*, 2(8):17033, Jun 2017.

[6] C. R. Dean, A. F. Young, I. Meric, C. Lee, L. Wang, S. Sorgenfrei, K. Watanabe, T. Taniguchi, P. Kim, K. L. Shepard, and J. Hone. Boron nitride substrates for high-quality graphene electronics. *Nature Nanotechnology*, 5(10):722–726, Oct 2010.

[7] K. S. Novoselov, A. Mishchenko, A. Carvalho, and A. H. Castro Neto. 2d materials and van der waals heterostructures. *Science*, 353(6298), Nov 2016.

[8] Yuan Cao, Valla Fatemi, Ahmet Demir, Shiang Fang, Spencer L. Tomarken, Jason Y. Luo, Javier D. Sanchez-Yamagishi, Kenji Watanabe, Takashi Taniguchi, Efthimios Kaxiras, Ray C. Ashoori, and Pablo Jarillo-Herrero. Correlated insulator behaviour at half-filling in magic-angle graphene superlattices. *Nature*, 556(7699): 1476–4697, Mar 2018.

[9] Yuan Cao, Valla Fatemi, Shiang Fang, Kenji Watanabe, Takashi Taniguchi, Efthimios Kaxiras, and Pablo Jarillo-Herrero. Unconventional superconductivity in magic-angle graphene superlattices. *Nature*, 556(7699): 43–50, Mar 2018.

[10] M. Angeli, D. Mandelli, A. Valli, A. Amaricci, M. Capone, E. Tosatti, and M. Fabrizio. Emergent D_6 symmetry in fully relaxed magic-angle twisted bilayer graphene. *Phys. Rev. B*, 98:235137, Dec 2018.

[11] Rafi Bistritzer and Allan H. MacDonald. Moiré bands in twisted double-layer graphene. *Proceedings of the National Academy of Sciences*, 108(30):12233–12237, Jul 2011.

[12] Y. Cao, J. Y. Luo, V. Fatemi, S. Fang, J. D. Sanchez-Yamagishi, K. Watanabe, T. Taniguchi, E. Kaxiras, and P. Jarillo-Herrero. Superlattice-induced insulating states and valley-protected orbits in twisted bilayer graphene. *Phys. Rev. Lett.*, 117:116804, Sep 2016.

[13] Patrick A. Lee, Naoto Nagaosa, and Xiao-Gang Wen. Doping a mott insulator: Physics of high-temperature superconductivity. *Rev. Mod. Phys.*, 78:17–85, Jan 2006.

[14] Xiaobo Lu, Petr Stepanov, Wei Yang, Ming Xie, Mohammed Ali Aamir, Ipsita Das, Carles Urgell, Kenji Watanabe, Takashi Taniguchi, Guangyu Zhang, Adrian Bachtold, Allan H. MacDonald, and Dmitri K. Efetov. Superconductors, Orbital Magnets, and Correlated States in Magic Angle Bilayer Graphene. *arXiv e-prints*, arXiv:1903.06513, Mar 2019.

[15] Matthew Yankowitz, Shaowen Chen, Hryhoriy Polshyn, Yuxuan Zhang, K. Watanabe, T. Taniguchi, David Graf, Andrea F. Young, and Cory R. Dean. Tuning superconductivity in twisted bilayer graphene. *Science*, 363(6431):1059–1064, Mar 2019.

[16] Alexander Kerelsky, Leo McGilly, Dante M. Kennes, Lede Xian, Matthew Yankowitz, Shaowen Chen, K. Watanabe, T. Taniguchi, James Hone, Cory Dean, Angel Rubio, and Abhay N. Pasupathy. Magic Angle Spectroscopy. *arXiv e-prints*, arXiv:1812.08776, Dec 2018.

[17] Youngjoon Choi, Jeannette Kemmer, Yang Peng, Alex Thomson, Harpreet Arora, Robert Polski, Yiran Zhang, Hechen Ren, Jason Alicea, Gil Refael, Felix von Oppen, Kenji Watanabe, Takashi Taniguchi, and Stevan Nadj-Perge. Imaging Electronic Correlations in Twisted Bilayer Graphene near the Magic Angle. *arXiv e-prints*, arXiv:1901.02997, Jan 2019.

[18] Yonglong Xie, Biao Lian, Berthold Jäck, Xiaomeng Liu, Cheng-Li Chiu, Kenji Watanabe, Takashi Taniguchi, B. Andrei Bernevig, and Ali Yazdani. Spectroscopic signatures of many-body correlations in magic-angle twisted bilayer graphene. *Nature*, 572(7767):101–105, Aug 2019.

[19] Aaron L. Sharpe, Eli J. Fox, Arthur W. Barnard, Joe Finney, Kenji Watanabe, Takashi Taniguchi, M. A. Kastner, and David Goldhaber-Gordon. Emergent ferromagnetism near three-quarters filling in twisted bilayer graphene. *arXiv e-prints*, arXiv:1901.03520, Jan 2019.

[20] Yuhang Jiang, Jinhai Mao, Xinyuan Lai, Kenji Watanabe, Takashi Taniguchi, Kristjan Haule, and Eva Y. Andrei. Evidence of charge-ordering and broken rotational symmetry in magic angle twisted bilayer graphene. *arXiv e-prints*, arXiv:1904.10153, Apr 2019.

[21] M. Serlin, C. L. Tschirhart, H. Polshyn, Y. Zhang, J. Zhu, K. Watanabe, T. Taniguchi, L. Balents, and A. F. Young. Intrinsic quantized anomalous hall effect in a moiré heterostructure. *Science*, 367(6480):900–903, 2020.

[22] Dillon Wong, Kevin P. Nuckolls, Myungchul Oh, Biao Lian, Yonglong Xie, Sangjun Jeon, Kenji Watanabe, Takashi Taniguchi, B. Andrei Bernevig, and Ali Yazdani. Cascade of electronic transitions in magic-angle twisted bilayer graphene. *Nature*, 582(7811):198–202, Jun 2020.

[23] H. Polshyn, M. Yankowitz, S. Chen, Y. Zhang, K. Watanabe, T. Taniguchi, C. R. Dean, and A. F. Young. Phonon scattering dominated electron transport in twisted bilayer graphene. *arXiv e-prints*, page arXiv:1902.00763, Feb 2019.

[24] Yuan Cao, Debanjan Chowdhury, Daniel Rodan-Legrain, Oriol Rubies-Bigorda, Kenji Watanabe, Takashi Taniguchi, T. Senthil, and Pablo Jarillo-Herrero. Strange metal in magic-angle graphene with near planckian dissipation. *Phys. Rev. Lett.*, 124:076801, Feb 2020.

[25] Fengcheng Wu, Euyheon Hwang, and Sankar Das Sarma. Phonon-induced giant linear-in-T resistivity in magic angle twisted bilayer graphene: Ordinary strangeness and exotic superconductivity. *arXiv e-prints*, arXiv:1811.04920, Nov 2018.

[26] Yu Saito, Jingyuan Ge, Kenji Watanabe, Takashi Taniguchi, and Andrea F. Young. Independent superconductors and correlated insulators in twisted bilayer graphene. *Nature Physics*, 1745-2481, Jun 2020.

[27] Petr Stepanov, Ipsita Das, Xiaobo Lu, Ali Fahimniya, Kenji Watanabe, Takashi Taniguchi, Frank H. L. Koppens, Johannes Lischner, Leonid Levitov, and Dmitri K. Efetov. Untying the insulating and superconducting orders in magic-angle graphene. *Nature*, 583(7816):375–378, Jul 2020.

[28] Fengcheng Wu, A. H. MacDonald, and Ivar Martin. Theory of phonon-mediated superconductivity in twisted bilayer graphene. *Phys. Rev. Lett.*, 121:257001, Dec 2018.

[29] Biao Lian, Zhijun Wang, and B. Andrei Bernevig. Twisted Bilayer Graphene: A Phonon Driven Superconductor. *arXiv e-prints*, arXiv:1807.04382, Jul 2018.

[30] M. Angeli, E. Tosatti, and M. Fabrizio. Valley jahn-teller effect in twisted bilayer graphene. *Phys. Rev. X*, 9:041010, Oct 2019.

[31] Kan-Ting Tsai, Xi Zhang, Ziyan Zhu, Yujie Luo, Stephen Carr, Mitchell Luskin, Efthimios Kaxiras, and Ke Wang. Correlated superconducting and insulating states in twisted trilayer graphene moire of moire superlattices, 2019. *arXiv e-prints*, arXiv:1912.03375, dec 2019

[32] Xiaomeng Liu, Zeyu Hao, Eslam Khalaf, Jong Yeon Lee, Yuval Ronen, Hyobin Yoo, Danial Haei Najafabadi, Kenji Watanabe, Takashi Taniguchi, Ashvin Vishwanath, and Philip Kim. Tunable spin-polarized correlated states in twisted double bilayer graphene. *Nature*, 583(7815):221–225, Jul 2020.

[33] Z. F. Wang, Zheng Liu, and Feng Liu. Quantum anomalous hall effect in 2d organic topological insulators. *Phys. Rev. Lett.*, 110:196801, May 2013.

[34] Kha Tran, Galan Moody, Fengcheng Wu, Xiaobo Lu, Junho Choi, Kyounghwan Kim, Amritesh Rai, Daniel A. Sanchez, Jiamin Quan, Akshay Singh, Jacob Embley, André Zepeda, Marshall Campbell, Travis Autry, Takashi Taniguchi, Kenji Watanabe, Nanshu Lu, Sanjay K. Banerjee, Kevin L. Silverman, Suenne Kim, Emanuel Tutuc, Li Yang, Allan H. MacDonald, and Xiaoqin Li. Evidence for moiré excitons in van der waals heterostructures. *Nature*, 567(7746):71–75, Mar 2019.

[35] Chenhao Jin, Emma C. Regan, Aiming Yan, M. Iqbal Bakti Utama, Danqing Wang, Sihan Zhao, Ying Qin, Sijie Yang, Zhiren Zheng, Shenyang Shi, Kenji Watanabe, Takashi Taniguchi, Sefaattin Tongay, Alex Zettl, and Feng Wang. Observation of moiré excitons in wse2/ws2 heterostructure superlattices. *Nature*, 567(7746):76–80, Mar 2019.

[36] Hongyi Yu, Gui-Bin Liu, Jianju Tang, Xiaodong Xu, and Wang Yao. Moiré excitons: From programmable quantum emitter arrays to spin-orbit–coupled artificial lattices. *Science Advances*, 3(11), 2017.

[37] Kyle L. Seyler, Pasqual Rivera, Hongyi Yu, Nathan P. Wilson, Essance L. Ray, David G. Mandrus, Jiaqiang Yan, Wang Yao, and Xiaodong Xu. Signatures of moiré-trapped valley excitons in mose2/wse2 heterobilayers. *Nature*, 567(7746):66–70, Mar 2019.

[38] Fengcheng Wu, Timothy Lovorn, and A. H. MacDonald. Topological exciton bands in moiré heterojunctions. *Phys. Rev. Lett.*, 118:147401, Apr 2017.

[39] Fengcheng Wu, Timothy Lovorn, Emanuel Tutuc, and A. H. MacDonald. Hubbard model physics in transition metal dichalcogenide moiré bands. *Phys. Rev. Lett.*, 121:026402, Jul 2018.

[40] Lei Wang, En-Min Shih, Augusto Ghiotto, Lede Xian, Daniel A. Rhodes, Cheng Tan, Martin Claassen, Dante M. Kennes, Yusong Bai, Bumho Kim, Kenji Watanabe, Takashi Taniguchi, Xiaoyang Zhu, James Hone, Angel Rubio, Abhay Pasupathy, and Cory R. Dean. Magic continuum in twisted bilayer WSe2 *arXiv e-prints*, arXiv:1910.12147, Oct 2019.

[41] Mit H. Naik, Sudipta Kundu, Indrajit Maity, and Manish Jain. Origin and evolution of ultraflatbands in twisted bilayer transition metal dichalcogenides: Realization of triangular quantum dot array *Phys. Rev. B*, 102:075413, Aug 2020.

[42] Lede Xian, Martin Claassen, Dominik Kiese, Michael M. Scherer, Simon Trebst, Dante M. Kennes, and Angel Rubio. Realization of nearly dispersionless bands with strong orbital anisotropy from destructive interference in twisted bilayer mos2 *arXiv e-prints*, arXiv:2004.02964, Apr 2020.

[43] Lede Xian, Dante M. Kennes, Nicolas Tancogne-Dejean, Massimo Altarelli, and Angel Rubio. Multiflat bands and strong correlations in twisted bilayer boron nitride: Doping-induced correlated insulator and superconductor. *Nano Letters*, 19(8):4934–4940, 2019. PMID: 31260633.

[44] D. M. Kennes, L. Xian, M. Claassen, and A. Rubio. One-dimensional flat bands in twisted bilayer germanium selenide. *Nature Communications*, 11(1):1124, Feb 2020.

[45] Jacob Brooks, Guorong Weng, Stephanie Taylor, and Vojtech Vlcek. Stochastic many-body perturbation theory for moiré states in twisted bilayer phosphorene. *Journal of Physics: Condensed Matter*, 32(23):234001, mar 2020.

[46] J. M. B. Lopes dos Santos, N. M. R. Peres, and A. H. Castro Neto. Graphene bilayer with a twist: Electronic structure. *Phys. Rev. Lett.*, 99:256802, Dec 2007.

[47] Kazuyuki Uchida, Shinnosuke Furuya, Jun-Ichi Iwata, and Atsushi Oshiyama. Atomic corrugation and electron localization due to moiré patterns in twisted bilayer graphenes. *Phys. Rev. B*, 90:155451, Oct 2014.

[48] Kuan Zhang and Ellad B. Tadmor. Structural and electron diffraction scaling of twisted graphene bilayers. *Journal of the Mechanics and Physics of Solids*, 112:225 – 238, 2018.

[49] Shuyang Dai, Yang Xiang, and David J. Srolovitz. Twisted bilayer graphene: Moiré with a twist. *Nano Letters*, 16(9):5923–5927, 2016. PMID: 27533089.

[50] Nguyen N. T. Nam and Mikito Koshino. Lattice relaxation and energy band modulation in twisted bilayer graphene. *Phys. Rev. B*, 96:075311, Aug 2017.

[51] Sandeep K Jain, Vladimir Juričić, and Gerard T Barkema. Structure of twisted and buckled bilayer graphene. *2D Materials*, 4(1):015018, 2017.

[52] Fernando Gargiulo and Oleg V Yazyev. Structural and electronic transformation in low-angle twisted bilayer graphene. *2D Materials*, 5(1):015019, 2018.

[53] Procolo Lucignano, Dario Alfè, Vittorio Cataudella, Domenico Ninno, and Giovanni Cantele. The crucial role of atomic corrugation on the flat bands and energy gaps of twisted bilayer graphene at the "magic angle" $\theta \sim 1.08$. *Phys. Rev B*, 99:195419, May 2019.

[54] G. Cantele, D. Alfè, F. Conte, V. Cataudella, D. Ninno, and P. Lucignano. Structural relaxation and low energy properties of twisted bilayer graphene *arXiv e-prints*, arXiv:2004.02964, Apr 2020.

[55] H. Yoo, K. Zhang, R. Engelke, P. Cazeaux, S. H. Sung, R. Hovden, A. W. Tsen, T. Taniguchi, K. Watanabe, G.-C. Yi, M. Kim, M. Luskin, E. B. Tadmor, and P. Kim. Atomic reconstruction at van der Waals interface in twisted bilayer graphene. *Nature Materials*, 18 448-453, April 2019.

[56] Donald W Brenner, Olga A Shenderova, Judith A Harrison, Steven J Stuart, Boris Ni, and Susan B Sinnott. A second-generation reactive empirical bond order (rebo) potential energy expression for hydrocarbons. *Journal of Physics: Condensed Matter*, 14(4):783, 2002.

[57] Aleksey N. Kolmogorov and Vincent H. Crespi. Registry-dependent interlayer potential for graphitic systems. *Phys. Rev. B*, 71:235415, Jun 2005.

[58] Wengen Ouyang, Davide Mandelli, Michael Urbakh, and Oded Hod. Nanoserpents: Graphene nanoribbon motion on two-dimensional hexagonal materials. *Nano Letters*, 18(9):6009–6016, 2018. PMID: 30109806.

[59] Erik Bitzek, Pekka Koskinen, Franz Gähler, Michael Moseler, and Peter Gumbsch. Structural relaxation made simple. *Phys. Rev. Lett.*, 97:170201, Oct 2006.

[60] J. C. Slater and G. F. Koster. Simplified lcao method for the periodic potential problem. *Phys. Rev.*, 94:1498–1524, Jun 1954.

[61] G. Trambly de Laissardiére, D. Mayou, and L. Magaud. Localization of dirac electrons in rotated graphene bilayers. *Nano Letters*, 10(3):804–808, 2010. PMID: 20121163.

[62] Yuan Cao, Debanjan Chowdhury, Daniel Rodan-Legrain, Oriol Rubies-Bigordà, Kenji Watanabe, Takashi Taniguchi, T. Senthil, and Pablo Jarillo-Herrero. Strange metal in magic-angle graphene with near Planckian dissipation. *arXiv e-prints*, arXiv:1901.03710, Jan 2019.

[63] S. L. Tomarken, Y. Cao, A. Demir, K. Watanabe, T. Taniguchi, P. Jarillo-Herrero, and R. C. Ashoori. Electronic compressibility of magic angle graphene superlattices. *arXiv e-prints*, arXiv:1903.10492, Mar 2019.

[64] Stephen Carr, Daniel Massatt, Steven B. Torrisi, Paul Cazeaux, Mitchell Luskin, and Efthimios Kaxiras. Relaxation and domain formation in incommensurate two-dimensional heterostructures. *Phys. Rev. B*, 98:224102, Dec 2018.

[65] Shang Liu, Eslam Khalaf, Jong Yeon Lee, and Ashvin Vishwanath. Nematic topological semimetal and insulator in magic angle bilayer graphene at charge neutrality *arXiv e-prints*, arXiv:1905.07409, May 2019.

[66] Ming Xie and A. H. MacDonald. Nature of the correlated insulator states in twisted bilayer graphene. *Phys. Rev. Lett.*, 124:097601, Mar 2020.

[67] Tommaso Cea and Francisco Guinea. Band structure and insulating states driven by the coulomb interaction in twisted bilayer graphene *Phys. Rev. B*, 102:045107, Jul 2020.

[68] Yi Zhang, Kun Jiang, Ziqiang Wang, and Fuchun Zhang. Correlated insulating phases of twisted bilayer graphene at commensurate filling fractions: a hartree-fock study, 2020. *Phys. Rev. B*, 102:035136, Jul 2020.

[69] Hoi Chun Po, Liujun Zou, Ashvin Vishwanath, and T. Senthil. Origin of mott insulating behavior and superconductivity in twisted bilayer graphene. *Phys. Rev. X*, 8:031089, Sep 2018.

[70] Stephen Carr, Shiang Fang, Ziyan Zhu, and Efthimios Kaxiras. Exact continuum model for low-energy electronic states of twisted bilayer graphene. *Phys. Rev. Research*, 1:013001, Aug 2019.

[71] J. Kang and O. Vafek. Symmetry, maximally localized Wannier states, and low energy model for the twisted bilayer graphene narrow bands. *Phys. Rev. X*, 8.031088, Sep 2018.

[72] M. Koshino, N. F. Q. Yuan, T. Koretsune, M. Ochi, K. Kuroki, and L. Fu. Maximally-localized Wannier orbitals and the extended Hubbard model for the twisted bilayer graphene. *Phys. Rev. X*, 8.031087, Sep 2018.

[73] Noah F. Q. Yuan and Liang Fu. Model for the metal-insulator transition in graphene superlattices and beyond. *Phys. Rev. B*, 98:045103, Jul 2018.

[74] Liujun Zou, Hoi Chun Po, Ashvin Vishwanath, and T. Senthil. Band structure of twisted bilayer graphene: Emergent symmetries, commensurate approximants, and wannier obstructions. *Phys. Rev. B*, 98:085435, Aug 2018.

[75] Zhida Song, Zhijun Wang, Wujun Shi, Gang Li, Chen Fang, and B. Andrei Bernevig. All magic angles in twisted bilayer graphene are topological. *Phys. Rev. Lett.*, 123:036401, Jul 2019.

[76] H. C. Po, L. Zou, T. Senthil, and A. Vishwanath. Faithful Tight-binding Models and Fragile Topology of Magic-angle Bilayer Graphene. *ArXiv e-prints*, August 2018.

[77] Liujun Zou, Hoi Chun Po, Ashvin Vishwanath, and T. Senthil. Band structure of twisted bilayer graphene: Emergent symmetries, commensurate approximants, and wannier obstructions. *Phys. Rev. B*, 98:085435, Aug 2018.

[78] L. Rademaker and P. Mellado. Charge-transfer insulation in twisted bilayer graphene. *Phys. Rev. B*, 98:235158, Dec 2018.

[79] Hoi Chun Po, Haruki Watanabe, and Ashvin Vishwanath. Fragile topology and wannier obstructions. *Phys. Rev. Lett.*, 121:126402, Sep 2018.

[80] Jianpeng Liu, Junwei Liu, and Xi Dai. The pseudo-Landau-level representation of twisted bilayer graphene: band topology and the implications on the correlated insulating phase. *arXiv e-prints*, arXiv:1810.03103, Oct 2018.

[81] Hoi Chun Po, Haruki Watanabe, and Ashvin Vishwanath. Fragile topology and wannier obstructions. *Phys. Rev. Lett.*, 121:126402, Sep 2018.

[82] Jian Kang and Oskar Vafek. Strong coupling phases of partially filled twisted bilayer graphene narrow bands. *arXiv e-prints*, page arXiv:1810.08642, Oct 2018.

[83] T. O. Wehling, E. Şaşıoğlu, C. Friedrich, A. I. Lichtenstein, M. I. Katsnelson, and S. Blügel. Strength of effective coulomb interactions in graphene and graphite. *Phys. Rev. Lett.*, 106:236805, Jun 2011.

[84] Ming Xie and Allan H. MacDonald. On the nature of the correlated insulator states in twisted bilayer graphene. *arXiv e-prints*, arXiv:1812.04213, Dec 2018.

[85] Yi-Zhuang You and Ashvin Vishwanath. Superconductivity from Valley Fluctuations and Approximate SO(4) Symmetry in a Weak Coupling Theory of Twisted Bilayer Graphene. *arXiv e-prints*, arXiv:1805.06867, May 2018.

[86] I. Yudhistira, N. Chakraborty, G. Sharma, D. Y. H. Ho, E. Laksono, O. P. Sushkov, G. Vignale, and S. Adam. Gauge phonon dominated resistivity in twisted bilayer graphene near magic angle. *arXiv e-prints*, arXiv:1902.01405, Feb 2019.

[87] R. Englman. *The Jahn-Teller Effect in Molecules and Crystals*. Interscience Monographs and Texts in Physics and Astronomy. Wiley-Interscience, 1972.

[88] Ado Jorio, Luiz Gustavo Cançado, and Leandro M. Malard. *Vibrations in Graphene*, page 71–89. Cambridge University Press, 2017.

[89] Emmanuel Koukaras, George Kalosakas, Costas Galiotis, and Konstantinos Papagelis. Phonon properties of graphene derived from molecular dynamics simulations. *Scientific Reports*, 5:12923, Aug 2015.

[90] Denis L. Nika and Alexander A. Balandin. Two-dimensional phonon transport in graphene. *Journal of Physics Condensed Matter*, 24:233203, Jun 2012.

[91] D. M. Basko and I. L. Aleiner. Interplay of coulomb and electron-phonon interactions in graphene. *Phys. Rev. B*, 77:041409, Jan 2008.

[92] Y. W. Choi and H. J. Choi. Electron-phonon interaction in magic-angle twisted bilayer graphene. *Phys. Rev. B*, 98:241412, Dec 2018.

[93] Alexandr I. Cocemasov, Denis L. Nika, and Alexander A. Balandin. Phonons in twisted bilayer graphene. *Phys. Rev. B*, 88:035428, Jul 2013.

[94] Andreij C. Gadelha, Douglas A. A. Ohlberg, Cassiano Rabelo, Eliel G. S. Neto, Thiago L. Vasconcelos, João L. Campos, Jessica S. Lemos, Vinícius Ornelas, Daniel Miranda, Rafael Nadas, Fabiano C. Santana, Kenji Watanabe, Takashi Taniguchi, Benoit van Troeye, Michael Lamparski, Vincent Meunier, Viet-Hung Nguyen, Dawid Paszko, Jean-Christophe Charlier, Leonardo C. Campos, Luiz G. Cançado, Gilberto Medeiros-Ribeiro, and Ado Jorio. Lattice dynamics localization in low-angle twisted bilayer graphene *arXiv e-prints*, arXiv:2006.09482, Jun 2020.

[95] Shang Liu, Eslam Khalaf, Jong Yeon Lee, and Ashvin Vishwanath. Nematic topological semimetal and insulator in magic angle bilayer graphene at charge neutrality. *arXiv e-prints*, arXiv:1905.07409, May 2019.

[96] Michele Fabrizio, Marco Airoldi, and Erio Tosatti. Interplay of orbital degeneracy and superconductivity in a molecular conductor. *Phys. Rev. B*, 53:12086–12093, May 1996.

[97] Michele Fabrizio and Erio Tosatti. Nonmagnetic molecular jahn-teller mott insulators. *Phys. Rev. B*, 55:13465–13472, May 1997.

[98] Massimo Capone, Michele Fabrizio, Claudio Castellani, and Erio Tosatti. Strongly correlated superconductivity and pseudogap phase near a multiband mott insulator. *Phys. Rev. Lett.*, 93:047001, Jul 2004.

[99] Cenke Xu and Leon Balents. Topological superconductivity in twisted multilayer graphene. *Phys. Rev. Lett.*, 121:087001, Aug 2018.

[100] Ganapathy Baskaran. Theory of Emergent Josephson Lattice in Neutral Twisted Bilayer Graphene (Moi\'re is Different). *arXiv e-prints*, arXiv:1804.00627, Apr 2018.

[101] J. F. Dodaro, S. A. Kivelson, Y. Schattner, X. Q. Sun, and C. Wang. Phases of a phenomenological model of twisted bilayer graphene. *Physical Review B*, 98:075154, Aug 2018.

[102] Hiroki Isobe, Noah F. Q. Yuan, and Liang Fu. Unconventional superconductivity and density waves in twisted bilayer graphene. *Phys. Rev. X*, 8:041041, Dec 2018.

[103] Dante M. Kennes, Johannes Lischner, and Christoph Karrasch. Strong correlations and d +id superconductivity in twisted bilayer graphene. *Physical Review B*, 98:241407, Dec 2018.

[104] Ya-Hui Zhang, Dan Mao, Yuan Cao, Pablo Jarillo-Herrero, and T. Senthil. Nearly flat Chern bands in moiré superlattices. *Physical Review B*, 99:075127, Feb 2019.

[105] M. Fidrysiak, M. Zegrodnik, and J. Spałek. Unconventional topological superconductivity and phase diagram for an effective two-orbital model as applied to twisted bilayer graphene. *Phys. Rev. B*, 98:085436, Aug 2018.

[106] Evan Laksono, Jia Ning Leaw, Alexander Reaves, Manraaj Singh, Xinyun Wang, Shaffique Adam, and Xingyu Gu. Singlet superconductivity enhanced by charge order in nested twisted bilayer graphene Fermi surfaces. *Solid State Communications*, 282:38–44, Oct 2018.

[107] Ying Su and Shi-Zeng Lin. Pairing symmetry and spontaneous vortex-antivortex lattice in superconducting twisted-bilayer graphene: Bogoliubov-de Gennes approach. *Physical Review B*, 98:195101, Nov 2018.

[108] Xingyu Gu, Chuan Chen, Jia Ning Leaw, Evan Laksono, Vitor M. Pereira, Giovanni Vignale, and Shaffique Adam. Antiferromagnetism and chiral d-wave superconductivity from an effective $t-J-D$ model for twisted bilayer graphene. *arXiv e-prints*, arXiv:1902.00029, Jan 2019.

[109] J. González and T. Stauber. Kohn-luttinger superconductivity in twisted bilayer graphene. *Phys. Rev. Lett.*, 122:026801, Jan 2019.

[110] J. González and T. Stauber. Marginal Fermi liquid in twisted bilayer graphene. *arXiv e-prints*, arXiv:1903.01376, Mar 2019.

[111] Bitan Roy and Vladimir Juričić. Unconventional superconductivity in nearly flat bands in twisted bilayer graphene. *Phys. Rev. B*, 99:121407, Mar 2019.

[112] Laura Classen, Carsten Honerkamp, and Michael M. Scherer. Competing phases of interacting electrons on triangular lattices in moir\'e heterostructures. *arXiv e-prints*, arXiv:1902.05350, Feb 2019.

[113] Huaiming Guo, Xingchuan Zhu, Shiping Feng, and Richard T. Scalettar. Pairing symmetry of interacting fermions on a twisted bilayer graphene superlattice. *Physical Review B*, 97:235453, Jun 2018.

[114] Tongyun Huang, Lufeng Zhang, and Tianxing Ma. Antiferromagnetically ordered Mott insulator and $d+id$ superconductivity in twisted bilayer graphene: A quantum Monte carlo study. *arXiv e-prints*, arXiv:1804.06096, Apr 2018.

[115] Yu-Ping Lin and Rahul M. Nandkishore. A chiral twist on the high-T_c phase diagram in Moir\'e heterostructures. *arXiv e-prints*, arXiv:1901.00500, Jan 2019.

[116] Fengcheng Wu, A. H. MacDonald, and Ivar Martin. Theory of phonon-mediated superconductivity in twisted bilayer graphene. *Phys. Rev. Lett.*, 121:257001, Dec 2018.

[117] Pilkyung Moon and Mikito Koshino. Optical absorption in twisted bilayer graphene. *Phys. Rev. B*, 87:205404, May 2013.

[118] Zhiming Zhang, Yimeng Wang, Kenji Watanabe, Takashi Taniguchi, Keiji Ueno, Emanuel Tutuc, and Brian J. LeRoy. Flat bands in twisted bilayer transition metal dichalcogenides. *Nature Physics*, 1745-2481, Jul 2020.

[119] Yusong Bai, Lin Zhou, Jue Wang, Wenjing Wu, Leo McGilly, Dorri Halbertal, Chiu Fan B. Lo, Fang Liu, Jenny Ardelean, Pasqual Rivera, Nathan R. Finney, Xuchen Yang, Dmitri N. Basov, Wang Yao, Xiaodong Xu, James Hone, Abhay Pasupathy, and Xiaoyang Zhu. One-dimensional moiré excitons in transition-metal dichalcogenide heterobilayers *Nature Materials*, 1476-4660, Jul 2020.

[120] Astrid Weston, Yichao Zou, Vladimir Enaldiev, Alex Summerfield, Nicholas Clark, Viktor Z'olyomi, Abigail Graham, Celal Yelgel, Samuel Magorrian, Mingwei Zhou, Johanna Zultak, David Hopkinson, Alexei Barinov, Thomas Bointon, Andrey Kretinin, Neil R. Wilson, Peter H. Beton, Vladimir I. Fal'ko, Sarah J. Haigh, and Roman Gorbachev. Atomic reconstruction in twisted bilayers of transition metal dichalcogenides. *arXiv e-prints*, arXiv:1911.12664, Nov 2019.

[121] Barry Bradlyn, Luis Elcoro, Jennifer Cano, M. G. Vergniory, Zhijun Wang, Claudia Felser, M. I. Aroyo, and B. Andrei Bernevig. Topological quantum chemistry. *Nature*, 547:298–305, 2017.

[122] Shiang Fang, Rodrick Kuate Defo, Sharmila N. Shirodkar, Simon Lieu, Georgios A. Tritsaris, and Efthimios Kaxiras. Ab initio tight-binding hamiltonian for transition metal dichalcogenides. *Phys. Rev. B*, 92:205108, Nov 2015.

[123] Paolo Giannozzi, Stefano Baroni, Nicola Bonini, Matteo Calandra, Roberto Car, Carlo Cavazzoni, Davide Ceresoli, Guido L Chiarotti, Matteo Cococcioni, Ismaila Dabo, Andrea Dal Corso, Stefano de Gironcoli, Stefano Fabris, Guido Fratesi, Ralph Gebauer, Uwe Gerstmann, Christos Gougoussis, Anton Kokalj, Michele Lazzeri, Layla Martin-Samos, Nicola Marzari, Francesco Mauri, Riccardo Mazzarello, Stefano Paolini, Alfredo Pasquarello, Lorenzo Paulatto, Carlo Sbraccia, Sandro Scandolo, Gabriele Sclauzero, Ari P Seitsonen, Alexander Smogunov, Paolo Umari, and Renata M Wentzcovitch. QUANTUM ESPRESSO: a modular and open-source software project for quantum simulations of materials. *Journal of Physics: Condensed Matter*, 21(39):395502, sep 2009.

[124] P Giannozzi, O Andreussi, T Brumme, O Bunau, M Buongiorno Nardelli, M Calandra, R Car, C Cavazzoni, D Ceresoli, M Cococcioni, N Colonna, I Carnimeo, A Dal Corso, S de Gironcoli, P Delugas, R A DiStasio, A Ferretti, A Floris, G Fratesi, G Fugallo, R Gebauer, U Gerstmann, F Giustino, T Gorni, J Jia, M Kawamura, H-Y Ko, A Kokalj, E Küçükbenli, M Lazzeri, M Marsili, N Marzari, F Mauri, N L Nguyen, H-V Nguyen, A Otero de-la Roza, L Paulatto, S Poncé, D Rocca, R Sabatini, B Santra, M Schlipf, A P Seitsonen, A Smogunov, I Timrov, T Thonhauser, P Umari, N Vast, X Wu, and S Baroni. Advanced capabilities for materials modelling with quantum ESPRESSO. *Journal of Physics: Condensed Matter*, 29(46):465901, oct 2017.

[125] Kristian Berland, Valentino R Cooper, Kyuho Lee, Elsebeth Schröder, T Thonhauser, Per Hyldgaard, and Bengt I Lundqvist. van der waals forces in density functional theory: a review of the vdW-DF method. *Reports on Progress in Physics*, 78(6):066501, may 2015.

[126] Ikutaro Hamada and Minoru Otani. Comparative van der waals density-functional study of graphene on metal surfaces. *Phys. Rev. B*, 82:153412, Oct 2010.

[127] Nicolas Mounet, Marco Gibertini, Philippe Schwaller, Davide Campi, Andrius Merkys, Antimo Marrazzo, Thibault Sohier, Ivano Eligio Castelli, Andrea Cepellotti, Giovanni Pizzi, and Nicola Marzari. Two-dimensional materials from high-throughput computational exfoliation of experimentally known compounds. *Nature Nanotechnology*, 13(3):246–252, Mar 2018.

[128] Felice Conte, Domenico Ninno, and Giovanni Cantele. Electronic properties and interlayer coupling of twisted mos_2/$nbse_2$ heterobilayers. *Phys. Rev. B*, 99:155429, Apr 2019.

[129] Andrea Dal Corso. Pseudopotentials periodic table: From h to pu. *Computational Materials Science*, 95:337 – 350, 2014.

[130] Peter Scherpelz, Marco Govoni, Ikutaro Hamada, and Giulia Galli. Implementation and validation of fully relativistic gw calculations: Spin–orbit coupling in molecules, nanocrystals, and solids. *Journal of Chemical Theory and Computation*, 12(8):3523–3544, 2016. PMID: 27331614.

[131] Jeil Jung, Arnaud Raoux, Zhenhua Qiao, and A. H. MacDonald. Ab initio theory of moiré superlattice bands in layered two-dimensional materials. *Phys. Rev. B*, 89:205414, May 2014.

[132] Fengcheng Wu, Timothy Lovorn, Emanuel Tutuc, Ivar Martin, and A. H. MacDonald. Topological insulators in twisted transition metal dichalcogenide homobilayers. *Phys. Rev. Lett.*, 122:086402, Feb 2019.

[133] Peter Scherpelz, Marco Govoni, Ikutaro Hamada, and Giulia Galli. Implementation and validation of fully relativistic gw calculations: Spin–orbit coupling in molecules, nanocrystals, and solids. *Journal of Chemical Theory and Computation*, 12(8):3523–3544, 2016. PMID: 27331614.

[134] V. V. Enaldiev, V. Zólyomi, C. Yelgel, S. J. Magorrian, and V. I. Fal'ko. Stacking domains and dislocation networks in marginally twisted bilayers of transition metal dichalcogenides. *Phys. Rev. Lett.*, 124:206101, May 2020.

[135] Stephen Carr, Daniel Massatt, Steven B. Torrisi, Paul Cazeaux, Mitchell Luskin, and Efthimios Kaxiras. Relaxation and domain formation in incommensurate two-dimensional heterostructures. *Phys. Rev. B*, 98:224102, Dec 2018.

[136] Luis Elcoro, Barry Bradlyn, Zhijun Wang, Maia G Vergniory, Jennifer Cano, Claudia Felser, B Andrei Bernevig, Danel Orobengoa, G Flor, and Mois I Aroyo. Double crystallographic groups and their representations on the bilbao crystallographic server. *Journal of Applied Crystallography*, 50(5):1457–1477, 2017.

[137] Congjun Wu, Doron Bergman, Leon Balents, and S. Das Sarma. Flat bands and wigner crystallization in the honeycomb optical lattice. *Phys. Rev. Lett.*, 99:070401, Aug 2007.

[138] Tian-Heng Han, Joel S. Helton, Shaoyan Chu, Daniel G. Nocera, Jose A. Rodriguez-Rivera, Collin Broholm, and Young S. Lee. Fractionalized excitations in the spin-liquid state of a kagome-lattice antiferromagnet. *Nature*, 492(7429):406–410, Dec 2012.

[139] C. Broholm, R. J. Cava, S. A. Kivelson, D. G. Nocera, M. R. Norman, and T. Senthil. Quantum spin liquids. *Science*, 367(6475), 2020.

[140] Stephen Carr, Daniel Massatt, Mitchell Luskin, and Efthimios Kaxiras. Duality between atomic configurations and bloch states in twistronic materials. *Phys. Rev. Research*, 2:033162, Jul 2020.

[141] Hoi Chun Po, Liujun Zou, T. Senthil, and Ashvin Vishwanath. Faithful tight-binding models and fragile topology of magic-angle bilayer graphene. *Phys. Rev. B*, 99:195455, May 2019.

[142] Stephen Carr, Shiang Fang, Hoi Chun Po, Ashvin Vishwanath, and Efthimios Kaxiras. Derivation of wannier orbitals and minimal-basis tight-binding hamiltonians for twisted bilayer graphene: First-principles approach. *Phys. Rev. Research*, 1:033072, Nov 2019.

[143] Miao Zhou, Zheng Liu, Wenmei Ming, Zhengfei Wang, and Feng Liu. sd^2 graphene: Kagome band in a hexagonal lattice. *Phys. Rev. Lett.*, 113:236802, Dec 2014.

[144] Wai-Kee Li and S. M. Blinder. Particle in an equilateral triangle: Exact solution of a nonseparable problem. *Journal of Chemical Education*, 64(2):130, 1987.